RESEARCH ACTIVITIES

Upgrade Plan of 15MeV Compact Electron Linear Accelerator LEENA as a Terahertz Radiation Source

Satoshi Hashimoto, Sayaka Chin, Dazhi Li[#], Sho Amano and Shuji Miyamoto
LASTI, University of Hyogo
[#] Institute of Laser Technology

Abstract

We are planning to upgrade the 15MeV electron linear accelerator LEENA as a radiation source in terahertz regime. For the precise beam handling, an old-fashioned control system is now partially updated to the new one based on PC and Linux. Upgrade of other components such as beam monitors, RF low-level system, and terahertz radiation monitoring system are also being planed. Beam commissioning for the generation of terahertz light by Smith-Purcell radiation has started.

Introduction

Apart from 1.5GeV electron storage ring, we have a 15MeV electron linear accelerator LEENA [1] in the NewSUBARU facility. This compact linac was constructed prior to the NewSUBARU ring, and studies on free electron laser in IR regime and the generation of bright beam using needle cathodes have been performed [2]. The aging machine has an old-fashioned control system and its performance was poor. Thus we planed the upgrade of LEENA accelerator as a terahertz radiation source and some parts of this plan are underway.

Generation of terahertz radiation and its application are recently becoming more interesting. In addition to UV, soft X-ray and Compton gamma ray from NewSUBARU, the terahertz light form LEENA will further promote the industrial application of various kind of radiation in our facility.

General layout of the 15MeV Linac LEENA

Figure 1 shows the general layout of LEENA. Electron beams generated by a RF gun with a thermal cathode are bunched at an alpha magnet and accelerated up to 6-15MeV. After passing through a dispersive section, electron beams go to a radiation chamber. Then the beams are dumped after being deflected by a bending magnet. Main parameters of LEENA are shown in Table. I.

Table I Main parameters of LEENA

RF frequency	2856 MHz
Beam Energy	6-15MeV
Energy spread	+-0.5%@15MeV
Micro pulse	
peak current	50A
Pulse width	<10ps
Macro pulse	
Frequency	1-10Hz
Pulse width	10us

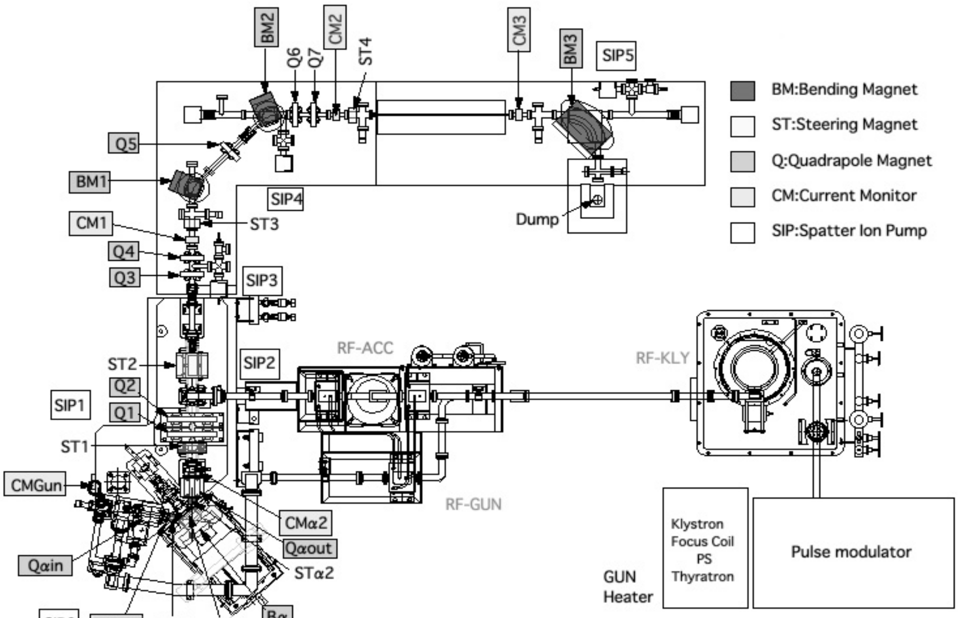

Fig.1. Layout of LEENA accelerator

Upgrade of Accelerator Control System

The control system of LEENA was based on PLC (Programmable Logic Controller). Magnet currents and RF parameters were adjusted by potentiometers or from a touch panel. Thus it was difficult to precisely control these parameters and the reproducibility was poor.

We are developing the new control system that is based on LabVIEW and EPICS [3] and can be flexibly controlled from Windows or Linux machines. Three PC or Linux machines are running as virtual machines (VMs) in VMware server on a Linux host machine. Operation programs for controlling devices run over the VMs. Client machines access to the VMs through the dedicated network for LEENA. Any kind of devices for LEENA, including PLC, oscilloscopes, GPIB-Ethernet converters, and network-distributed devices, is connected to this private LAN. PLC (Mitsubishi MELSEC Q-series) is already connected to LabVIEW via OPC server and we are developing several control programs with a graphical user interface. Main program controlling LEENA will be developed with EPICS.

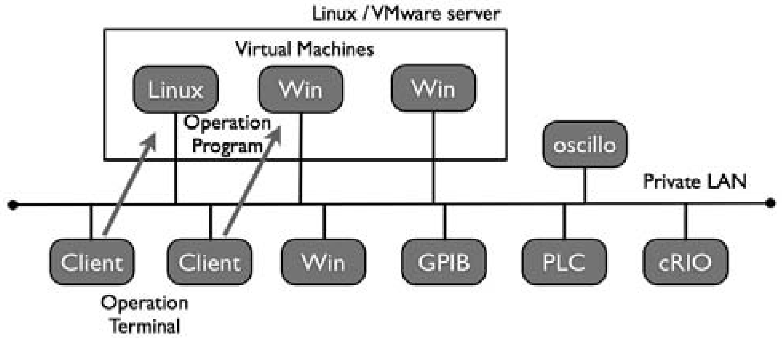

Fig. 2. New control system for LEENA

Other Upgrades

In addition to the control system, the following system upgrades are planning or underway.

Present beam monitor system is composed from six current transformers (CT) and four screen monitors. In addition to these monitor, beam position monitors (BPM) are necessary for precise control of the beam trajectory and a few will be installed. The shape and length of electron bunches play important roles in generating terahertz radiation. Development of a bunch length monitor using both the electro-optical detection of Coulomb field and the single-shot cross-correlation of optical pulses [4] is desired.

One of the most important problems to be solved is the beam loss at beam transport. It is necessary for reducing the beam loss not only to precisely control magnet and RF parameters, but also to study beam dynamics using simulation code such as GPT [5]. Another important problem is the beam stability. Present unstable operation may come from poor controls of RF low level and utilities such as cooling water. The new control system based on PC is useful to a feedback control of these quantities.

As for measurement of terahertz radiation, monitor systems of power and spectrum are under construction.

Generation of Terahertz Light

Three radiation sources may be possible for the generation of terahertz light with LEENA; (1) Smith-Purcell (SP) radiation, (2) coherent synchrotron radiation from a bending magnet with bunched electron beams, (3) free electron laser in terahertz regime.

SP radiation is generated when an electron beam passes close to the surface of a periodic structure, that is, a diffraction grating. In LEENA a diffraction grating has been installed and beam commissioning operation started in April 2011. In addition to the conventional SP radiation, observation of coherent SP and superradiant SP radiations [6] are expected.

Acknowledgement

We greatly thanks to Mr. Kawata, Mr. Takemura and Dr. Minagawa for their cooperation.

References

[1] http://www.lasti.u-hyogo.ac.jp/NS-en/facility/leena/
[2] T. Inoue *et al*., Jpn. J Appl. Phys., **41**, pp.7402-7406 (2002).
[3] http://www.aps.anl.gov/epics/index.php
[4] B. Berden *et al*., Proceedings of EPAC2004, pp.2700 (2004)
[5] http://www.pulsar.nl/
[6] D. Li *et al*., Phys. Rev. ST AB, 9, 040701 (2006)

Photonuclear reaction of iodine-129 with laser-Compton scattering gamma-ray

Ken Horikawa
LASTI, University of Hyogo

Abstract

A photonuclear reaction cross section of iodine-129 was measured using a polarized laser-Compton scattering gamma-ray beam in an energy range from 13.9 to 19.7 MeV. The maximum cross section was evaluated to be 220 mbarn ±50% at a photon energy of 15.9 MeV ±4%. We did not observe any appreciable difference in the cross sections for linearly and circularly polarized gamma-ray beams, considering the limits of experimental error.

Introduction

We previously proposed the nuclear transmutation of radioactive nuclei including iodine-129 using a laser-Compton scattering (LCS) gamma-ray beam1). To evaluate the process efficiency, we must have an accurate photonuclear reaction cross section of iodine-129. J. Magill et al.2) measured an integral cross section of iodine-129 σ_R by laser-generated bremsstrahlung photons that had a Boltzmann-like distribution with a hot-electron temperature with random polarizations. They assumed a Lorentzian shape for σ_R with a calculated energy threshold of 8.8 MeV and E_{max} = 12.4 MeV, and obtained a cross section of $\sigma_R(E_{max})$ = 220 mbarn2), where E_{max} is the photon energy which maximizes the σ_R and $\sigma_R(E_{max})$ is the σ_R at E_{max}. Unfortunately, their measurement was only accurate within a factor of two. In addition, the gamma-ray-polarization dependence of the cross section has not been investigated yet. For this study, we carried out measurements at NewSUBARU to determine the dependence of the photonuclear reaction cross section of iodine-129 on the energy and polarization of incident gamma-ray photons.

Experimental

Polarized gamma-rays with maximum energy of 16.7 MeV were generated in the storage ring by the interaction between a 1.064-μm CW laser beam of 4.6 W and a 974 MeV electron beam of 220 mA. The laser polarization was rotated using a combination of λ/4 and λ/2 wave plates in a laser oscillator. The polarized gamma-rays were semi- monochromatized in the 3% energy spread using a 3-mm-diameter lead collimator. The flux of the gamma-rays incident on the target was measured using a 10-mm-thick plastic scintillator that was installed in front of the target. The scintillator was attached with a 1-mm-thick piece of lead as a signal multiplier on the beam incident side. The flux of the polarized and semi- monochromatized gamma-rays was measured to be 5 × 10^5 photons sec^{-1} 3). The polarization of the gamma-rays was measured4) and confirmed to be controllable by the polarization of the incident laser beam.

Iodine-129 was prepared as a powder of palladous iodide. The radioactivity of the target was calibrated to be 36.8 kBq by Isotope Products Laboratories5). The number of iodine-129 atoms in the target was calculated to be 2.63 × 10^{19} from its radioactivity of 36.8 kBq and the half-life of iodine-129 $\tau_{I\text{-}129}$ = 1.57 × 10^7 year6).

The number of iodine-128 atoms $N(t)$ is derived as a function of time from the following equation:

$$N(t) = \frac{Y}{\lambda}\left(1 - e^{-\lambda t}\right). \tag{1}$$

where Y is the yield rate of iodine-128, $\lambda = \ln 2/\tau_{I-128}$ = 0.028 min^{-1} is the decay rate coefficient, which is constant, and $\tau_{I\text{-}128}$ = 25 min is the half-life of iodine-1286). After the irradiation of the gamma-rays, the number of decayed gamma-rays with an energy of 443 keV, which were emitted from the radioactive iodine-128, was measured using a Ge detector. The peak detection efficiency of the Ge detector used in this experiment was calibrated to be 5% using the 384-keV gamma-ray photons emitted by barium-133. The probability of one iodine-128 atom emitting a 443-keV photon in a spontaneous decay process was considered to be 12.6%6). The number of iodine-128 atoms N_i was calculated using the following equation:

$$N_i = \frac{N_T}{1 - e^{-\lambda T}}, \tag{2}$$

where N_T is a number of decayed iodine-128 atoms and T is a time period for measuring the 443-keV photons.

Derivation of reaction cross section

The photonuclear reaction cross section of iodine-129 σ_R was evaluated as follows using N_i [Eq. (2)]. The variation of the yield rate of iodine-128 dY for distance dx along the direction of the LCS gamma-ray beam is expressed as follows:

$$dY = n \cdot f(x) \cdot \sigma_R \cdot dx \cdot dS, \tag{3}$$

where n is the atomic density of iodine-129 and $f(x)$ is the flux of the gamma-ray photons per unit area at position x. The atomic density was calculated to be 7.4 × 10^{17} mm^{-3} from the size of the target. The 3-mm-diameter collimator passes an axial portion of the incident gamma-ray beam so that the spatial distribution of the transmitted beam with a 3-mm diameter is uniform, and the target has rotational symmetry whose axis is coaxial with the beam axis. By evaluating Eq. (4), Y is described as follows:

$$Y = 2\pi \cdot n \cdot \sigma_R \cdot f(0) \int_0^R r \int_0^{L(r)} e^{-n(\sigma_R+\sigma_S)x}\, dx\, dr\,, \qquad (4)$$

where $f(0)$ is the value of the incident flux at the target entrance. $f(0)$ was measured as $f(0) = 4.7 \times 10^4$ photon mm^{-2} sec^{-1} ± 2%. R is the radius of the target, $L(r)$ is the penetration distance of the incident gamma-rays into the target, which is a function of radius r. σ_S is the cross section for all processes except the photonuclear reaction.

Dependence of reaction cross section on polarization and energy of incident gamma-rays

Fig. 1 shows photonuclear reaction cross section σ_R derived from Eqs. (1) and (4) by assuming the value of σ_S proposed by J. Berger et al.[7] in an energy range from 13.9 to 19.7 MeV for both linear (crossed) and circular (circled) polarizations of incident gamma-rays. The gamma-ray photon energy was scanned by changing the energy of the electron beam from 890 to 1060 MeV. The probability distribution of the signal intensity against the count rate was assumed to be a Poisson distribution. From its standard deviation, the error bars in Fig. 1 were calculated to be 12% at respective gamma-ray energy. The error in the absolute value of the cross section was evaluated to be ±50% by taking into account the errors due to the alignment accuracy between the gamma-ray beam and the target axes; this accuracy was a major factor compared with the errors in the number of iodine-129 atoms (< ±1%), the flux of the gamma-rays (±2%), their energy spread (-3%), and the peak detection efficiency of the Ge detector (±10%).

An appreciable difference in the cross sections determined for linear and circular polarizations was not observed because the data of both polarizations remained within the dispersion of the measurements. Therefore, all data of the cross section of the iodine-129 target were treated as a set and fitted by a Lorentzian curve to derive the dependence of the cross section on the photon energy[8]. From the above evaluation, the energy dependence of the cross section was determined by a fitting curve with a maximum value of 220 mbarn ±50% at 15.9 MeV ±4% with a half-width at half-maximum of 2.55 MeV ±20%. In this measurement the accuracy of the cross section obtained was improved compared with that of the data by J. Magill et al.[2] because the polarized gamma-rays were semi- monochromatized in the 3% energy spread so that the cross section was directly obtained for each energy point of the gamma-ray photon. The photon energy dependence of the iodine-129 σ_R was obtained experimentally by scanning the energy of the semi- monochromatized gamma-ray photons.

The (γ, n) reaction is caused by the giant resonance which is due to the gamma-ray photon field in nucleus. No appreciable difference observed in the cross sections determined for linear and circular polarizations suggests that the helicity of the photon due to the polarization does not affect the photon reaction by the giant resonance. The theoretical analysis to explain the above result will be done in further study.

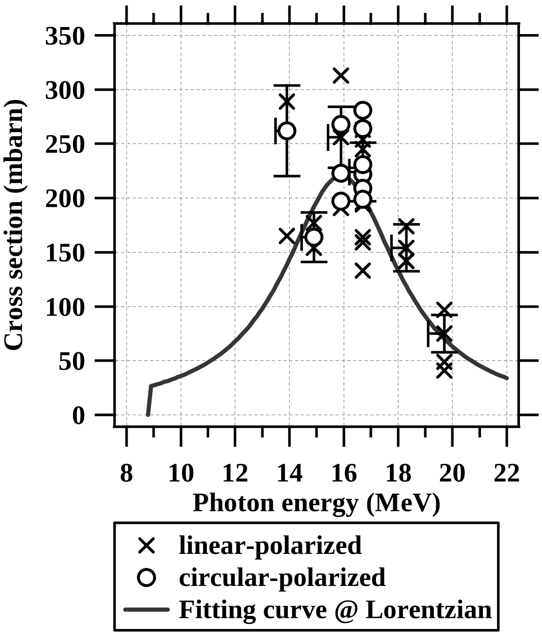

Fig. 1 Dependence of photonuclear reaction cross section of iodine-129 on energy and polarization of gamma-ray photons.

Conclusion

We determined the maximum photonuclear reaction cross section of iodine-129 to be 220 mbarn ±50% at a photon energy of 15.9 MeV ±4% with a half-width at half-maximum of 2.55 MeV ±20%. We did not observe any appreciable difference in the cross sections determined for linearly and circularly polarized gamma-ray beams considering the limits of experimental error.

Reference

[1] K. Imasaki *et al.*: *Proc. SPIE Advanced High Power Lasers and Applications '99, Osaka Japan, 1999*, pp.**721** (2000).

[2] J. Magill *et al.*: Appl. Phys. B, **77**, pp.387 (2003).

[3] K. Horikawa *et al.*: Nucl. Instr. and Meth. A, **618**, pp.209 (2010).

[4] Nobuhiko Sakai *et al.*: submitted in Nucl. Instr. and Meth. A.

[5] Isotope Products Laboratories. Eckert & Ziegler Isotope Products (Main Office) 24937 Avenue Tibbitts Valencia, CA 91355.

[6] Jagdish K. Tuli: "Nuclear Decay Data in the MIRD Format," <http://www.nndc.bnl.gov/mird/> (2010).

[7] M. J. Berger *et al.*: "XCOM: Photon Cross Sections Database," <http://www.nist.gov/pml/data/xcom/index.cfm> (2010).

[8] R. L. Bramblett *et al.*: Phys. Rev, **148**, pp.1198 (1966).

Determination of the number of pulsed laser-Compton scattering photons

Takeo Kondo[1], Hiroaki Utsunomiya[1], Hidetoshi Akimune[1], Tamio Yamagata[1], Akiyuki Okamoto[1], Hideo Harada[2], Fumito Kitatani[2], Tatsushi Shima[3], Ken Horikawa[4], Shuji Miyamoto[4]
[1]Department of Physics, Konan University [2]JAEA [3]RCNP, Osaka University [4]LASTI, University of Hyogo

Abstract

We measured pulse-height spectra of 16.7 MeV laser-Compton scattering photons with a 6” × 5” NaI(Tl) detector for a blank and three lead materials of 75.8, 50.9, and 25.9 % transmissions at the NewSUBARU facility to investigate how the original Poisson distribution of the pulsed photons is modified after passing through thick-target materials. We present a well- prescribed method of determining the number of incident photons within 3.5% accuracy based on the response of the NaI(Tl) detector to the pulsed photon beams.

1. Introduction

Quasi-monochromatic γ-ray beams are produced in the interaction of laser photons with relativistic electrons, which is referred to as inverse Comp- ton scattering, at synchrotron radiation facilities in Japan[1, 2], where the laser-Compton scattering (LCS) γ -ray beam is used in nuclear physics experiments. An experimental study of photon-induced nuclear reactions requires a thick target material because of small interaction cross sections. Therefore, the determination of the number of photons incident on the target material is an important experimental factor,

Collisions of pulsed laser photons with relativistic electrons in a storage ring are a statistical phenomenon. Thus, the probability distribution of the number of scattered photons n is expected to follow the binomial distribution. Since the product of the numbers of laser photons and electrons, N, involved in each laser pulse is very large and the collision probability p is very small, the binomial distribution may be reduced to a Poisson distribution[3]

$$P_m(n) = \frac{m^n}{n!} e^{-m} \qquad (1)$$

where m is the average number of scattered photons per laser pulse which is given by $m = Np$.

Previously it was shown that energy spectra of pulsed LCS photon beams measured with a BGO detector are characterized by the Poisson distribution[4]. Thus, it is straightforward to deduce the number of LCS photons if the average number of scattered photons per laser pulse, m, is experimentally determined. In measurements with a thick target, the Poisson distribution is modified by attenuation of pulsed LCS photons in the target material. How- ever, it is readily shown that the modified distribution remains a Poisson distribution with a different value of the average number of scattered pho- tons m′. Also shown is that the number of LCS photons incident on the target can be deduced if m′ is corrected for the attenuation by a factor α

$$m' = \alpha m \qquad (2)$$

with $\alpha = e^{-\mu t}$, where μ is the linear attenuation coefficient of γ rays and t is the thickness of target material.

We experimentally tested this prescription for determining the photon flux using thick lead materials of different thicknesses and verified the prescription. We report results of the experimental test and present an experimental formula for the photon flux determination which is useful in a thick target measurement.

2. Experiment

We produced a 16.7 MeV pulsed quai-monochromatic γ-ray beam in the laser-Compton scattering of 1064 nm laser photons from 974 MeV electrons at the NewSUBARU facility. The quoted γ-ray energy stands for the maximum energy. A top-up

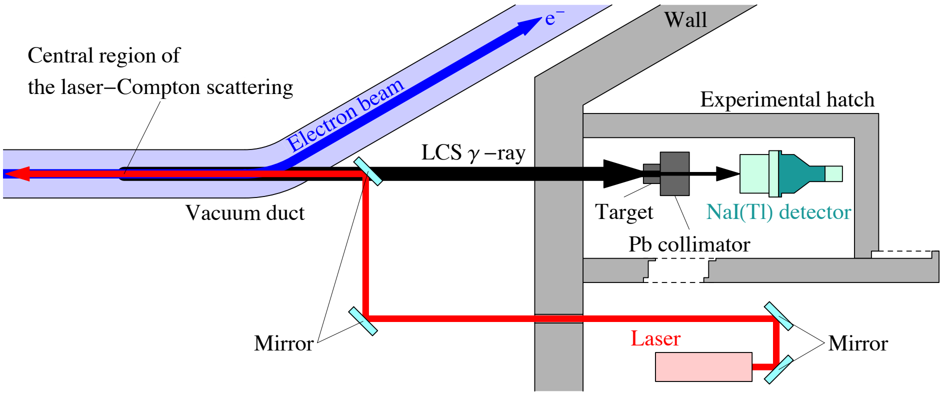

Fig. 1: Experimental setup in the LCS γ-ray production beam line at the NewSUBARU facility.

operation of the storage ring was carried out, where electrons are injected from a linear accelerator whenever a decrease of the electron beam current beyond a threshold is detected. The top-up operation kept the beam current constant at 219.98 ± 0.44 mA (0.2 % variation) during the present measurement. The experimental setup is depicted in Fig. 1. Laser photons from a YVO_4 laser operated in a Q-switch mode at 30 kHz were injected into a 20 m straight section of a storage ring of race-track shape. A 3 mm lead collimator of 100 mm thickness was mounted in a small experimental hatch at the distance of 16.49 m from the central region of the laser-Compton scattering. Three natural lead targets of 4.4, 10.6, 21.2 mm thicknesses were used. The transmission rate of the three targets is 75.8, 50.9, and 25.9 %, respectively [5]. The target was mounted immediately upstream the collimator. A NaI(Tl) detector of 6 in. diameter and 5 in. length (REXON components inc., USA) was mounted at 30 cm downstream the collimator to measure the 16.7 MeV LCS γ-ray beam. Measurements at 3.94 W laser power were carried out for 600 sec to obtain energy specctra of the pulsed LCS photon beam for the three lead targets and a blank target. Single-photon spectra were also measured for 300 sec at a reduced laser power 0.10 W in the blank- and lead-target runs. We note that 14.2 % of the 16.7 MeV photons transmit the NaI(Tl) detector. However, this transmission does not essentially affect the discussion made below.

3. Results and analysis

Figure 2 shows multi-photon pile-up spectra hp(x) measured for a blank target and the three lead targets. Single-photon spectra $h_s(x)$ measured for each target are also shown in the figure. Obviously the result for a blank target (Fig. 2(a)) represents a pile-up spectrum of the LCS γ-ray beam originally produced in the interaction between laser photons and relativistic electrons. One can see in Figs. 2(b), 2(c) and 2(d) that the pile-up spectra vary when the γ-ray beam passes through the lead targets in such a way that the center of gravity of the distribution is shifted toward less multiplicity with increasing the target thickness (decreasing the transmission rate). This is obviously because of the attenuation of the LCS γ rays in the target materials.

The NaI(Tl) detector responds differently when it detects n photons with each having 16.7 MeV and a photon with 16.7 × n MeV. The response to multiple photons with the multiplicity n with each having 16.7 MeV, $R_n(x)$, was calculated from the experimental single-photon spectrum, $R_1(x)$, by

$$R_n(x) = \int \dots \int \prod_{i=1}^{i=n} R_1(x_i)dx_1 \quad \text{where} \quad x = \sum_{i=1}^{i=n} x_i .$$

The resultant multiple-photon spectra are shown in Fig. 3 for n= 2-10 as well as the single-photon spectra (n=1).

In Fig. 4, we compare the peak position of the experimental pile-up spectrum corresponding to the multiplicity n (solid circles) with the calculation (open circles) for the blank and three Pb targets. It is noted that the n=1 peak positions of the pile-up spectra

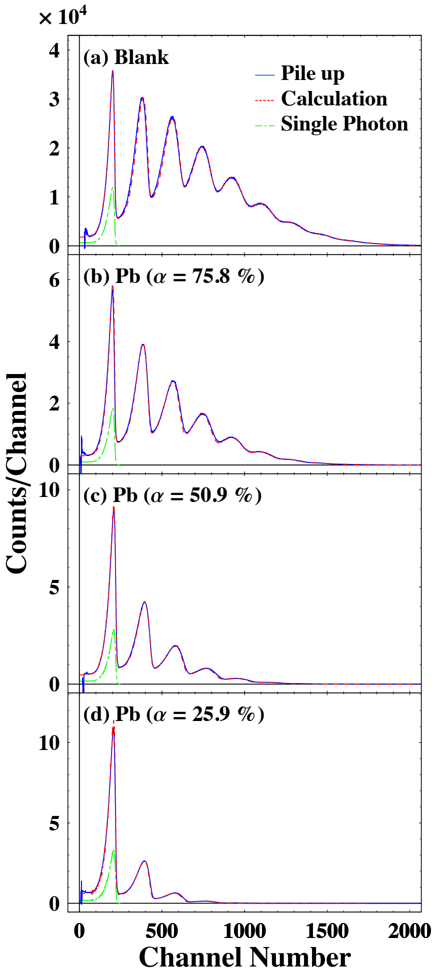

Fig. 2: Experimental pile-up spectra of a 16.7 MeV LCS γ-ray beam measured with the 6” × 5” NaI(Tl) detector for a blank (a) and three lead targets with 75.8 % (b), 50.9 % (c), and 25.9 % (d) transmission rates, respectively. Experimental single-photon spectra are shown by the dashed lines in an arbitrary scale. Best fits to the experimental pile-up spectra are shown by the dotted lines.

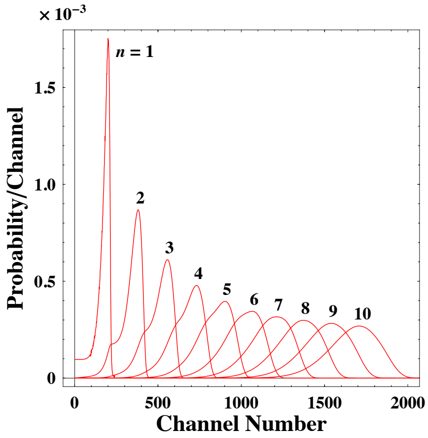

Fig. 3: The multiple-photon distributions with the multiplicity n (n= 1-10) calculated from the experimental single-photon distribution (see text).

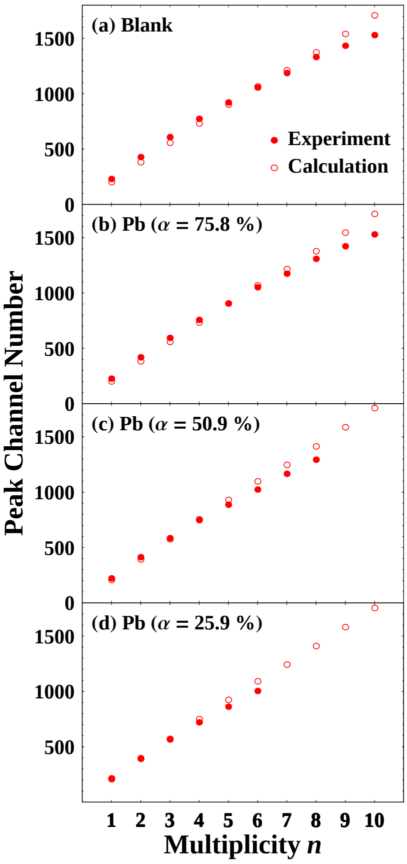

Fig. 4: The peak channels of the experimental pile-up spectra corresponding to the multiplicity n (filled circles) in comparison with those of the experimental single-photon distribution with *n*=1 and calculated multiple-photon distributions with *n*=2-10 (open circles).

(solid circles) for blank and the lead target with 75.8 % transmission are larger by 14-12 % than those of the corresponding single- photon spectra (stars). The same tendency is seen for the peak positions of the pile-up (solid circles) and calculated (open circles) spectra with *n*=2-4. This discrepancy is unlikely to take place for the primary component of the NaI(Tl) scintillation light with 230 ns decay time in view of the 30 kHz frequency of the γ-ray beam pulses. However it may take place for an afterglow by phosphorescence with 0.15 s decay time [6]. The afterglow effect may be enhanced in a detection of high-multiplicity photons each having 16.7 MeV. Indeed, it has been observed in past measurements with LCS γ-ray beams at 20 kHz at the National Institute of Advanced Industrial Science and Technology [1] that a discrepancy of the *n*=1 peak position in single-photon and pile-up spectra increases with increasing the average number of photons per beam pulse. Furthermore, we note that the experimental peak position for higher multiplicities tends to saturate more rapidly than the calculation. We ascribe this saturation effect to the response of the photomultiplier tube of the NaI(Tl) detector. The deviation observed at *n*=10 in blank and the Pb target with 75.8 % transmission was 11 %.

The experimental pile-up spectra were fitted by a superposition of the calculated multiple-photon distributions, where corrections were made for the dependence of the peak position on the multiplicity. Best-fit results are shown by the dotted lines in Fig. 2. Thus, the experimental pile-up spectra were decomposed into multiple-photon events with the multiplicity *n*. The number of the multiple-photon events are shown by the histogram as a function the multiplicity n in Fig. 5 for blank and the three Pb targets. The experimental distribution of the multiple-photon events was fitted by a Poisson distribution for each targets. The resultant Poisson distributions are also shown in Fig. 5.

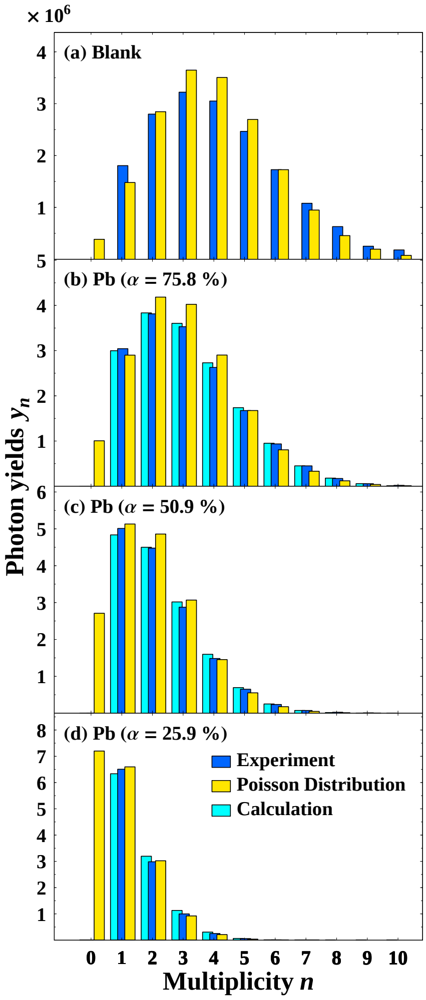

Fig. 5: The peak channels of the experimental pile-up spectra corresponding to the multiplicity n (filled circles) in comparison with those of the experimental single-photon distribution with *n*=1 and calculated multiple-photon distributions with *n*=2-10 (open circles).

One can easily understand the experimental fact that the multi-photon distribution (the distribution of the multiple-photon events) resulting from the attenuation of the LCS photons in the target material remains a Poisson distribution.

Starting from the multi-photon distribution for a blank target, we calculated those for the three Pb targets taking their transmission rates of 75.8, 50.9 and 25.9 % into account. The results are shown by the half-tint histogram in Fig.5. One can see that the experimental multi-photon distributions for the three Pb targets are well reproduced by the calculation.

Table I. The number of the LCS photons incident on targets estimated from the Poisson distribution with $n \geq 0$ shown in Fig.5. The number of the LCS photon-beam pulses with $n \geq 0$ is given by the product of the frequency of the laser (30 kHz) and the data acquisition time (600 s); $N_0 = 1.80 \times 10^7$.

target	$m^{\text{fit 1)}}$	$N^{\text{out}}_{\gamma}(\times 10^7)$	$N^{\text{in}}_{\gamma}(\times 10^7)$
Blank	3.84	6.90	6.90
Pb (α=75.8%)	2.89	5.19	6.85
Pb (α=50.9%)	1.89	3.41	6.70
Pb (α=25.9%)	0.916	1.65	6.38

1) The average number of photons in the Poisson distribution.

4. Discussion

It is straightforward to deduce the number of incident LCS photons, N_γ. Using the Poisson distribution, we get $N_\gamma = N_0 m$ which is the average number of photons per LCS photon-beam pulse m times the number of the LCS photon-beam pulses. The number of beam pulses is equal to the frequency of the beam pulses (30 kHz) times the data acquisition time.

The number of incident LCS γ rays is also obtained from the attenuated multi-photon distribution by $N_\gamma = N_0 m = N_0 m'/\alpha$ using the average multiplicity m' for the attenuated multi-photon distribution and the transmission probability α given by Eq.(2).

When we use the Poisson distributions that are best fits to the experimental multi-photon distributions, we obtain the number of the LCS photons incident on the target materials as listed in Table I. Note that the number of the LCS photons were in principle kept constant by the top-up operation of the NewSUBARU storage ring. The three measurements with the Pb targets give results that are consistent with that for blank target within 8 %.

In an actual experiment, a photon detector does not detect zero multiplicity events (n=0, no photons per beam pulse). However, the experimental multi-photon distribution can be directly used to determine the number of incident LCS photons. The number of LCS photons is determined from the product of the average number of photons per beam pulse and the number of beam pulses for the experimental $n \neq 0$ events. Note that the former quantity corresponds to $m'/(1-e^{-m'})$ in the Poisson distribution, while the latter quantity corresponds to $N_0(1-e^{-m'})$. The number of incident LCS photons is determined by correcting for the attenuation. The results are listed for blank and the three Pb targets in Table II. The agreement between the experimental quantities within 4.4 % is obtained. Furthermore, we note that the numbers of incident LCS photons determined from the experimental and the best-fit Poisson distributions agree well within 2.2 %.

Finally we present a more practical prescription for a photon flux determination. Instead of the multi-photon spectra with the multiplicity $n \neq 0$ (Fig. 5), let us deduce the number of incident LCS photons from the experimental pile-up spectra (Fig. 2).

The number of incident LCS photons obtained from this practical prescription is listed in Table III. The results obtained from blank and the three Pb targets agree to each other within 3.5%. Naturally the results are in excellent agreement with those given in Table II.

Table II. The number of the LCS photons incident on targets γ estimated from the experimental multi-photon distribution with $n \geq 1$ shown in Fig. 5.

target	$m^{\text{exp 1)}}$	$N_{\text{p}}^{2)}(10^7)$	$N^{\text{out}}_{\gamma}(10^7)$	$N^{\text{in}}_{\gamma}(10^7)$
Blank	3.97	1.72	6.81	6.81
Pb (α=75.8%)	3.12	1.63	5.10	6.73
Pb (α=50.9%)	2.29	1.48	3.39	6.67
Pb (α=25.9%)	1.56	1.08	1.69	6.52

1) The average number of photons in the experimental multi-photon distribution (Fig. 5).

Table III. The number of the LCS photons incident on targets γ calculated from the experimental pile-up spectra shown in Fig. 2.

target	$m^{\text{exp 1)}}$	$N_{\text{p}}^{2)}(10^7)$	$N^{\text{out}}_{\gamma}(10^7)$	$N^{\text{in}}_{\gamma}(10^7)$
Blank	3.97	1.73	6.87	6.87
Pb (α=75.8%)	3.14	1.66	5.21	6.88
Pb (α=50.9%)	2.33	1.49	3.48	6.84
Pb (α=25.9%)	1.59	1.08	1.72	6.65

1) The average number of photons in the experimental pile-up spectra (Fig. 2).

4. Conclusion

We experimentally investigated the nature of multi-photon distributions of pulsed LCS photons measured with the NaI(Tl) detector using blank and the three thick lead targets and found that the multi-photon distribution is well characterized by the Poisson distribution. We present an experimental formula based on pile-up photon spectra measured with the NaI(Tl) detector to determine the number of incident pulsed LCS photons within 3.5 % accuracy in a thick target measurement.

References

[1]H.Ohgaki et al., IEEE Trans. Nucl. Sci. 38 (1991) 386-392.

[2]K.Horikawa, S.Miyamoto, A.Amano, T. Mochizuki, Nucl. Instrum. Meth. A618(2010) 209-215.

[3]T. Kii et al., Proc. 12th symposium on Accelerator Science and Tech- nology.

[4]H. Toyokawa, T. Kii, H. Ohgaki, T. Shima, T. Baba, Y. Nagai, IEEE Trans. Nucl. Sci. 47 (2000) 1954-1957.

[5]http://physics.nist.gov/PhysRefData/XrayMassCoef/tab3.html

[6]S.Koički, A.Koički, and V.Ajdačić, Nucl. Instrum. Meth. 108 (1973) 297-299.

Resonant Photonuclear Reactions for Isotope Transmutation

Hiroyasu Ejiri[1,2] , Tatsushi Shima[1] , Shuji Miyamoto[3] , Ken Horikawa[3] , Yasuhisa Kitagawa[3]
Yoshihiro Asano[4], Schin Date[5], and Yuji Ohashi[5]
[1] RCNP, Osaka University, [2] Nuclear Science, Czech Technical University, [3] LASTI, University of Hyogo
[4] RIKEN/XFEL SPring-8, [5] JASRI SPring-8

Abstract

Resonant photonuclear isotope transmutation (RPIT) is shown to be very powerful to produce exclusively radioactive isotopes (RIs) by resonant photonuclear (γ,n) and (γ,2n) reactions via E1 giant resonances. Photons to be used are medium energy (E(γ) ≈ 12- 25 MeV) photons produced by laser photons backscattered off GeV electrons. The cross sections are as large as $\sigma \approx 0.2 - 0.5$ b (10^{-24}cm2) for all medium-heavy nuclei. A large fraction (~ 3%) of photons is effectively used for the photonuclear reactions, while the scattered GeV electrons remain in most storage rings to be re-used. To demonstrate the RPIT feasibility, ^{99}Mo/^{99m}Tc and ^{196}Au RIs were produced by RPIT on ^{100}Mo and ^{197}Au with laser photons scattered off 1 GeV electrons at the NewSUBARU storage ring. RPIT with medium energy photons around 10^{12-15}/sec provides specific/desired RIs with the rate of 10^{10-13}/sec and the RI density around 0.05-50 GBq/mg for nuclear science, molecular biology and for nuclear medicines.

1. Introduction

The present paper aims at reporting that RPIT(resonant photonuclear isotope trans- mutation) is quite powerful for exclusive RI (radio isotope) productions (transmutations). Nuclear reactions used for RPIT are resonant photonuclear reactions through giant resonances (GR) by means of laser electron photons, i.e. medium energy photons produced by laser photons backscattered off energetic GeV electrons in a storage ring.

RPIT is shown to be a very efficient and realistic way to provide various kinds of RIs to be used for nuclear physics, molecular biology, nuclear medicine and for other basic and applied science.

So far, (n,γ) reactions and nuclear fissions have been extensively used for RI productions and transmutations. Low energy thermal neutrons used for (n,γ) reactions and/or nuclear fissions are easily obtained by using intense medium energy protons and/or high flux nuclear reactors. RIs produced by (n,γ) reactions and those by nuclear fissions are limited to those with large neutron capture cross sections and those with large fission branches, respectively. Many kinds of fission product RIs, however, are produced in addition to the specific isotope of interest, and thus chemical separation is indispensable for extracting the desired isotope.

In the present report, we discuss the possible use of photonuclear reactions for nu- clear isotope transmutations. Actually, photonuclear reaction cross section is in general much smaller than typical nuclear cross sections because of the small EM coupling constant.

The main points of the present RPIT are to use resonant photonuclear excitations via E1 giant resonance[1] with the large cross section and to use energetic photon beams obtained by laser photons backscattered off GeV electrons. Such photon beams are called as laser electron photons. The main ideas of RPIT are discussed in the recent report.[2, 3]

Laser electron photons for RI productions have been discussed, as given in recent reports and references therein.[2,4,5] Photonuclear reactions and photo fissions for medical isotope productions and nuclear transmutations were evaluated by using the FLUKA simulation code.[4] Photonuclear reactions with photon beams of large brilliance and small band width ($\Delta E/E = 10^{-3}$) were discussed for production of medical RIs with high specific activity.[5] Isotope productions by using bremsstrahlung photons from medium energy electron beams were discussed in the recent report.[6] Among them, FEL(Free Electron Laser) photons backscattered off GeV electrons in the HIγS facility[7] is very interesting to provide medium energy photons for RPIT.

In what follows, we describe briefly RPIT with laser electron photons to provide efficiently various kinds of RIs with large RI production rate and high RI density. It is used to get RIs of interest without extra RIs. Unique features of RPIT and the E1 giant resonance and those of laser electron photons for photonuclear reactions are given in section 2 and section 3, respectively. RI production rates and efficiencies are discussed in section 4, and ^{99}Mo/^{99m}Tc and ^{196}Au productions by RPIT on ^{100}Mo and ^{197}Au with laser photons scattered off 1 GeV electrons at NewSUBARU are described in section 5. Concluding remarks and perspectives are presented in the last section.

2. Resonant photonuclear reactions via E1 giant resonance

Resonant photonuclear reactions via the isovector E1 giant resonance are used for RPIT. Merits of the resonant reactions are as given below.

1. The cross section is quite large because of the resonant excitation of many nucleons involved in the GR. The energy integrated cross section is given by

$$\int \sigma(E(\gamma))dE(\gamma) = 2\pi^2\alpha\frac{\hbar^2}{M}\frac{NZ}{A}(1+\kappa)$$
$$= 250\alpha A[fm^2 MeV] \qquad (1)$$

where N and Z are the proton and neutron numbers, $A = N + Z$ is the mass number, $\kappa \approx 0.2$ is the correction coefficient for the exchange current, and $\alpha = e^2/\hbar \approx 1/137$ is the EM coupling constant.

Table I. Cross sections for photonuclear reactions at E1 GR and cross sections for electron positron pair creations and Compton scatterings in unit of $b = 10^{-24}cm^2$.

Isotope	σ(GR) b	σ(e) b	σ(GR)/σ(e)
^{27}Al	0.07	0.95	0.071
^{63}Cu	0.16	3.3	0.048
^{100}Mo	0.25	6.1	0.041
^{124}Sn	0.31	8.9	0.034
^{208}Pb	0.52	20	0.026

Using the Breit-Wigner resonance shape with the observed width of $\Gamma \approx 4.5$ MeV for the E1 GR, the cross section at E(γ) = E(GR) is expressed as

$$\sigma(GR) \approx 2.5 \times 10^{-3}\, A\, b. \qquad (2)$$

The cross section amounts to about 30 % of the geometrical nuclear cross section. GR resonance cross sections for typical nuclei are shown in Table I and Fig.1. The cross section is proportional to the mass number A because of the resonant excitation. Therefore the small EM coupling of α ≈ 1/137 is well compensated by the large factor of A = 60~200 in case of medium heavy nuclei.

2. GR is a macroscopic oscillation of a bulk of protons and that of neutrons. Accordingly the cross section per nucleon, the resonance energy and the resonance width do not depend much on individual nuclides and insensitive to individual nuclear structures. The resonance energy is expressed as E(GR) ≈ aA−1/5 = 22~14 MeV for A = 30 ~ 200 nuclei as shown in Fig.1, and the width is as broad as Γ = 4 ~5 MeV. Thus one can preferentially excite GR in any nuclei by using medium energy photons. This is in contrast to (n,γ) reactions by thermal neutrons, where the cross section depends much on individual nuclides and nuclear level structures.

3. Photonuclear reactions on medium heavy nuclei at the GR region are mainly (γ,*n*) or (γ,2*n*) reactions, depending on $B(2n) \geq E(\gamma) \geq B(n)$ or $E(\gamma) \geq B(2n)$, where $B(n)$ and $B(2n) \approx 2B(n)$ are the one and two neutron binding energies, respectively. Then one gets exclusively nuclei with $(Z, N - 1)$ and $(Z, N - 2)$ from target nuclei with (Z,N) by using the (γ,*n*) and (γ,2*n*) reactions with adequate energy photons, respectively. In case of light nuclei, (γ,*p*) reactions are also used to produce RIs with $(Z - 1, N)$. Accordingly, it is possible to get specific/desired RI isotopes from stable isotopes, or short-lived RI isotopes from long-lived RI isotopes without producing many extra RIs. This is in contrast to fission products in nuclear reactors, where many extra isotopes are necessarily produced.

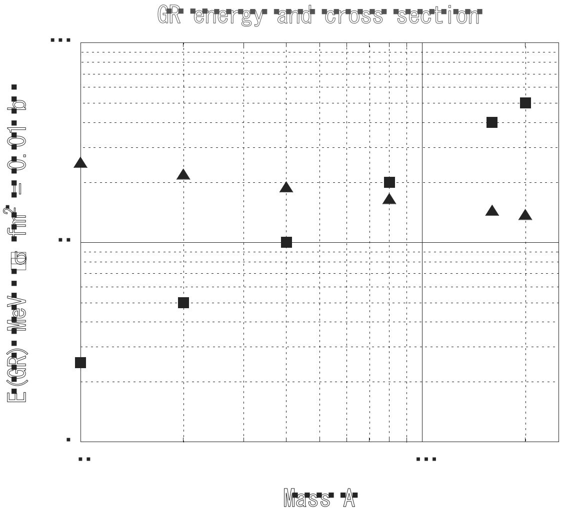

Fig. 1. *E1* giant resonance (GR) energy (triangles) and photonuclear cross sections via E1 GR (squares) as a function of the mass number A

3. Laser electron photons for photonuclear isotope transmutation

Medium energy photons with the appropriate energy of *E(γ) ≈ E(GR)* are obtained by Compton backscattering of laser photons from GeV electrons in a storage ring. Laser photons are amplified in energy via scattering off GeV electrons by many orders of magnitude, depending on the electron energy and the scattering angle. The appropriate energy window $\Delta E \approx \Gamma$ is selected by using a collimator to define the scattering angle.

The scattering process of laser photons is schematically shown in Fig.2.

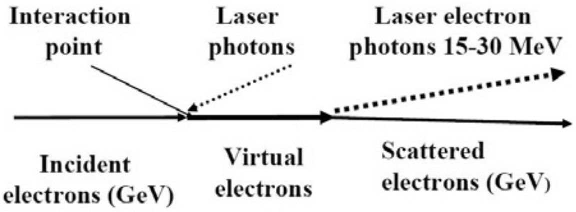

Fig. 2. Schematic view of production of laser electron photons by Compton backscattering of laser photons from GeV electrons.

Here the GeV electron is excited to a virtual state by the laser photon capture, and is split into the scattered GeV electron and the laser electron photon, i.e. the scattered photon. The scattered photon energy *E(γ)* is expressed in terms of the laser photon energy *E(l)* and the scattering angle *θ* with respect to the electron beam as

$$E(\gamma) = \frac{4\gamma_e^2 E(l)}{1 + 4\gamma_e E(l)/m + \gamma_e^2\theta^2} \qquad (3)$$

where m denotes the electron mass and $\gamma e = E(e)/m$ is the Lorentz factor of the incident electron with the energy *E(e)*. Noting $4\gamma e E(l)/m \ll 1$ in the present case, the photon energy can be conveniently expressed as

$$E(\gamma) = kE(l)f(\theta) \tag{4}$$

where $k \approx 4\gamma e2$ is the amplification factor, and $f(\theta) \approx [1 + \gamma e^2 \theta^2]^{-1}$ stands for the angle dependence. Since $f(\theta) \approx 1$ at the forward angle of $\theta = 0$, i.e. the backward angle with respect to the incident laser photon, the laser electron photon has the maximum energy of $k E(l)$ with the amplification factor $k \approx 4\gamma e2$ at $\theta = 0$.

The energy window of $E(\gamma) - E'(\gamma)$ can be set by using a collimator of an angle aperture of $\pm\Delta\theta$ at the forward direction, where $E(\gamma)$ and $E'(\gamma)$ are the photon energies at the scattering angles of $\theta = 0$ and $\theta = \Delta\theta$.

The laser electron photon energy and the band width are tuned by adjusting $E(l)$, $E(e)$ and $\Delta\theta$ so that the energy spectrum shows the peak at the maximum energy of $E(\gamma) \approx E(GR)$(~15 MeV) and the band width around $\Delta E(\gamma) \approx \Gamma$(~5 MeV).

The energy amplification factor is as large as $k = 10^{7\sim8}$ for the GeV electron energy of $E(e) = 1 \sim 3$ GeV. Then one gets medium energy photons of $E(\gamma) \approx 15$ MeV to be used for photonuclear reactions by using 1 ~ 0.1 eV laser photons.

The photon intensity of around 10^{8-12}/sec is realistic by using intense lasers and intense electrons. In future, high intensity photon sources with the intensity of the order of $10^{14\text{-}15}$/sec will be possible.

The laser electron photons have several advantageous points to charged particles and neutrons. They are as follows.

1. The laser photons are well collimated into a small angular region of $\theta \approx 1/\gamma e$. The angle spread is around $\theta \approx 0.15\text{-}0.5$ mrad. for 3-1 GeV electrons. Thus the nuclear transmutation is confined in the small cylinder within 1 mm in radius at around a few meters from the laser electron interaction point. This makes it possible to get isotopes with very high RI density of the order of GBq/mg, which is crucial for nuclear physics, molecular biology and nuclear medicines.

2. The large fraction (~ 3%) of the incident photons are effectively used for the isotope transmutation, as given in Table I. Here a very thick target of the order of 20~30 gr/cm2 can be used for photon beams since photons have no electric charge to interact with atomic electrons. Note that charged particles lose their energy mostly via interaction with atomic electrons without being used for nuclear reactions.

3. The scattered GeV electrons lose the energy via the interaction with the laser photon only by 0.3 ~1 % , depending on the scattering angle, and thus most of them can still remain in the storage ring to be re-accelerated up to the original energy by RF power supply.

4. The laser electron photons tuned to the GR energy are well above the (γ,n) threshold energy. In a typical case of the maximum photon energy of $E(\gamma) = 16$ MeV and the neutron binding energy of $B(n) = 8$ MeV, more than a half of the laser electron photons is above the threshold energy of 8 MeV for photonuclear reactions, and is used for photonuclear reactions. This is in contrast to bremsstrahlung photons, where the photon yields drop down rapidly with increase of the energy, and thus a small part of the high energy tail can be used for photonuclear reactions.[6]

5. Some laser electron photons interact with target nuclei to excite GR, which decays by emitting 1 or 2 fast neutrons and a few γ rays, while others interact with the electric field of the target nuclei to produce electron positron pairs with $E(e\pm) = 5 \sim 8$ MeV. These neutrons, γ rays and electron-positron pairs may be used for basic and applied science. Slowing down the fast neutrons, one may re-use them for another isotope transmutation.[4]

4. Photonuclear RI productions

Let's estimate the RI production rate and the RI density for RPIT. Photonuclear (γ,*n*) and (γ,2*n*) cross sections via the E1 GR are given as $\sigma e(n) = \sigma e(GR)Br(n)$, and $\sigma e(2n) = \sigma e(GR)Br(2n)$, where $Br(n)$ and $Br(2n)$ are the effective branching ratios for the n and 2*n* channels and σe(GR) is the effective GR cross section for the laser electron photons in the energy window. Practically, $Br(n)$ and $Br(2n)$ are nearly 1 by selecting the laser electron photon energies as $B(n) \leq E(\gamma) \leq B(2n)$ and $B(2n) \leq E(\gamma) \leq B(3n)$, respectively. Experimentally, we use photons with the spectrum window of $\Delta E \approx \Gamma$. Thus the effective cross section is $\sigma e(xn) \approx 0.7\, \sigma(xn) = 0.7\, Br(xn)\, \sigma(GR)$.

The RI production rate $N(Z, N - x)$ by using the (γ, xn) reaction on the $A(Z, N)$ target nucleus is given as

$$N(Z,N-x) = N'(\gamma)a\sigma^e(xn)N(T) \tag{5}$$

where $N'(\gamma)$ is the number of photons per sec in the energy window of $\Delta E \approx 5$ MeV, a is the attenuation factor of the incident photons through the thick target, and $N(T)$ is the number of target nuclei per unit area. We evaluate the RI production rates in two cases.

In case of FEL, the production rate can be evaluated on the basis of the HIγS data of $N(\gamma) \approx 2 \times 109$/sec for 50 mA electrons with $E(e) = 0.474$ GeV and $E(l) = 1.6$ eV (λ =780 nm).7) The photon intensity increases as $E(e)k$ with k ≈5.

Extrapolating these data, one may assume/expect to get the total number of photons around $N(\gamma) \approx 2\times10^{12}$/sec / 500 mA for $E(e)$=1.2 GeV and the $N'(\gamma) \approx 10^{12}$ /sec for the photons in the energy window. Using a target with thickness of around 30 gr/cm^2 and a ≈ 0.62, the RI production rate for a typical case of A = 100, $Br(n) = 0.7$ and $\sigma(GR) = 0.25\, b$ is given as,

$$N(Z,N-x) \approx 1.5\times10^{10}\ /\text{sec} \tag{6}$$

The photons are well defined into the small angular region of $\theta = 1/\gamma e \approx 4 \times 10^{-4}$ radian, i.e. within a radius r ≈ 0.8 mm at 2 m from the interaction point. Then the target cylinder with 1.6 mm in diameter is 0.6 gr. Thus the RI density after sufficiently long irradiation (multiple of the product half-life) is 1.5×10^{10} /sec/0.6 gr = 0.025 GBq/mg, which is equivalent to 0.025 GBq/ml in case of liquid with 1 gr/cc. Using target nuclei enriched into particular isotopes, one gets efficiently the isotope transmutation, being almost free from other extra/

In case of CO_2 laser photons injected anti-parallel to a beam of GeV electrons in a storage ring, the number of the backscattered photons per sec is given as.8)

$$N(\gamma) = 1 \times 10^8 \frac{lIP}{s} \tag{7}$$

where I is the current of the electron beam and P stands for the power of the laser, respectively in units of A and W. A segment with the length l of the electron beam is assumed to be contained inside the laser beam of the cross section area s, respectively in units of m and mm. A finite Rayleigh length makes s dependent on l. In case of a Gaussian laser beam, the dependence is written as

$$s = \frac{\gamma}{2} \frac{l}{L}, \quad L = \arctan\left(\frac{l\lambda}{2\pi w^2}\right) \tag{8}$$

where λ (10.6μm) in unit of μm and w in unit of mm are, respectively, the wavelength and the waist radius of the laser beam at the middle of the segment l. To enhance N(γ) , one may increase l and reduce w. It is however bounded by a value $N_0(\gamma) = 4.4\times10^7$ I P , which corresponds to a sufficiently large segment length l compared with the Rayleigh length. When a relationship $l \geq 4w^2$ is fulfilled, *N(γ)* counts more than 90 % of N_0.

Low emittance electron beams in the third generation synchrotron light sources allow us to assume w = 0.5 mm for which an adequate segment length is *l*=1 meter. To obtain *N(γ)* = 10^{12}/sec with *I* = 500 mA as considered in the FEL case, the power of the laser is required to be *P* = 46 kW. To be conservative, we may say that a well established technique of the laser backward scattering utilizing a few kW CO_2 laser photons can provide a mean to study nuclear transmutation and RI production with a production rate of an order of 10^9/s.

Radioactive isotopes to be used for PET and SPECT tracers and photonuclear reactions are shown in Table II and Table III.

Table II. Radioactive isotopes to be used for PET tracers and photonuclear reactions.

Isotope	Halflife	Q(EC) keV	Reaction	Abund
^{11}C	20.4 m	1982	^{12}C(γ,n)	98.9
^{13}N	10.0 m	2220	^{14}N(γ,n)	99.6
^{15}O	2.04 m	2754	^{16}O(γ,n)	99.8
^{18}F	109.8 m	1656	^{19}F(γ,n)	100
^{62}Zn	9.2 h	1627	^{64}Zn(γ,2n)	48.6
^{68}Ga	67.6 m	2921	^{69}Ga(γ,n)	60.1

Table III. Radioactive isotopes to be used for SPECT tracers and photonuclear reactions.

Isotope	Halflife d	Q(EC) keV	Reaction	Abund
^{67}Ga	3.26	93, 185	^{69}Ga(γ,2n)	60.1
^{99}Mo/^{99m}Tc	2.75, 0.25	140	^{100}Mo(γ,n)	9.6
^{111}In	2.8	245, 171	^{113}In(γ,2n)	4.3
^{126}I	13	389, 666	^{127}I(γ,n)	100
^{195m}Pt	4.02	259	^{196}Pt(γ,n)	25.4
^{201}Tl	3.04	167	^{203}Tl(γ,2n)	29.5

Intense sources of medium energy photons with *N*(γ) = 10^{13-15}/s may provide RIs around N ≈ 10^{11-13}/s. The RI density is evaluated for a typical case of *E(e)* = 2 GeV with γe=3.9 10^3. Laser electron photons with *E(γ)*=15 - 10 MeV and 24 - 16 MeV for (γ, n) and (γ, 2n) reactions are obtained, respectively, by scattering of 0.24 eV and 0.39 eV laser photons at *θ* = 0 - 0.16 mrad. Thus the collimator to be used for both reactions are the one with aperture of$\Delta\ \theta$ = ± 0.16 mrad. i.e. the radius of 0.65 mm at 4 m from the interaction point. Using a 30 gr/cm2 target, *N* ≈ 10^{11-13}/s can be confined in a cylinder of *r* =0.65 mm with the density of 0.5 - 50 G Bq/mg after long irradiation.

Let us discuss the ^{99}Mo/^{99m}Tc isotopes, which are widely used as SPECT isotopes. The ^{99}Mo isotopes are produced by ^{100}Mo(γ,n) reactions and also ^{100}Mo(γ,p) reactions followed by β− decays. RPIT with *N*(γ) ≈ 10^{13-15}/s and enriched ^{100}Mo isotopes provides the RIs of ^{99}Mo/^{99m}Tc with the production rate of 10^{11-13}/sec and the RI density of 5 10^{8-10} Bq/mg after sufficiently long irradiation.

5. ^{99}Mo/^{99m}Tc and ^{196}Au RI productions by RPIT

^{99}Mo/^{99m}Tc and ^{196}Au RIs were produced by RPIT on 100Mo and ^{197}Au in order to demonstrate the RPIT feasibility. Medium energy photons with *E(*γ) ≈ 16-12 MeV were obtained by using 1.064 μm Nd-YAG4 lasers scattered off 0.95 GeV electrons in the NewSUBARU electron storage ring. A collimator with aperture of 6 mm in diameter was used to select the energy window of ΔE ≈4 MeV. The photon energy window is just adequate to excite preferentially E1 GRs in ^{100}Mo and ^{197}Au. The photon intensity is of the order of 106/sec. Note that the scattered electrons at the forward angle of *θ* ≈0 mrad. are not re-used in the present NewSUBARU with E ≤ 1 GeV, although they are re-used in most storage rings with *E* ≥ 2-3 GeV.

A target used consists of 6 natural Mo disks with 2 mm in thickness and 1 Au disk with 0.5 mm in thickness. Here the Au disk is inserted just between the 3 and 3 Mo disks. Note the natural Mo includes 9.6 %100Mo, while the natural Au is 100 %^{197}Au. They are irradiated by the medium energy photons for 8.89 hrs (hours), and the γ rays from RIs are measured by means of GMX Ge detector after 0.82 hrs from the stop of the irradiation.

The γ ray energy spectrum measured for 1 hr from 0.82 hrs after the irradiation is shown in Fig. 3. The ^{100}Mo stable isotopes were well transmuted to the ^{99}Mo RIs, as shown by the very strong 140.5 keV γ line from the 142.5 keV isomer in ^{99}Tc (T1/2 =6.0 hrs), which were populated from ^{99}Mo ($T_{1/2}$ =66 hrs) decays. Strong 739.5 keV, 778 keV and 181 keV γ lines from ^{99}Mo ($T_{1/2}$ =66 hr) decays are also observed. Note that the strong 140.5 keV γ ray is just the one used widely as the medicine for SPECT. Interesting is to see the 569 keV and 658 keV lines from ^{96}Nb ($T_{1/2}$ =23.4 hrs) and ^{97}Nb ($T_{1/2}$= 72.1 m), which are produced by the (γ,p) reactions on ^{97}Mo and ^{98}Mo, respectively.

The strong 355.5 keV, 333 keV, and 688.5 keV

(333 + 355.5) γ lines are from EC and β+ decays of ^{196}Au and the 426 keV line is from β− decays of ^{196}Au, which are produced by RPIT on ^{197}Au. The 67 keV and 75 keV lines are *K* X-rays from Pt and Pb, respectively.

Relative yields of ^{99}Mo and ^{196}Au isotopes are evaluated by using the measured yields of the 181 keV and 355.5 keV lines from their decays, respectively. They are plotted as a function of the time T from the start of the irradiation as shown in Fig. 4. They are consistent with the known half lives of ^{99}Mo and ^{196}Au.

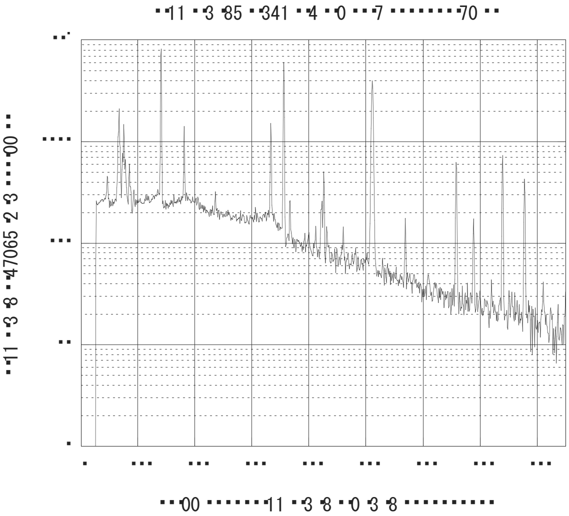

Fig. 3. Gamma ray energy spectrum from RPIT on natural Mo and Au targets. The γ rays at 140.5 keV, 181keV, 739.5 keV, and 778 keV are from ^{99}Mo. The γ rays at 569 keV and 658 keV are from 96Nb and 97Nb, respectively. The γ rays at 333 keV, 355.5 keV, 426 keV, and 688.5 keV(333 + 355.5) are from ^{196}Au. The 66.5 keV and 74.5 keV lines are X rays, while the 511 keV line is the electron positron annihilation.

Effective cross sections for the RPIT (γ,n) productions of ^{99}Mo and ^{196}Au isotopes were evaluated from the numbers of these isotopes produced by the RPIT photon irradiation by using Eq.(5).

The attenuation of the incident photons through the Mo and Au targets is given by a ≈ 0.78 for the present target ensemble.

The effective number of photons, *N'(γ)*, were derived as

$$N(\gamma) = \int N(\gamma, E(\gamma)) dE_{\gamma} \tag{9}$$

where *N(γ,E(γ))* is the energy distribution of the incident photons through the 6 mm dia. collimators. The relative energy distribution of *N(γ,E(γ))* was measured by using a *NaI* crystal.

The number of the ^{99}Mo isotopes are evaluated from the observed yields of 181 keV and 739.5 keV γ rays from the ^{99}Mo decays and that for the ^{196}Au are from the yield of the 355.5 keV γ rays from the ^{196}Au decays, respectively. Here the γ ray yields were corrected for the branching ratios known from the nuclear data[9–11] and the peak efficiencies estimated by using the Monte Carlo simulations.

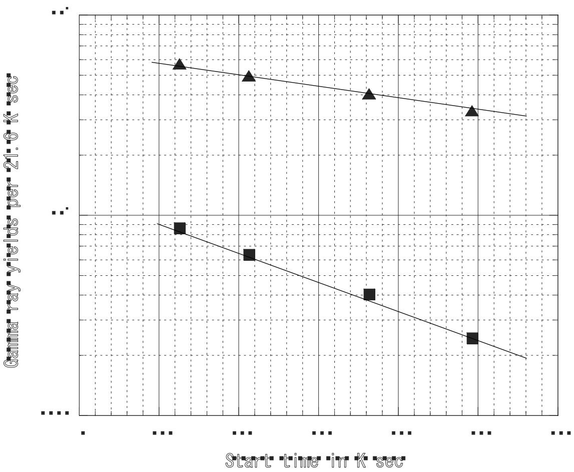

Fig. 4. Relative yields of the 181 keV γ rays from 99Mo (squares) and the 356 keV γ rays from 196Au(triangles) as a function of the time T (K sec) from the start of the irradiation by photons. The irradiation stopped at T = 8.89 hrs (32 K sec) and the γ ray counting started at T= 9.71 hrs (35 K sec). Solid lines are decay curves of the 99Mo ($T_{1/2}$ = 66 hrs) and 196Au ($T_{1/2}$=6.18 d)

Then the effective cross sections are expressed simply as

$$\sigma^{e}(^{99}M) = \frac{N(^{99}Mo)N(^{100}Mo)}{N(^{196}Au)N(^{197}Au)} \sigma^{e}(^{196}Au) \tag{10}$$

$$\sigma^{e}(^{99}M) = k\sigma^{e}(^{196}Au), \quad k = 0.30 \pm 0.05 \tag{11}$$

where *N(C)* and σ*e(C)* are the number of isotopes involved in the present RPIT, and the effective cross section with C standing for the product RIs of ^{99}Mo and ^{196}Au, and for the stable target isotopes of ^{100}Mo and ^{197}Au.

Using the observed excitation function for ^{197}Au[12] and the observed energy distribution of *N(γ,E(γ))*, we get σe(^{196}Au) = 0.365 ±0.012 b, Then the effective cross section for ^{100}Mo(γ,n)^{99}Mo is obtained by using Eq.(11) and the σe(^{196}Au) = 0.365 b as σe(^{99}Mo) = 0.109 ± 0.020 b, including a small contribution from (γ,p) channel. The effective cross sections for the ^{98}Mo(γ, p)^{97}Nb and ^{97}Mo(γ, p)^{96}Nb were evaluated from the observed yields of the 658 keV and 569 keV γ rays from ^{97}Nb and ^{96}Nb,

respectively. They are about 3 % of the effective (γ,n) cross sections. Then, assuming the 3 % contribution to the ^{99}Mo production from the (γ,p) channel, one gets the effective cross section of σe(^{99}Mo) = 0.106 ± 0.020 b. This is in consistent with the value 0.105 b derived from the measured (γ, n) cross section on ^{99}Mo,[13] and is consistent also with the cross section evaluated by using the number of the laser electron photons and the number of the measured ^{99}Mo isotopes.

We note here that the effective (γ,n) cross sections for ^{197}Au and ^{100}Mo are approximately 69% and 62% of the GR peak cross sections of σ(GR), respectively.

6. Concluding remarks and perspectives on photonuclear reactions

The present report shows that RPIT with laser electron photons provides exclusively various kinds of specific/desired isotopes with the large production rate and the high density for basic and applied science. RPIT is of potential interest also for nuclear transmutation of long-lived nuclei. Accordingly, RPIT using intense laser photons and GeV electrons in a storage ring is quite complementary to other methods using high flux reactors and intense charged particle accelerators.

RPIT with large efficiency is quite attractive from ecological view points. Since the GeV electrons stored in most storage rings lose little their energy via interactions with laser photons, they remain in the ring. The laser electron photons are efficiently used for production of desired RIs. Then the overall efficiency of the RI production is many orders of magnitude larger than that of the charged particle accelerators and nuclear reactors. Fast neutrons have recently pointed out to be used for nuclear transmutation.14) This uses a small fraction of the charged particles to produce the fast neutrons, and is complementary to RPIT. Intense electron accelerators provide bremsstrahlung photons for photonuclear isotope transmutation,6) but most of photons are below the threshold energy of the photonuclear reaction and the electrons after the bremsstrahlung are not re-used.

There are several programs of intense photon sources under progress.[4,5,15] MEGa- ray is the project at LLNL for high intensity photons with 1012 photons/sec in the MeV region and ELI-NP is the one at Romania for higher energy photons with 10^{13} photons/sec in the GR energy region of $E(\gamma) \geq 19.5$ MeV. They plan to achieve the intensity of around 10^{15}/sec. In Tokai Japan, the ERL(Energy Recovery Linac) project is under progress to provide intense photons for resonance fluorescence.[16]

It is noted here that the laser photon backscattering off GeV electrons in an electron storage ring is well established and it requires fewer developments compared with linac based facilities like ones planned in Romania and Tokai.

If the natural abundance of the target nuclide is not large, enrichment in the specific isotope is effective to increase the efficiency by the enrichment factor and to reduce other RI productions. Ton-scale enrichment into 100Mo for 99Mo/99mTc and other isotopes are realistic by means of centrifugal isotope separators. Such isotopes are also used for basic science such as neutrino studies in double beta decays.[17] A large scale isotope separation plant with the separation rate of the order of 100 kg/year is interesting for basic and applied science.

RPIT can be used to detect small impurities of specific stable and radioactive isotopes. They are excited by photonuclear reactions via *E1-GR*, and are detected by measuring prompt and delayed gamma rays characteristic of the isotopes of the order of ppb/ppt levels. Thus it can be applied for nondestructive impurity and radionuclide assay.

It is of great interest from scientific and ecological view points to build high intensity electron storage rings and FEL photon sources to provide medium energy photons with intensity of the order of 10^{13-15}/sec. Such intense photons can be widely used for producing byproduct fast neutrons, γ rays and electron positron pairs as well as for the photonuclear RI productions for basic and applied science.

References

[1]A. Bohr and B. Mottelson: Nuclear structure I,II (Benjamin INC, New York 1969, 1975).

[2]H. Ejiri: Proc. Nuclear Materials Workshop, Saskatchewan Canada, April 2010. http://physics.usask.ca/ chang/department/index.html

[3]H. Ejiri and S. Daté: arXiv:1102.4451v1 [nucl-exp]

[4]B. Szpunar and C. Rangacharyulu: Proc. Nuclear Materials Workshop, Saskatchewan Canada, April 2010. http://physics.usask.ca/ chang/department/index.html; Proc. YS4-APSE2010, The 4th Yamada Symposium on Advanced Photons and Science Evolution, ed. H. Ejiri, Osaka, June 2010, http://www.yamadazaidan.jp/ys/apse2010/proceedings.html

[5]D. Habs and U. Koester: arXiv:1008.5336v1 [physics. med-ph].

[6]G. G. Bunatian a, V. G. Nikolenko and A. B. Popov: arXiv 1012.5002v1 [nucl-exp, Dec 2010].

[7]H.R. Weller, M.W. Ahmed, H. Gao, W. Tornow, Y.K. Wu, M. Gai, and R. Miskimen: Prog. Part. Nucl. Phys. 62 (2009) 257. http://www.yunl.duke.du/higs/

[8]S. Daté: Proc. Nuclear Materials Workshop, Saskatchewan Canada, April 2010, http://physics.usask.ca/ chang/department/index.html

[9]B.B. Firestone, V.S. Shirley, S.Y.F. Chu, C.M. Baglin and J. Zipkin: Table of Iso- topes(Wiley-Interscience 1996).

[10]L. Chunmei, W. Gongqing, and T. Zhenlan: Nucl. Data Sheets 83 (1998) 145.

[11]J. K. Tuli, G. Reed, and B. Singh: Nucl. Data Sheets 93 (2001) 1.

[12]A. Veyssiere, H. Beil, R. Bergere, P. Carlos, and A. Lepretre: Nucl. Phys. A 159 (1970) 561.

[13]H. Beil, R. Bergere, P. Carlos, A. Lepretre, A. De Miniac, and A. Veyssiere: Nucl. Phys. A227 (1974) 427.

[14]Y. Nagai and Y. Hatsukawa: J. Phys. Soc. Jpn. 78 (2009) 033201.

[15]C. Barty, Development of MEGa-Ray technology at LLNL, http://www.eli-np.ro/ . http://www.eli-np.ro/executive

[16]R. Hajima, N. Kikuzawa, N. Nishimori, T. Hayakawa, T. Shizuma, K. Kawase, M. Kando, E. Minehara, H. Toyokawa, H. Ohgaki: Nucl. Instr. Meth. A608 (2009) S57.

[17]H. Ejiri: J. Phys. Soc. Jap. 74 (2005) 2101.

Soft X-ray Source by Laser Produced Xe Plasma

S. Amano, K.Masuda, S.Miyamoto, T.Mochizuki
LASTI/UH

Abstract

The laser plasma soft X-ray source in the wavelength rage of 5-17 nm was developed, which consisted of the rotating drum system supplying cryogenic Xe target and the high repetition rate pulse Nd:YAG slab laser. It demonstrated the maximum conversion efficiency of 30% and the soft X-ray generation with the high repetition rate pulse of 320 pps and the high average power of 20 W. The soft X-ray cylindrical mirror was also developed and successfully focused the soft X-ray with an energy intensity of 1.3 mJ/cm^2. The plasma debris mitigation with Ar gas will allow a long lifetime of the mirror and a focusing power intensity of 400 mW/cm^2 with 320 pps. The high power soft X-ray is useful for various applications.

Laser-plasma-X-ray is generated from high-temperature and high-density plasma produced by high-intensity laser. This X-ray source is useful for a lot of applications as a compact light source with high intensity. In order to use this light source for industrial uses, high average power is required. The rotating drum Xe cryogenic target, which could supply continuously solid Xe target for laser-produced plasma soft X-ray, was developed to satisfy this demand.

As shown in Fig.1, spectrum from the Xe has a very broad bandwidth (5-17 nm), so it was expected to be a high efficient soft X-ray source. When a Nd:YAG laser irradiated the target with a laser energy of 800mJ and 300mJ, a maximum conversion efficiency in bandwidth of 5-17 nm was found to be 30 % (Fig.2) and 21 %, respectively. The irradiation laser with a high average power (100 W) and a high repetition rate pulse (320 pps) was also developed originally. It is a PCM-MOPA (Phase Conjugated Mirror – Master Oscillator and Power Amplifier) Nd:YAG slab system. High average output soft X-ray of 20 W at the wavelength range of 5-17 nm was realized by using both the target and the laser.

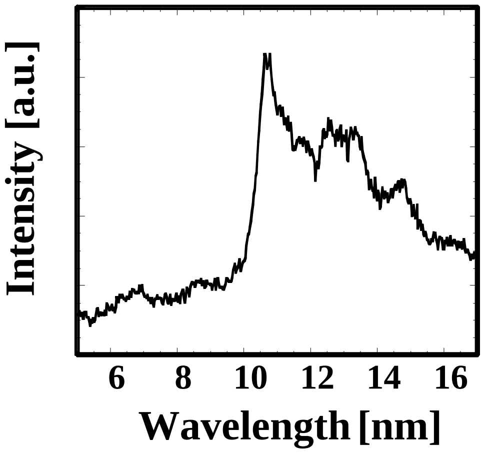

Fig.1 Spectrum of soft X-ray radiation from the rotating cryogenic Xe target.

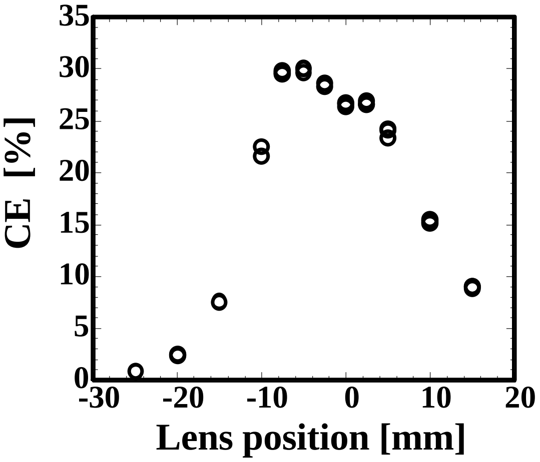

Fig.2 Conversion efficiency (CE) as a function of lens position.

In order to increase an intensity of this soft X-ray, we designed a focusing mirror system. The mirror has a shape of a cylinder with three pieces of cylindrical Ru coated mirror. The piece with an angle of 101 degrees had a curvature radius of 26 mm. The mirror system was placed at a distance of 93mm from a plasma point, that was designed to be maximized a focused X-ray energy by compromising accepted solid angle for the light source and Ru mirror reflectivity. The X-ray energy intensities at a focal plane were measured by a X-ray diode having a sensitivity in 13.5 nm with 2 % bandwidth. Taking account of reflected spectra, the X-ray intensity in the rage of 5-17 nm was estimated as shown in Fig.3. As the measured results, a maximum focused intensity was 1.3 mJ/cm^2. With the mirror, the X-ray intensity at a focal point was improved to be 27-times.

Lithium fluoride plate was used to observe the focused X-ray pattern. X-ray generates color-center in Lithium fluoride. Because a band-gap of lithium fluoride is bigger than 14eV, its color-center can be produced only for X-ray, not visible light and UV light. The produced color-centers emit yellow light by pumping blue light, and we can know a pattern of X-ray by observing the yellow pattern. The measured pattern was in good agreement with a calculated one.

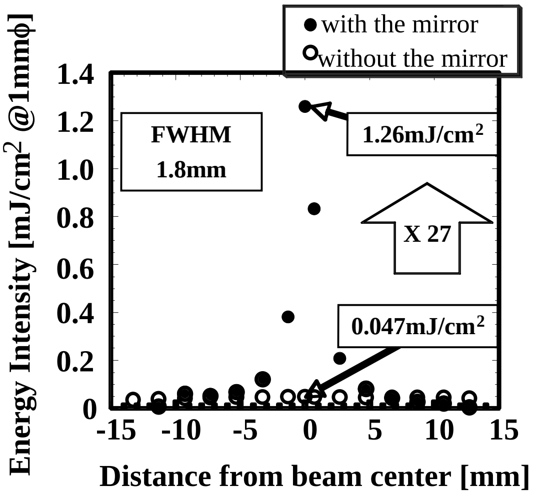

Fig.3 Energy intensity at the focal plane w/o the mirror.

Although Xe is a deposition-free target, mirror sputtering by debris needs to be mitigated. However, the major plasma debris component is ions, and we believe their mitigation to be simple compared with the case of a metal target such as Sn, using magnetic/electric fields and/or gas. We are now studying debris mitigation by Ar buffer gas. Ar gas was chosen because of its higher stopping power for Xe ions and lower absorption of X-ray, and its easy handling and low cost. After the vacuum chamber was filled with Ar gas, total erosion rates were measured using a gold-coated quartz crystal microbalance (QCM) sensor placed 77 mm from the plasma at a 45-degree angle, and simultaneously, X-ray losses were monitored by an X-ray diode placed 200 mm from the plasma at a 22.5-degree angle. Figure 4 shows the erosion rates as a function of Ar gas pressure. The rates were normalized by the erosion N_0 at a pressure of 0 Pa. When the Ar pressure was 8 Pa, we found the erosion rate was 1/18 of that without the gas, but the absorption loss for EUV light was only 8%. The erosion rates (N/N_0) in Fig. 4 can be fitted to an exponential curve:

$$N\left(P_{Ar}\right) = N_0 \cdot \exp\left(-\frac{P_{Ar}}{kT}\sigma l\right),$$

where P_{Ar} is the Ar pressure, k is the Boltzmann constant, T is the gas temperature, σ is the cross section and l is the debris flight length. From this fitting, we obtain $\sigma = 2.0 \times 10^{-20}$ m^2. The Ar buffer gas successfully mitigated the effect of plasma debris with little X-ray attenuation. Increasing the Ar pressure, mirror erosion decreases but X-ray attenuation increases. Compromising the erosion and X-ray attenuation, an optimized pressure is achieved. We should localize the higher density Ar gas to only the debris path so that EUV attenuation is as small as possible. We can design the optimized pressure condition using the σ value obtained and we consider the use of an Ar gas jet. Through this mitigation, we expect that erosion will be reduced by more than two orders of magnitude and the lifetime of the mirror will be extended.

This debris mitigation allows our LPP source to continuously operate with the longer mirror liftime and achieve a focusing power intensity of 400 mW/cm^2 with 320 pps. This high power soft X-ray is useful for various applications.

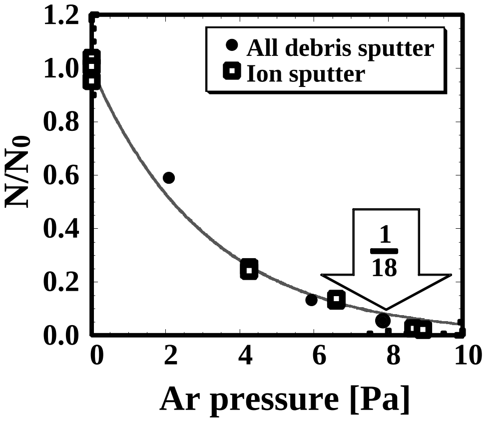

Fig.4 Normalized sputtering rate vs. Ar pressure.

References

[1] S.Amano *et al.*, IEEJ Trans. EIS, **130**, pp.1768(2010).

Characterization of a laser-plasma extreme-ultraviolet source using a rotating cryogenic Xe target

S.Amano, K.Masuda, A.Shimoura, S.Miyamoto, T.Mochizuki
LASTI/UH

Abstract

A laser-plasma source for extreme-ultraviolet (EUV) light that uses a rotating cryogenic solid-state Xe target has been characterized. We focused on parameters at the wavelength of 13.5 nm with 2% bandwidth required for an EUV lithography source and investigated improvements of the conversion efficiency (CE). With the drum rotating, there was an increase in CE and less fast ions compared with the case for the drum at rest. It is considered that the Xe gas on the target surface can produce optimal-scale plasma, satellite emission lines in Xe plasma effectively increase the EUV intensity, and the ion number is decreased by the gas curtain effect. The dependence of CE on the laser wavelength, laser energy and intensity also studied. As a result, the maximum CE was 0.9% at 13.5 nm with 2% bandwidth under the optimal condition. By continuous irradiation of a Nd:YAG slab laser at a repetition rate of 320 Hz and an average power of 110 W, the target continuously generated EUV light with an average power of 1 W at 13.5 nm with 2% bandwidth.

Introduction

Recently, there has been strong expectation of using an laser-produced-plasma (LPP) x-ray source as a light source for x-ray projection lithography, which is referred to as extreme ultraviolet (EUV) lithography and is expected to be used for the mass production of next-generation semiconductor chips. For this purpose, great efforts have been made to develop such an LPP-EUV source.

Light at 13.5 nm with 2% bandwidth is required for the EUV light source, which is limited by the reflectivity of Mo/Si mirrors in a projection lithography system. Xe and Sn as plasma targets have been studied intensively because they have strong emission around 13.5 nm. The emission peak from a Sn target is at 13.5 nm, therefore Sn intrinsically has a high EUV conversion efficiency (CE) at 13.5 nm with 2% bandwidth. However, such a metal target would deposit and remain on EUV mirrors near the plasma, degrading their reflectivity in a short period. On the other hand, Xe is an inert gas and does not deposit on mirrors, and it has been studied as a deposition-free target. Unfortunately, its emission peak is at 10.8 nm. Improvement of the CE is a critical issue for the Xe target.

We chose Xe as a deposition-free target and developed a rotating cryogenic drum target system, which could continuously supply a solid Xe target. We also developed a drive laser, which was a phase conjugated–maser oscillator power amplifier Nd:YAG slab system with a pulse repetition rate of 320 Hz. Using the above, we constructed an LPP-EUV light source system and were able to continuously generate EUV light. In this paper, we report the performance of the EUV light source, especially the improvements of the CE at 13.5 nm with 2% bandwidth.

Experiments

A cylindrical drum in a vacuum chamber is filled with liquid nitrogen, and thereby the copper surface is cooled to the temperature of liquid nitrogen. Xe gas blown on the surface is condensed to form a solid Xe layer. The drum coated by the solid Xe layer rotates around the vertical z-axis and moves up and down along the z-axis during rotation, moving spirally so that a fresh target surface is supplied continuously for every laser shot. Two wipers are mounted on the container wall to adjust the thickness of the solid Xe layer to 500 μm and assist in recovering the laser craters on the target. The thickness of 500 μm was found to be sufficient for a laser shot of 1 J not to damage the drum surface.

Figure 1 shows the experimental setup to obtain data of EUV emission from the cryogenic Xe target on the rotating drum. Here, a conventional Q-switched Nd:YAG rod laser was used in single-shot operations, which could deliver pulses at wavelengths of 1ω (1064 nm), 2ω (532 nm) and 3ω (355 nm). The laser pulse width was about 10 ns. The pulses were expanded by a beam-expander and focused on the target by a lens with a focal length of 500 mm so that plasma was produced and emitted EUV radiation. By changing the position of the focusing lens to change the laser spot, the laser intensity on the target was adjusted to find the optimum intensity. We note the lens position (LP) is zero at best focus, negative for in-focus (the laser spot in the target before focus) and positive for out-of-focus (beyond focus). An EUV energy detector calibrated absolutely (FC) (SCIENTEC Engineering, Flying Circus) and a relative energy monitor (EM) comprising an x-ray diode with Mo/Si filter (IRD, AXUV-20) and a Mo/Si mirror were used. Spatial distributions of the EUV emission were measured by scanning the EM on a rotating stage. A charge collector (CC) detected the plasma ions.

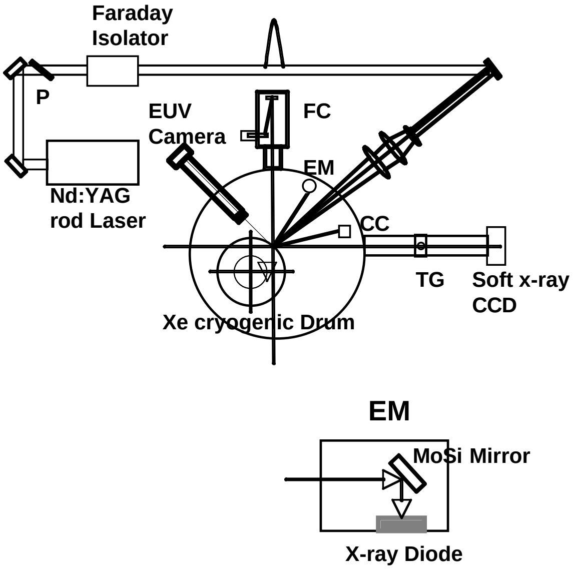

Figure 2. Experimental setup to obtain data of EUV emission from the cryogenic Xe target on the rotating drum.

Results

We investigated the CE from the laser to EUV using the 1ω laser pulse. Figure 2 shows the CE per solid angle as a function of LP (laser intensity), which was measured by the FC located at 45 degree from the laser incident axis. The laser pulse energy was 0.8 J. We see that the CE was enhanced under the rotating drum condition compared with the rest condition. Here, the rest condition is as follows. Xe gas flow is stopped (0 mL/min) after the target layer has formed, and the drum rests (0 rpm) during a laser shot and stepwise rotates after every shot so that a fresh target is supplied to the point irradiated by the laser. The rotation condition is as follows. Laser pulses irradiate quasi-continuously the target on the rotating drum, supplying Xe gas (40 mL/min) and forming the target layer. Here, the rotating speed was 130 rpm. In Fig. 2, we see that the maximum CE per solid angle was for an optimized laser intensity of 1×10^{10} W/cm^2 (LP = –10 mm) during rotation. Measurement of the EUV angular distribution by a scanning EM shows that the distribution can be expressed by a fitting curve of $(\cos\theta)^{0.38}$. Taking into account this distribution, we obtained the maximum spatially integrated CE of 0.9% at 13.5 nm with 2% bandwidth.

For the drum rotating operation, we found the good characteristics of not only increased CE but also less fast ions compared with the case with the drum at rest. The cause of the phenomena was considered to be Xe gas localized on the target surface by the wiper. We supposed that the gas produces optically thick plasma, satellite lines in Xe plasma would contribute effectively to increasing the EUV intensity, and the ion number is decreased by the gas curtain effect.

The laser wavelength dependency of the CE was investigated and it was found that the maximum CE was obtained for the 1ω laser and the rotating drum target. It was also found that laser energy of more than 0.3 J was sufficient to achieve the maximum CE with an optimal laser intensity of ~10^{10} W/cm^2. In conclusion, the maximum CE was found to be 0.9% at 13.5nm with 2% bandwidth for the optimal condition, and this value is higher than that for a Xe gas or liquid state target but lower than that for a Sn target.

When a slab laser having a repetition pulse of 320 Hz and an average power of 110 W irradiated the rotating target, continuous EUV generation was achieved with average power of 1 W at 13.5 nm with 2% bandwidth. The moving average of the EUV energy stability over 50 pulses was estimated to be 3% (1σ), but it could be improved using a laser-diode pumping laser. Using a higher-power drive laser with a repletion rate of 10 kHz and laser energy of 1 J, EUV power of 100 W at 13.5 nm with 2% bandwidth will be obtained. No degradation of the Mo/Si mirror reflectivity up to 10^6 shots was recognized. The main plasma debris from the Xe solid rotating target was plasma ions and it is thought that they can be mitigated easily compared with debris from a Sn target.

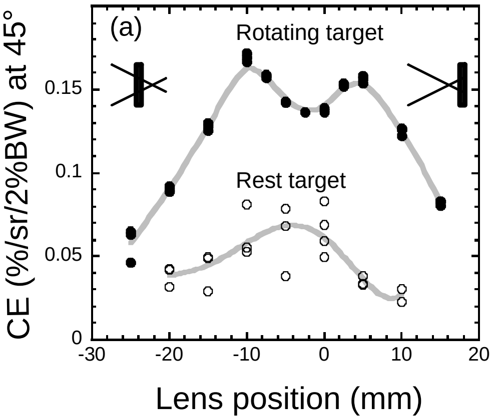

Figure 2. CE as a function of LP in the rotation (130 rpm) and at-rest (0 rpm) conditions. Insets show the laser beam focusing on the target.

References

[1] S.Amano *et al.*, Appl.Phys.B, **101**,213 (2010).

Soft X-Ray from Laser-Produced Xe and Sn Plasmas in a Wide Wavelength Range

Tomoaki Inoue, Takayasu Mochizuki, Shuji Miyamoto, Sho Amano,
Takeo Watanabe, and Kazuhiro Kanda

Abstract

Soft x-ray conversion efficiencies in a 5–17-nm wavelength range in xenon and tin plasmas produced by a 1.06-μm Q-switched neodymium-doped yttrium aluminum garnet laser were found to be extremely high. They were measured to be 25% and 20% for the xenon and tin plasmas, respectively, at a laser intensity of about 2×10^{10} W/cm^2. These results indicate that a stand-alone soft x-ray source using a laser-produced xenon or tin plasma is useful for various applications that require intense, soft x-ray photons in a wide wavelength range.

Introduction

Soft x-rays from high-temperature, high-density plasmas produced by focusing a high-intensity laser pulse on target materials are expected to be useful for various applications. These include extreme ultraviolet lithography (EUVL) that requires an intense output power at 13.5 nm within a bandwidth of 2%,[1] and material processes that require a bulk number of photons with a much wider bandwidth. We have studied soft x-ray generation in laser-produced plasmas using tin, xenon, and lithium targets.[2,3,4] N. Matsuo et al found that laser-plasma soft x-ray irradiation before excimer laser annealing (ELA) reduced the critical energy density for the start of crystallization of a-Si film.[5] The effect they observed will enable us to realize a low-temperature process for ELA crystallization.[6]

A cryogenic xenon target efficiently emits a large number of soft x-ray photons with an intense spectral peak at 10.8 nm,[2] whereas a tin target emits 13.5-nm photons selectively and efficiently.[3] The conversion efficiency (CE) at 13.5 nm within a bandwidth of 2% has been intensively studied.[7] However, the CEs in a cryogenic xenon target and a tin target in a wide soft-x-ray wavelength range have not been reported yet, to the best of our knowledge.

In this paper, we report on soft-x-ray CEs spectrally integrated in a 5–17-nm wavelength range in cryogenic xenon target and planar tin target plasmas produced by a 1.06-μm Q-switched neodymium-doped yttrium aluminum garnet (Nd:YAG) laser.

Experiments and Results

In the present experiment, a cryogenic xenon drum target was used in an irradiation chamber. The target is described in detail elsewhere.[8] Here we describe it briefly. A xenon target layer was formed on the surface of a rotating copper drum that was cooled by liquid nitrogen inside the drum. The thickness of the target layer was adjusted to be about 500 μm during rotation by two wipers that were installed inside the cover on the drum. The rotation speed was set to 130 rpm so that the lasers focused spot would not overlap the previous shot's spot even at a laser-pulse repetition rate of 320 pps.[9,10] A Q-switched 1.06-μm Nd:YAG rod laser was focused through a f/500 lens down to a minimum spot diameter of 50 μm on the drum target surface. The laser pulse duration and pulse energy were 8 ns at FWHM and about 300 mJ/pulse, respectively. The laser intensity was adjusted by changing the lens position (LP). The vacuum pressure in the irradiation chamber was maintained at less than 0.2 Pa by using a turbo-molecular pump when the xenon target gas was loaded into the drum chamber as the drum rotated. A Flying Circus 3 (FC3) was mounted at −45 degree to measure the plasma emission energy.[11] The FC3 was composed of a Mo/Si mirror, a Zr filter, and an x-ray photodiode, and it was absolutely calibrated in energy sensitivity for a bandwidth of 13.5 nm ± 1%. An x-ray calorimeter was mounted at 22.5 degree. The plasma emission spectrum between 5 and 17 nm was observed using a transmission grating spectrometer (TGSM) mounted at 45 degree. The TGSM was consisted of a transmission grating and a charge-coupled device (CCD) camera. The characteristics of the transmission grating were studied by K. Eidmann et al,[12] and the wavelength sensitivity of a pixel in the CCD camera was studied by Yuelin Li et al.[13]

By using the absolute energy at 13.5 nm ± 1% in the FC3 as a reference and combining it with the relative x-ray spectral intensity, we obtained the total, absolute x-ray emission energy integrated for the 5–17-nm range. In separate experiments, we found that angular distribution of the x-ray emission was $(\cos\theta)^{0.38}$ by monitoring the x-ray calorimeter signals at different angles.[14] Therefore, here we assumed the above angular distribution in 2π space for the x-ray emission. CE was then derived by dividing the x-ray energy integrated by the incident laser energy.

The experiment was performed with a single laser shot in two modes, in which the xenon target was rotating or stationary, respectively. For comparison, a similar experiment was performed using a planar tin target. The x-ray energy from the tin plasma at 5–17 nm was evaluated using an x-ray calorimeter calibrated by FC3, as previously described for the xenon target.

X-ray spectra obtained for the 5–17-nm wavelength range from the rotating xenon target, the stationary xenon target, and the planar tin target are shown in Fig. 1. The LP was fixed at −5 mm, where the measured CE was about the maximum for each target. The x-ray spectrum of the tin plasma had an intensity peak at 13.5 nm attributable to the 4d–5p transition in tin ions. The spectrum profile in the xenon plasma varied significantly, and the x-ray conversion efficiency increased as the xenon target rotated. The spectrum for the rotating xenon target had a broader bandwidth than that for the tin target.

The maximum soft x-ray CEs for the xenon and tin plasmas were measured to be about 25% and 20%, respectively, between 5 and 17 nm at about LP = −5 mm, where the laser spot size on the target surface was about 500 μm (FWHM), and thus, the laser intensity was evaluated to be about 2×10^{10} W/cm^2.

The intensity at 12–16 nm in the cryogenic xenon target was enhanced by a factor of about 3 by rotating the target. This suggests that the two wipers increase the surface temperature of the target layer, thereby preforming a xenon gas layer on the surface of the cryogenic target while the drum rotates. The result is a plasma density profile having a relatively long scale length in the target plasma. Such a density profile would lead to an increase in the optical thickness, which makes the emission spectrum more blackbody-like.

From the above results, we concluded that the CE in the cryogenic xenon target is as high as that in the tin target. However, although the tin target would be prepared as micro-droplets by using a jet nozzle system, it still produces plasma debris that tend to deposit on the x-ray optics unless a strong magnetic field is provided for ion shielding.[15] A buffer gas method would be a simple and effective method of shielding the optics against bombardment by fast ions for any target.[16] Nevertheless, it would be difficult to stop the tin ions from being deposited on the optics after they have been decelerated or neutralized by collisions with buffer gas molecules and have started to drift slowly in the chamber. Therefore, using the cryogenic xenon target seems more realistic than using the tin target for soft x-ray generation for long-term operation if we need not require such a narrow band width as ±1% for EUVL.

In conclusion, we obtained CEs as high as 25% and 20% in laser-produced xenon and tin plasmas, respectively, for the 5–17-nm wavelength range. These results indicate that a stand-alone soft x-ray source using a laser-produced xenon or tin plasma is useful for various applications that require intense, soft x-ray photons in a wide wavelength range. A practical, intense, soft x-ray source may be more easily realized with a cryogenic xenon target than with a tin target. The soft x-rays from the laser-produced plasma are intrinsically pulsed and yield significant CEs such as those we obtained. A high soft-x-ray irradiation intensity of more than 10^4 W/cm^2 may be easily achieved at a focus zone of several millimeters in diameter with condenser optics, which may enable us to use new material processes.

Part of this work was supported by a Grant-in-Aid for Scientific Reserch C(#21560752) from The Ministry of Education, Culture, Sports, Science and Technology (MEXT) of Japan.

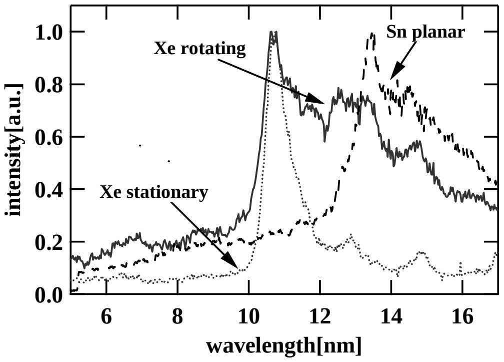

FIG. 1. X-ray spectra from a rotating Xe target (solid line), a stationary Xe target (dotted line), and a planar Sn target (dashed line) with a lens position of −5 mm.

[1] EUV source for Lithography, edited by V. Bakshi (SPIE, Washington, 2005), p4.
[2] Atsushi Shimoura et al, Appl. Phys. Lett. **72**, 164 (1998).
[3] Takayasu Mochizuki, EUV R&D report (2003), p105-114, sponsored by EUVA.
[4] Akihisa Nagano et al, Appl. Phys. Lett. **90**, 151502 (2007).
[5] Naoto Matsuo et al, Jpn. J. Appl. Phys. **46**. (2007), 1061-1063.
[6] Naoto Matsuo et al, J. Jpn Inst. Metals. **51** (2010),1490-1493.
[7] Shuji Miyamoto et al, Appl. Phys. Lett. **86**, 261502 (2005).
[8] Keisuke Fukugaki et al, Rev. Sci. Instrum.**77**, 063114 (2006).
[9] Takayasu Mochizuki, Proc. SPIE. **3886**, 306 (2000).
[10] Takayasu Mochizuki et al, Proc. SPIE. **4504**, 87 (2001).
[11] S. A. van der Westen et al, ISMT Technology Transfer Report, 04024490A-TR (2004).
[12] K. Eidmann et al, Journal of X-ray Science and Technology **2**, 259-273 (1990).
[13] Yuelin Li, G. D. Tsakiris, and R. Sigel, Rev. Sci. Instrum. **66** (1), 80 January (1995).
[14] S. Amano et al, Appl. Phys. B **101** ,213 (2010).
[15] Sho Amano et al, Rev. Sci. Instrum **81**, 023104 (2010).
[16] Francesco Flora, Luca Mezi et al, Proc. SPIE. **4504**, 77 (2001).

Study on Powder Transport
Using Surface Acoustic Wave Actuator

Hikaru Tomita*, Tsunemasa Saiki**, Nozomu Araki*, Yuichi Utsumi*
* Laboratory of Advance Science and Technology for Industry, University of Hyogo, Japan
****** Hyogo Prefectural Institute of Technology, Japan

Abstract

Surface acoustic wave (SAW) devices are expected for micro total analysis systems, because their structures are simple. We studied powder transport using SAWs. In this study, we investigated powder transport characteristic using SAWs as the relationship between the electric power applied to a SAW actuator and the moving speed of powder. As a result, we found that the possibility of controlling the amount of powder transport by adjusting the electric power applied to the IDT and the application time was demonstrated and powder can be transported efficiently by optimizing the IDT's parameter.

Introduction

The manufacturing process of each device in a lab on a chip must be simplified so that many small devices can be integrated. Surface acoustic wave (SAW) actuators with very simple structures have attracted interest. Therefore, we fabricated SAW drive pumps and created a continuous flow of liquid by optimizing interdigital transducers (IDTs) that generate the SAWs [1]. Moreover, we fabricated a high efficiency mixing chip for synthesizing—one that is operated only using the SAWs [2]. We also speculated that powder can be transported by using the SAWs because they had been found to move solids [3]. If powder transport on a µTAS is possible, we can apply it to transporting micro beads or to separating a micro channel and to acquiring solid fragments precipitated in a liquid phase as the unit chemical operation in solid synthesis. Processes like these would enable extending the application range of the SAW actuators. However, the process requires a precise amount of bead movement. Thus, we investigated as transport characteristic using SAWs the relationship between the electric power applied to a SAW actuator and the moving speed of powder.

Experimental Setup

Our experimental setup of powder movement using SAWs is shown in Fig. 1.

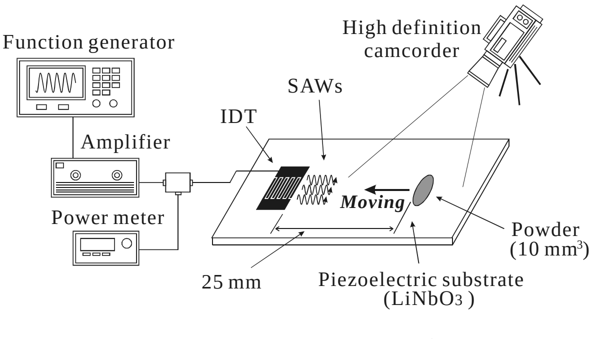

Figure 1. Experimental setup for observing powder movement using SAWs.

In the experiment, a function generator created 1-kHz burst waveforms consisting of 1000 cycles of 19.2 MHz sine waves, and an amplifier boosted the burst waveform voltage. When the burst waveform voltage was applied to an IDT electrode patterned on a piezoelectric substrate (127.8° y-rotated x-propagating LiNbO3), SAWs were generated. The SAWs propagated through the surface layer of the piezoelectric substrate and arrived at a 10-mm3 powder located about 25 mm from the IDT. Here, we used two copper powders, whose specific gravity is 8.9, as shown in Fig. 2. The diameters of powder are 10µm and 100µm. The powder then became energized due to the SAWs, and it moved to the upper stream of the SAWs, as shown in the sequential photographs taken using a high-definition camera of Fig. 3. Incidentally, the moving speed of the powder can be obtained from photographs like these by using the reaching distance and time.

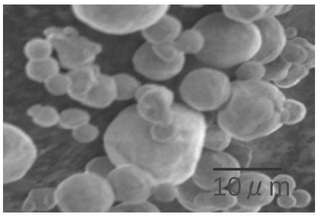

(a) 10µm copper powder

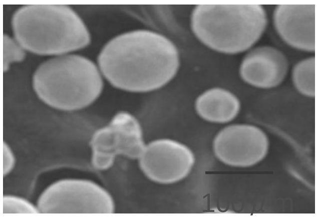

(b) 100µm copper powder

Figure 2. SEM images of copper powder used for experiment.

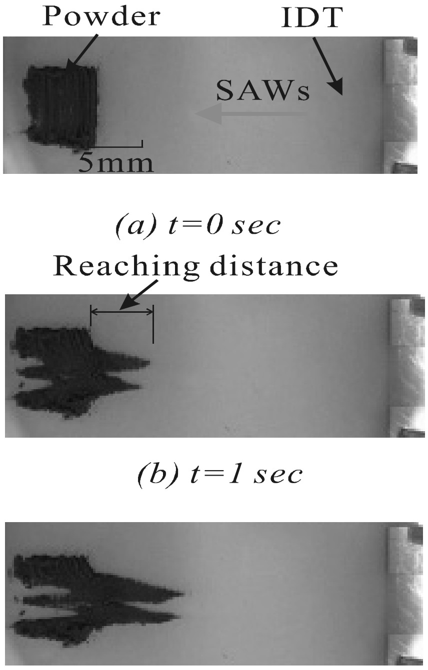

(a) t=0 sec

(b) t=1 sec

(c) t=2sec

Figure 3. Sequential photographs of powder movement using SAWs (Applied electric power: 420 mW).

Experiment and results

We investigated the relationship between the moving speed of the powders and the electric power applied to the IDT. Here, Stripline pitch of IDT is 200μm. The result is shown in Fig. 4. The moving speed increased as the applied electric power increased. When 1440 mW of electric power was applied to the IDT, the moving speed of 10μm powder was the third faster than it of 100μm powder. Those result demonstrated the possibility of controlling the amount of powder transport by adjusting the electric power applied to the IDT and the application time.

Next, we investigated the relationship between stripline pitch and transporting efficiency of powder. Here, Stripline pitches of IDT are 40, 80 and 200μm and powder is 10μm copper powder. The result is shown as Fig. 5. When the stripline pitch was changed, the transporting efficiency of powder was changed. When pitch was 80μm, the transporting efficiency of powder was the highest. Those facts let us to the conclusion that powder can be transported efficiently by optimizing the IDT's parameter. Therefore, we will systematically investigate this relationship to design powder transport actuators.

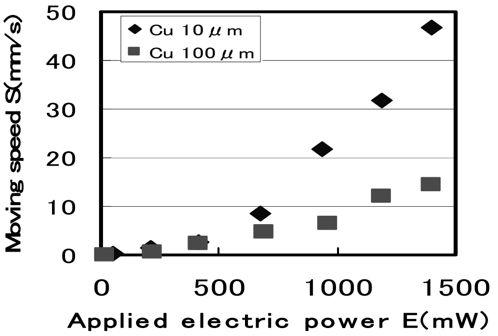

Figure 4. Relationship between moving speed of powder and electric power applied to IDT.

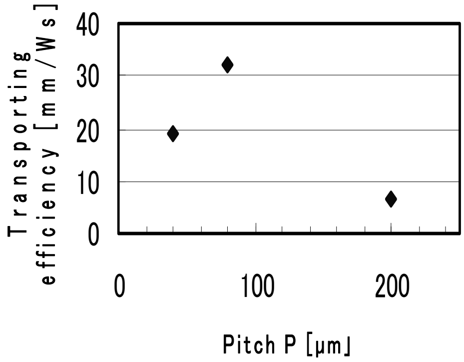

Figure 5. Relationship between stripline pitch and transporting efficiency of powder.

References

[1] Y. Utsumi, T. Saiki and K. Okada, "Proposal of a Novel Continuous Flow Pumping Operated by Surface Acoustic Wave," 12th International Conference on Miniaturized Systems for Chemistry and Life Sciences (μTAS2008), 715 (2008).
[2] T. Saiki, K. Okada and Y. Utsumi, "High Efficiency Mixing and Pumping of Continuous Liquid Flow using Surface-Acoustic-Wave", 13th International Conference on Miniaturized Systems for Chemistry and Life Sciences (μTAS2009), 58 (2009).
[3] M. Kurosawa, M. Takahashi and T. Higuchi, "Ultrasonic Linear Motor using Surface Acoustic Waves", IEEE Transactions on Ultrasonics, Ferroelectronics, and Frequency Control, 43, 901 (1996)

HIGH-SENSITIVE DETECTION OF POLYCHLORINATED BIPHENYL ON THREE-DIMENSIONAL LAB-ON-A-CD

Hiroki Nose*, Tsukasa Azeta*, Yoshiaki Ukita**, Saki Kondo*, Chiwa Kataoka***, Yuzuru Takamura**, and Yuichi Utsumi**
*Laboratory of Advanced Science and Technology for Industory, University of Hyogo, JAPAN
**School of Material Scinence, Japan Advanced Institute for the Science and Technology (JAIST), JAPAN
***Carbuncle Bioscientech LLC., JAPAN

Abstract

This paper presents high-sensitivity detection of poly-chrolinatedbiphnenil in three-dimensional lab-on-a-CD, which consists of multiple disks with three-dimensional microchannel networks. To perform the automatic sequencing of competitive protocol, capillary barrier type passive valves with vertically embedded capillary valve is designed and fabricated. We successfully demonstrated the detection of poly-chrolinatedbiphenil. It is notable that the reproducibility of the detection is strongly epending on the quality of scaffold and it is suggested that detection with concentration of sample down to 0.01ng/ml is possible.

Introduction

The importance of fast and low cost immunoassay, such as enzyme-linked immunosorbent assay (ELISA), has been recognized for advanced diagnosis systems. Lab-on-a-CD has many advantages, small sample volume consumption, high-speed reaction, large-scale and parallel assays, and compact system. However it has many issues to be addressed. Especially, the development of highly-functionalized and highly-integrated microsystems and high-sensitive and reliable accuracy is necessary for wider applications. Moreover the automatic parallel operation of multiple microreactors is also important for high-performance system to improve the convenience and accuracy. The concept of centrifugal microfluidics realize fully automated microfluidic systems without external syringe pumping systems.

We have been proposed vertical microreactor stack with multifunctional capillary bundle structure realizing integrated system with multiple components with different functions. The capillary bundle structure has been used due to its multiple functions and unique characteristics of high-efficiency microreaction, high-efficiency mixing, and 3D optical detection design.

As shown in the fig. 1(a), our lab-on-a-CD consists of planer microchannel disk of PDMS and through-hole disk of PMMA disk. These disks are stacked and reversibly bonded together to construct 3D microchannel network. As shown in fig. 1(b), stacked structure contributes to enhance surface area for antibody immobilization by using bundle-like capillary structure and optical path length of the detection reservoirs are also increased. The stack structure of our device also contributes to reduction of space consumption of the each module by increasing the thickness of reservoirs up to 700µm, thus we succeeded in to integrate 10 microreactors on an 8cm-disk. Figures 2 shows the photographs of planer microchannel disks of PDMS and through-hole PMMA disk, which fabricated by standard rapid prototyping and deep X-ray lithography. As shown in fig. 2(b) bundle-likes capillary structure of square-shape capillaries (75µm in diameter) are formed on the PMMA disks for the effective immobilization of antibody.

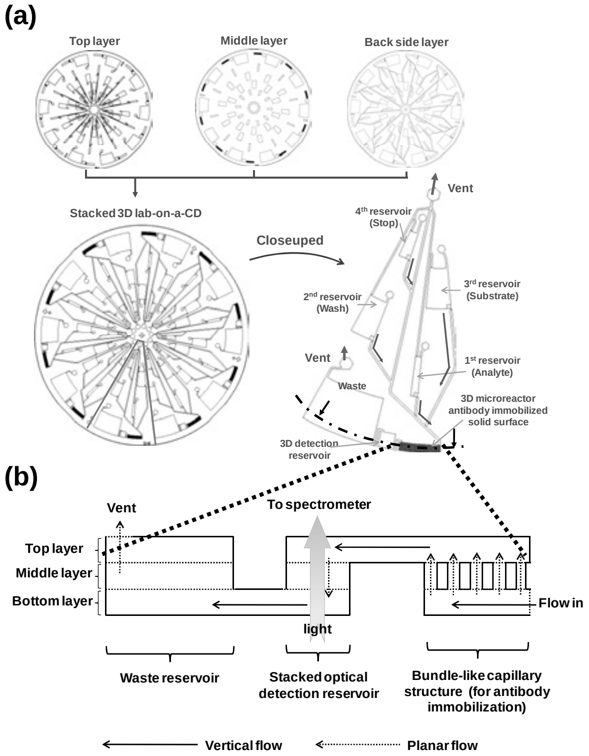

Figure 1. The schematic illustration of three-dimensional lab-on-a-CD. (a) Multiple layers of disks are stacked and bonded each other, to construct 3D microchannel networks. (b) Cross section of the 3D reaction chamber and optical detection reservoir.

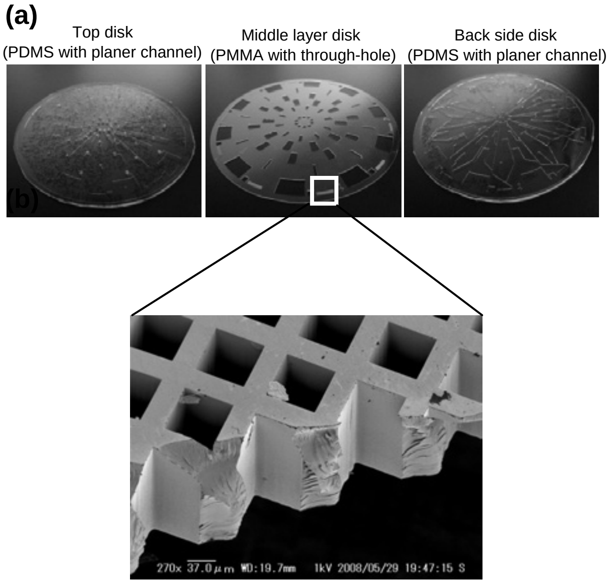

Figure 2. (a)Photographs of fabricated disks of 3D lab-on-a-CD. (b)SEM image of bundle-like capillary structure for antibody immobilization.

Experiments and Results

To demonstrate the detection of PCB, bundle-like capillary structure is immobilized with anti-PCB antibody and blocked with BSA by off-chip immobilization. Then the disk is reversibly bonded with PDMS (also blocked) to construct 3D lab-on-a-CD.

We found out the strong effect of micromachining accuracy of the bundle-like capillary structure onto the reproducibility of the assay. The Table 1 shows simultaneously taken results of the three results of tests with same condition. As shown in Table 1, the reproducibility of the signal intensity is indeed good (error below the 5%) by using X-ray lithography with improved machining accuracy.

Table 1 *Reproducibility of the B0. The error of the test is less than 5% in n=3*

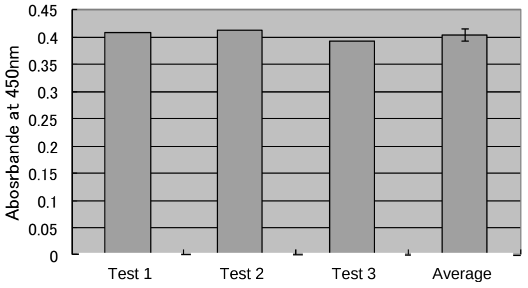

We demonstrated competitive ELISA and Table 2 shows the result of the ELISA. The measurements corresponding to each plot are simultaneously carried out on same chip of three-dimensionally stacked detection reservoirs by means of absorption spectroscopy. As shown in Table 2, the decreasing signal with analyte concentration clearly suggests successful detection of PCB. Estimated detection limit is less than 0.01ng/ml, and the sensitivity is comparable to the commercially available ELISA kit, however it is expected that the further improvement can be achieved by optimizing the protocol and the device.

Table 2 *Obtained calibration curve by using three-dimensional lab-on-a-CD. The signal of the enzyme reaction is amplified by high-sensitive peroxidase substrate(TMBZ).*

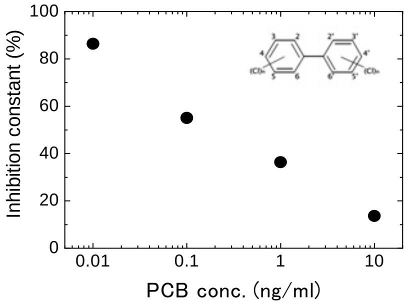

References

1. "A fully automated immunoassay from whole blood on a disk" B. S. Lee *et al.*, *Lab Chip*, **9**, 1548, (2009)
2. "Design of a compact disk-like microfluidic platform for enzyme-linked immunosorbent assay" S. Lay *et al.*, *Anal. Chem.*, **76**, 1832, (2004)

Fabrication of Integrated Magneto Impedance Sensor for Medical Monitoring

Y. Yoritama[1], M. Yoshida[1], R. Takahashi[1], T. Uchiyama[2], A. Yamaguchi[3], Y. Utsumi[1]
[1]University of Hyogo, [2]Nagoya University, [3]Keio University

Abstract

For medical monitoring, we fabricate integrated Magneto Impedance (MI) sensor. The sensor is magnetic sensor using skin effect. The fabricate process is complex consisting lithography process, sputtering process and electroplating process. Therefore, we optimize the process through repeated study of the chemical resistance of various materials and procedures, aimed at completion of the sensor.

Introduction

Recently, the relationship between heartbeat fluctuations and diseases such as the diabetes mellitus is very much noticed. By developing the system that always monitors the heartbeat, it is expected that it may be connected for the early detection of various diseases. The strength of the biomagnetic field is about 10^{-10} to 10^{-13}T. Generally, measurement of such a small magnetic field had to be measured by the use SQUID (Superconducting QUantum Interference Device). But this sensor has the disadvantage that need to cool the sensor unit. In contrast, MI (Magneto Impedance) sensors could be used at room temperature, so it has attracting attention at present. In addition Generally magnetic sensor detect the magnetization of the magnetic material to measure magnetic field. If you downsize the sensor, the accurate measurement become difficult by be affected demagnetizing field. However MI sensor has a measurement principle that doesn't use the magnetization of the ferromagnetic. So the downsizing of sensor unit is easy.

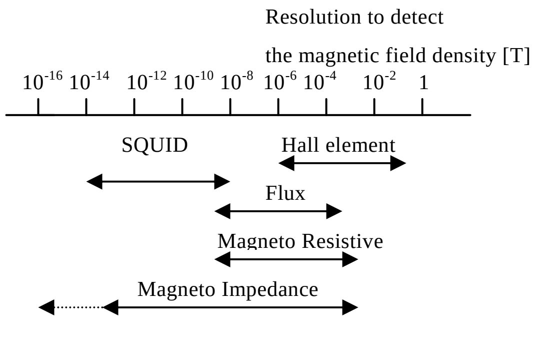

Fig.1 Magnetic sensor type and resolutions.

Sensor Design

The structure of our MI sensors is form the pickup coil was wrapped around a ferromagnetic sensor units (Fig.2). Pickup coil can detect of the signal from the ferromagnet without noise. There is the insulation layer between the ferromagnetic and the pickup coil.

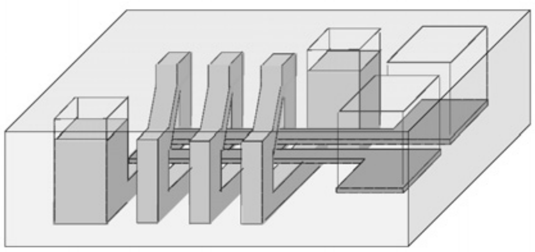

Fig.2 The image of our MI sensor

Fabrication Process

We designed the fabrication process of the sensor by stacking multiple layers of insulation, and forming a three-dimensional coil pattern into insulation layer.

The fabricated process consists of lithography process, sputtering process and electroplating process. The insulation layer (SU-8) of the internal structure is formed by lithography process. Next, we fabricate coil by electroplating, and pattern 2nd insulation layer on it.

On the 2nd layer, sputtered high permeability alloy (Ni-Fe, permalloy). After that in the same way we stacked an insulating layer on the brass substrate and formed the coil and the core in each layer. Finally the sensor is removed from the brass substrate and becomes it is completed. (Fig.3)

Experiments and Results

We proved the fabricate process of MI sensor where 5 Insulation layers (SU-8), sputtering, and Au plating had been used. As a result, it succeeded in making the sensing element of Ni-Fe and the coil of 3D structure surrounding it on the brass substrate (Fig.4). In the future, measuring the characteristics of the MI Sensor, aims to further improvements in sensor and its fabrication process.

References

[1] Berthold Rogge, Joachim Schulz : Magnetische LIGA-Mikroaktoren, F &M.104(1996)

[2] B.Rogge, J.Schulz, J.Mohr, A.Thommes and W.Menz : FULLY BATCH FABRICATED MAGNETIC MICROATORS USING A TWO LAYER LIGA PROCESS, TRANDUCERS’95

[3] K.Mohri、Y.Nakamura、T.Uchiyama、Y.Mohri、Yu.Mohri、 and Y.Inden : Sendeing of Human Micro-vibration Transmitted Along Solid Using Pico-Tesla Magneto-impedance Sensor (pT-MISensor), PIERS ONLINE, VOL.6, NO.2, 2010

[4] Tsuyosi Uchiyama, Shinsuke Nakayama, Kaneo Mohli, and Kenichi Bushida : Biomagnetic field detection using very high sensitivity magnetoimpedance sensors for medical applications Phys.Status Solidi A 206, No.4, 639-643(2009)/DOI 10.1002/pssa.200881251

[5] Berkem Özkaya, Srinivasa Rao Saranu, Senthilnathan Mohanan, and Ulrich Herr : Effects of uniaxial stress on the magnetic properties of thin films and GMR sensors prepared on polyimide substrates phys. stat sol (a) 205, No.8, 1876-1879(2008)/DOI 10.1002/pssa.200824036

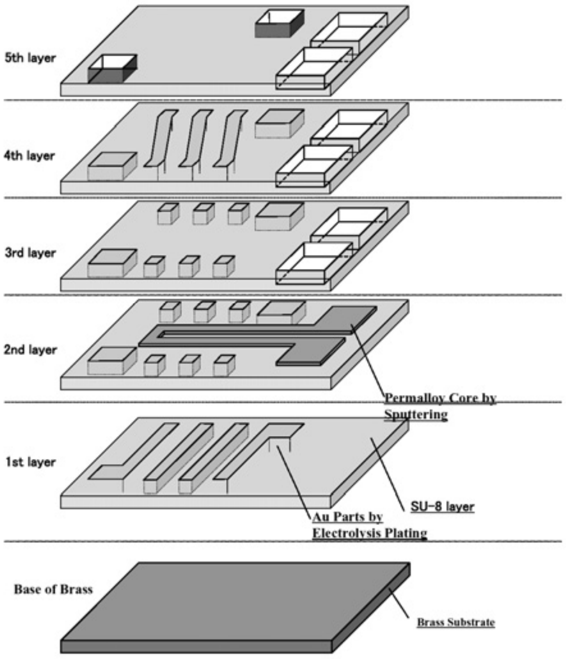

Fig.3 Outline of MI sensor fabrication process

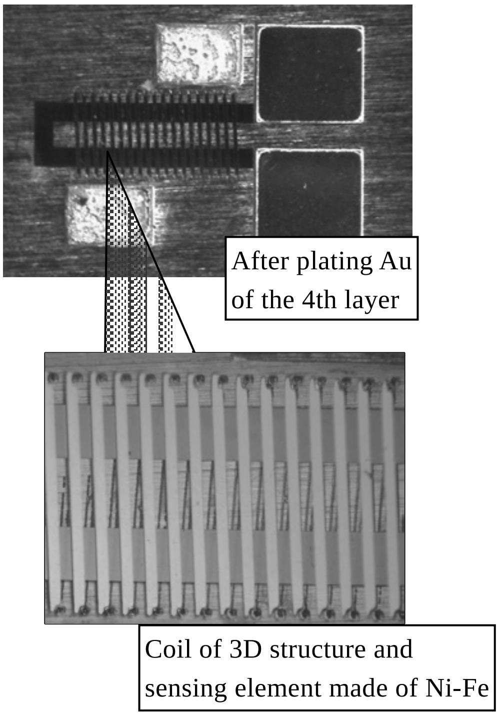

Fig.4 The structures of fabricated MI.sensor.

Fabrication of Gold Nanoparticles Assembled Nanovalley for Surface Enhanced Raman Scattering

Takao Fukuoka, Daisuke Fukuoka, and Yuichi Utsumi
Laboratory of Advanced Science and Technology for Industry, University of Hyogo, Japan

Abstract

We developed a novel structure "Nanovalley" using the anisotropic self assembles of gold nanoparticles on the nanoimprint template. The anisotropic noble metal nanostructures such as linearly connected gold nanoparticles have localized plasmon resonance (LPR) of longitudinal mode which appears in near infrared region depending the aspect ratio of the nanostructures. Enhance field of this LSR enables surface enhanced Raman scattering (SERS) with near infrared laser irradiation. Sufficiently, the demonstration of rapid, sensitive, non-label and near infrared sensing of molecules was carried out with the fabricated unique anisotropic nanostructures.

1. Introduction

The anisotropic noble metal nanostructures such as linearly connected gold nanoparticles have localized plasmon resonance (LPR) of longitudinal mode which appears in near infrared region depending the aspect ratio of the nanostructures.1) Evoked enhance field of this LSR enables surface enhanced Raman scattering (SERS) with near infrared laser irradiation. SERS is interesting phenomenon that Raman scattering intensity of the adsorbed molecules onto noble metal nanostructure with nano scale roughness are largely sensitized.2) Recently, SERS has brought much attention as new method which is optimum for narrow channel like microfluidic device.3,4)

There are, however, two problems to use SERS in the microfluidic device. The first problem is to fabricate appropriate nanostructure with suitable localized plasmon resonance wavelength for SERS in the narrow and limited region of micron order channel. Second, it is required to detect SERS signal rapidly to make use of characteristic of microfluidic flow analysis.

To resolve these issues, we developed new nanostructure "nanovalley". In this nanovalley structure, gold nanoparticles of 40 nm diameter were assembled along grooves of 200 nm deep which were fabricated on Polydimethylsiloxane (PDMS) by the nanoimprint method.

2. Experiments and Results

Commercial gold nanoparticles dispersion was supplied from Archilys (Kyoto, Japan) since it was specially designed to form chain-like aggregation under the diffusion-limited aggregation, so that the localized plasmon resonance (LPR) of the assembled gold nanoparticles in the nanovalley was expected in the near infrared region.

The nanovalley structure were fabricated as shown in Fig. 1 ; spin coating of PDSM resin on the nanoimprint template (step 1), stick the PDMS on the silver layer coated on silicon plate (step 2), deposition of colloidal gold nanoparticles onto the PDMS (step 3), and drying to make assembles of gold nanoparticles on the nanovalleys (step 4).5)

Step 1
Spin coating with PDMS resin on the nanoimprint template

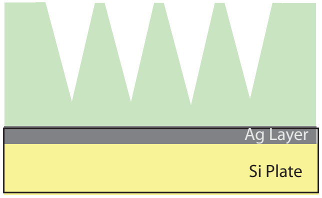

Step 2
Stick the PDMS on Ag Layer/Si Plate

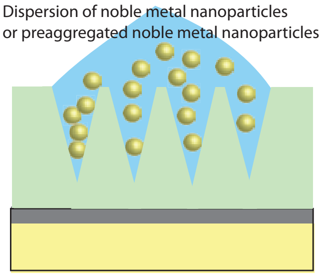

Step 3
Deposition of noble metal nanoparticles

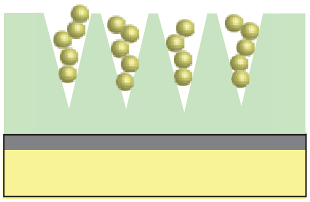

Step 4
The Nanovalleys with near infrared plasmon resonance

Fig. 1. Fabrication of the gold nanoparticles assembled nanovalley structure.

The obtained nanovalley structure kept color tone of reddish brown caused from LPR of assembled gold nanoparticles (Fig. 2). This reddish brown color seemed to be corresponding to the LPR in near infrared region.[1)]

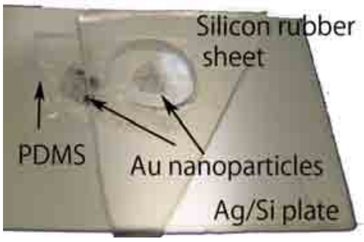

Fig. 2. Appearance of the nanovalleys substrate with LPR in near infrared region.

3. SERS Activity of The Nanovalley

Evaluation of SERS activity of the nanovally was carried out with Raman spectroscopy. This Raman spectrometer equips incidental light with 785 nm, 100mW laser. As Raman probe molecule, 4,4'-Bipyridine (4bpy) was used in aqueous solution.

In conventional SERS methods, it is essential that the sample solution is dropped and subsequently evaporated on the nanostructure, before Raman scattering of the deposited solid sample is collected. However, the throughput of the flow analysis is interrupted by the evaporation process in this "drop and dry" method.

To the contrary, the rapid signal response and long term stability of SERS spectra of 4bpy aqueous solution by 785 nm irradiation were observed. As shown in Fig. 3, 10 μM of 4bpy solution was sufficiently detected, while 100 mM concentration of 4bpy was required in normal Raman measurement without the nanovalley. These facts meant apparent enhancement more than 10^4 at least was achieved by using the anisotropic gold nanoparticles assembles.

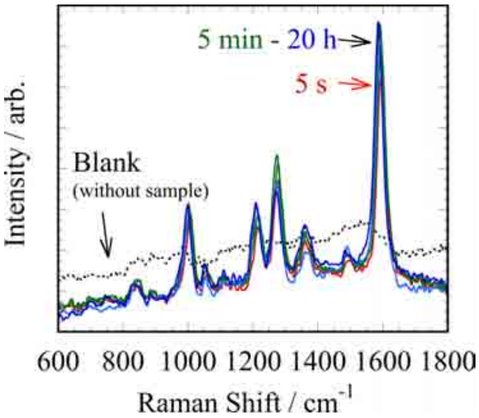

Fig. 3. Typical SERS spectra of 10 μM 4bpy aqueous solution with elapsed time after immersion in sample solution.

As for an in situ SERS measurement where the nanovalley structure was immersed in 4bpy aqueous solution, SERS appeared within 5 s after the immersion (Fig. 3 and 4). This very fast response of SERS signal was desirable for high throughput assay in microfluidic system. Fig. 4 also showed that the SERS intensity about 1600 cm^{-1} of 4bpy almost maintained constant value for 20 h.

The outstanding stability of SERS signal proves that the SERS active nanostructure in the nanovalley has been stable and unbreakable even under the wet condition.

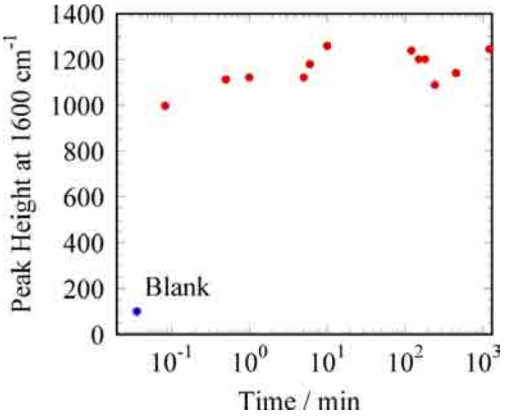

Fig. 4. SERS intensity response at 1600 cm^{-1} peak and long term stability using the nanovalley.

4. Concluding remarks and perspectives

In conclusion, the availability of the nanovalley structure as detector of microfluidic device was sufficiently demonstrated. It is thought that the unique nanovalley structure with anisotropic assembles of gold nanoparticles results in excellent effects for high throughput SERS measurements.

References

[1] M. Quiten and U. Kreibig: "Absorption und Elastic Scattering of Light by Particle Aggregates", Appl. Optics, 32(30), pp.6173-6182, 1993.

[2] R. K. Chang and T. E. Furtak (Ed.): “Surface Enhanced Raman Scattering”, Plenum, 1982.

[3] L. X. Chen and J. B. Choo : “Recent advances in surface-enhanced Raman scattering detection technology for microfluidic chips”, Electrophoresis, 29(9), 1815-1828(2008).

[4] S. D. Hudson and G. Chumanov : “Bioanalytical applications of SERS (surface-enhanced Raman spectroscopy)”, Anal. Bioanal. Chem., 394,.679-686 (2009).

[5] T. Fukuoka, D. Fukuoka, Y. Mori, Y. Utsumi, “Fabrication of Gold Nanoparticles Assembled Nanovalley for Surface Enhanced Raman Scattering”, IEEJ Transactions on Electronics, Information and Systems, 130(10), 1806-1810(2010).

Coherent Scatterometry Microscope (CSM)

Hiroo Kinoshita, Masato Nakasuji, Testuo Harada, and Takeo Watanabe

Center for Center for EUVL, LASTI, University of Hyogo

1. Introduction

This system is developed for the EUV mask inspection for the defect size of 20 nm and below, and also for mask absorber pattern CD measurement with high accuracy. To achieve these requirements, reconsidering the principle and law of the optics, it is employed that the novel inspection method instead of the conventional optics for the microscope. In this novel method, diffracted light intensity distribution observed by an irradiated coherent light to the mask absorber pattern is analyzed by a computer. Finally, using this novel method, it can realize that the high accurate measurement method which has never been achieved in the paradigm for the smaller rule for the advanced semiconductor devices. Since 2008, coherent scatterometry microscope has been developing n our lab with collaborating with RIKEN and Osaka University.

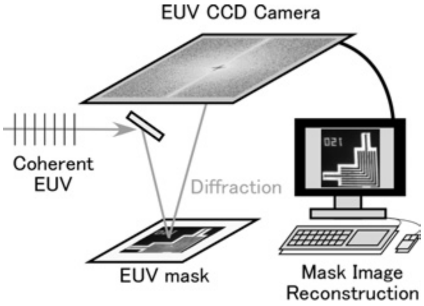

Fig. 1. The principle of the EUV coherent scattrometry microscope.

2. Coherent Scatterometry Microscope

Figure 1 shows the principle of the CSM. This system consists of the light source, mask, the CCD camera for the soft x-ray, and the computer. Defect can be inspected by the following method; 1) irradiating coherent light to the mask absorber pattern, 2) observing the diffracted light intensity distribution by the CCD camera, finally 3) absorber pattern images are reconstructed by a computer algorithm of the iterative Fourier-Transform method for the phase retrieval. In addition, absorber pattern width can be analyzed by the diffracted light intensity of the periodic absorber pattern, and it can be measured as a focal pattern width on the wafer.

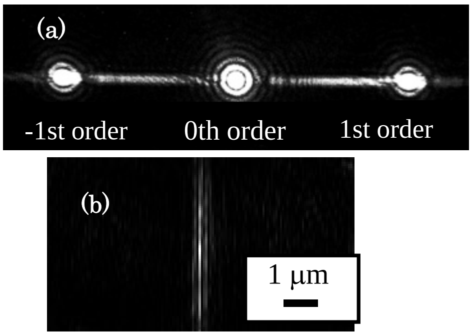

Fig. 2. Observation results of the line-defect of 30-nm width pattern in 22 nm node; (a) diffracted light intensity distributions, (b) reconstructed image

3. Observation Results of the EUV Masks

In the EUV mask for 22 nm node, Figure 2(a) shows the diffracted light intensity image and reconstructed image of L/S pattern with a 30-nm-width line-defect by the CCD camera distribution. The diffracted light signals from the line-defect are observed between the 0th-order light from the ±1th-order lights from the periodic mask pattern. As shown in Fig. 2(b), only line-defect image is reconstructed by remove the periodic pattern image applying specific frequency filtering. In addition, the excellent repeatability 0.32 nm (3) for the CD measurement of the line and space pattern is obtained, and the requirement of less than 0.65 nm (3) in the ITRS is achieved.

4. Mask Metrology System utilizing High-Order Harmonic EUV Light Source

Collaborating with RIKEN and Osaka University, a high-order harmonic laser for EUV light source on the basis of the 59th harmonic (= 13. 5nm) of the femto-second laser has been developing. Using this source, since reducing a CSM inspection time by increasing the light source intensity to be 1000 times larger than the conventional light source, full field mask inspection can be achieved.

5. Conclusions

Mask CD maeasurement becomes close to the practical technology level. For the mask defect inspection, the diffraction light intensity images of the various types of the mask defects have been analysing. In the future, 3-D recontructed images of the mask could be achieved to obtain.

EUV Finished Mask Observation utilizing EUV Microscope

Hiroo Kinoshita, Akifumi Tokimasa, Testuo Harada, and Takeo Watanabe

Center for Center for EUVL, LASTI, University of Hyogo

1. Introduction

Mask defect reduction is one of the significant issues. Since 2002, bright field mask metrology system for the finished EUV mask had been developed, and using this system hp 100 nm absorber pattern, pit-type phase defect size of 20 nm and the depth of 2 nm on the blank mask were succeed to obsorbed

.

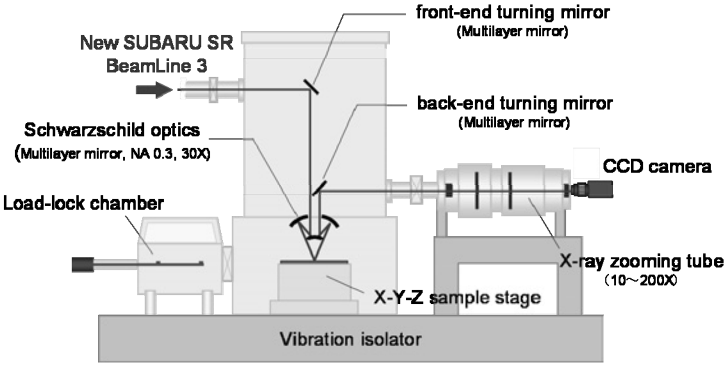

Fig. 1 System configuration of EUVM

2. Configuration of the Experimetal Tool

Figure 1 shows the system configuration of the EUVM. The light source is the bending magnet of BL3 beamline of NewSUBARU synchrotron radiation facility. Schwarzschild optics (NA 0.3 and 30X) and the x-ray zooming tude (20X～100X) are employed for the imaging optics. The optical image of the mask pattern was focused by the Schwarzschild optics on the CsI photocathode, this image was transfer to the electron image by the CsI photocathode, and demagnified by the eletromagnetic lense of the X-ray zooming tube. And then the eletron image was transfer to the optical image by the fluorescent plate after a micro-channel plate (MCP) and finally the image is capture by the CCD camera. As the spatial resolution of CsI is 0.3 m, 20 nm size defect can be theoretically obserbed. The 172-nm-wavelength Xe lamp is attached on the loadlock chamber to remove contamination on a sample before the observation. Figure 2 show the photograph of the EUVM.

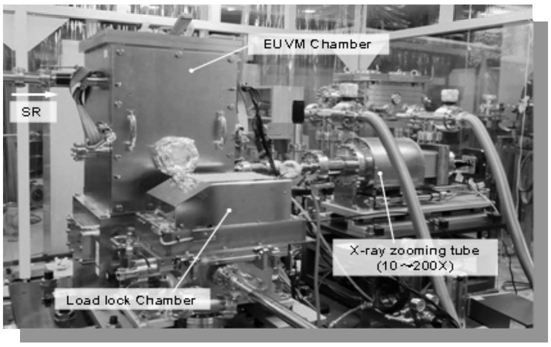

Fig. 2 Photograph of EUVM

3. Obervation Results

Obervation results are shown in Fig. 3.

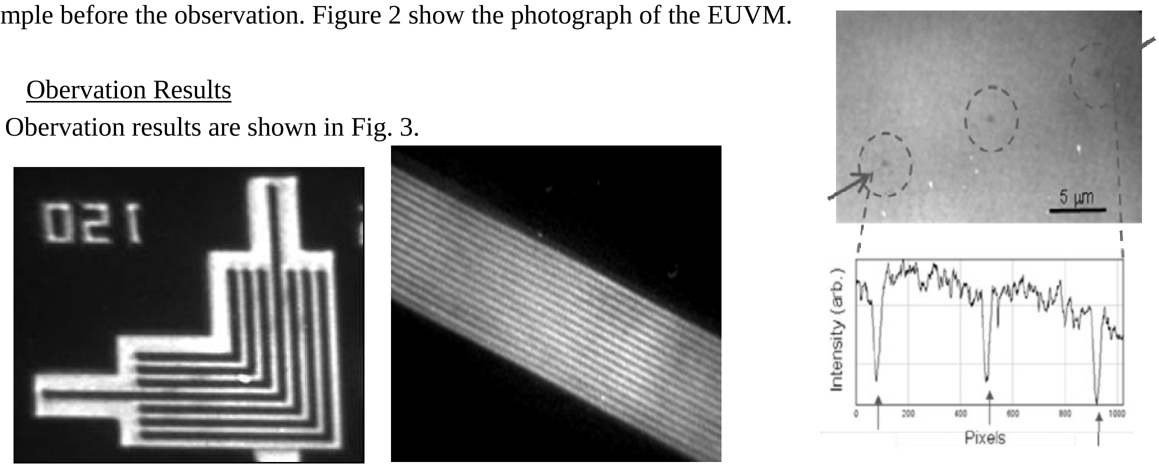

(a) hp480 nm Elbow (b) hp100 nm L&S (c) Phase defect on the mask blank

Fig.3. Observation results; (a), (b)absorber pattern, and (c) phase defect

4. Conclusions

Absorber pattern of the finished EUV mask and phase defects of mask blank can be observed by the EUVM.

EUV Interference Lithography

Takeo Watanabe, Yuya Yamaguchi, Takuro Urayama, Masato Nakasuji, Akifumi Tokimasa,

Naohiro Matsuda, Testuo Harada, Hiroo Kinoshita, and Takeo Watanabe

Center for EUVL, LASTI, University of Hyogo

1. Introduction

EUV interference lithographic system which can evaluate the resists for hp 22 nm, hp 16 nm, and hp 11 nm nodes has been developing. Since in EUV interference lithography using light diffraction and interference, replicated resist pattern with high accurate and high resolution can be obtained, it can be evaluated that resolution and LWR of resist itself without other fac JV-IL exposure system is installed at the BL-9 beamline. Since the 10.8-long undulator (LU) is employed as a light source, spatial coherence is large and fine pattern can be replicated in the whole exposure area. Up to now, 60-nm-pitch transmission grating pattern is fabricated, which corresponds to hp 15 nm resist pattern on a wafer.

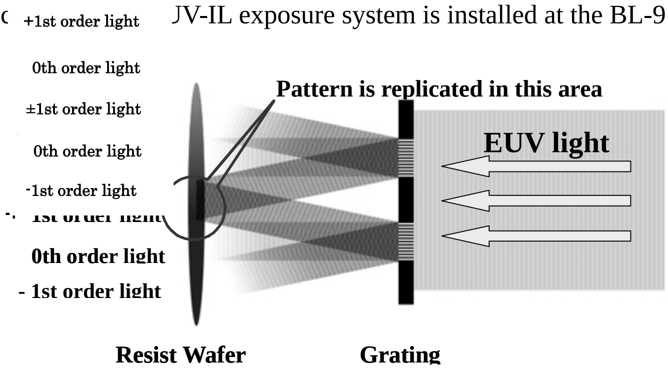

Fig. 1. Principle of EUV-IL.

2. Principle of EUV-IL

The intensity of the light produced from the LU is 1,000 times higher than that from the bending magnet. In addition, the high coherent light is produced from the LU. By Young's interference experiment, it is confirmed that spatial coherence length larger than 1 mm. Figure 1 shows the configuration of the principle of EUV-IL using two window type transmission grating. When the EUV light irradiates to the one grating window, the light diffracted into 0^{th}, -1^{st}, and $+1^{st}$ orders light. By two window grating, -1^{st} order light from one window grating and $+1^{st}$ order light from another window grating are interfere to produce the interference fringes on a wafer position. Consequently resist pattern with a half pitch size of the transparent grating is replicated on a wafer. The transmission grating is fabricated in the EUVL R&D center.

3. Exposure Results

Figure 2 shows the replicated resist pattern of the commercial resist ZEP-520A for electron utilizing EUV-IL. SEM photographs of hp 22.5 nm, hp 20 nm, and hp 15 nm resist patterns were shown in this figure. We obtain resist patterns with high contrast.

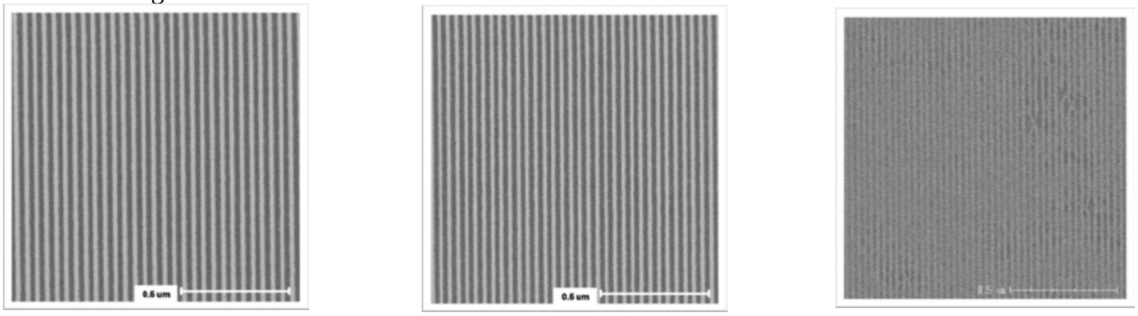

(a) hp 22.5 nm (b) hp 20 nm (c) hp 15 nm

Fig. 2. Exposure results obtained by EUV-IL

4. Conclusions

EUV-IL system has large enough coherence length. Uniform and high contrast resist patterns are replicated in whole exposed area. And it is confirmed that EUV-IL is effective for the resist evaluation of hp 22 nm and below.

In-situ contamination thickness measurement in the EUV resist outgassing environment

Takeo Watanabe, Naohiro Matsuda, Tetsuo Harada, and Hiroo Kinoshita

Center for EUVL, LASTI, University of Hyogo

1. Introduction

Exposure in EUVL requires vacuum environment. Since, in EUVL during the exposure, the carbon contamination is adhered on the optics and the mask, Mo/Si multilayer (ML) reflectivity of the optics and the mask, and replicated pattern width on a wafer could be changed. The carbon contamination mainly own to the decomposition reaction of the hydrocarbon gas species by EUV irradiation. Although many researches were carried out to reduce the contamination, it has not been clarified yet that the relationship between the outgas species of the hydrocarbons and the carbon contamination adhesion thickness on ML. Thus, the in-situ thickness-measuring system for the carbon contamination due to the resist outgas during the EUV irradiation.

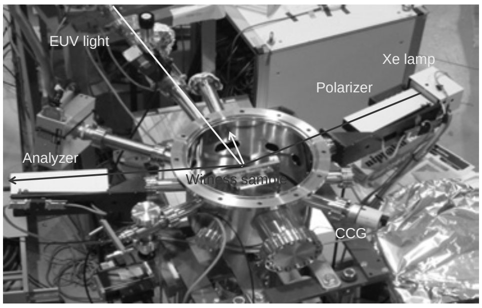

Fig. 1. Photograph of the novel resist evaluation system.

2. Experimental

Figure 1 shows the photograph of this system. EUV light irradiates to a witness sample of a Mo/Si ML mirror at the normal incident angle of 6 degrees, and the EUV light irradiates to the resist sample. The vacuum pressure is measured by the pressure gauge, and the outgas species are measured by the quadruple mass spectrometer (Qmass). Simultaneously, the contamination adhesion thickness is measured by the in-situ ellipsometer. Xe lamp is employed as a light source of the ellipsometer. The Xe light is led to the witness sample through the polarizer and then the reflected light is led to monochrometer through the analyzer. Finally the polarization spectra of the wavelength from 250 nm to 800 nm was analyzed to measure the adhesion thickness of the carbon contamination.

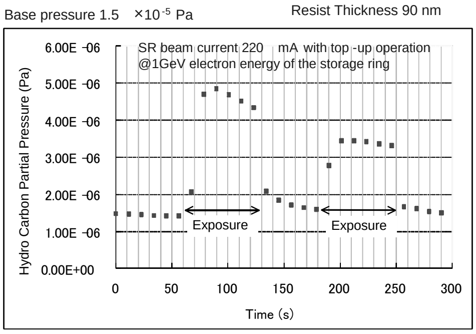

Fig. 2. Hydrocarbon partial pressure measured by Qmass.

3. Results and Discussions

Figure 2 shows the hydrocarbon partial pressure time dependency of the hydrocarbon. Since the partial pressure becomes high during the EUV irradiation and the partial pressure becomes small during the non-exposure, hydrocarbon outgas species produced during the EUV irradiation exposure to the resist. Figure 3 shows the time dependency of the carbon contamination thickness measured by the in-situ ellipsometer. In the thickness measurement, multilayer structure of the witness sample was taken in an account. The thickness measurement result by the in-situ ellipsometer has a good agreement with that by the atomic force microscope (AFM), by the nanometrcis thickness measurement system, and the reflectometer at the BL10 beamline in NewSUBARU. As the results, it is confirmed that the effectiveness of the carbon contamination thickness utilizing the in-situ ellipsometer.

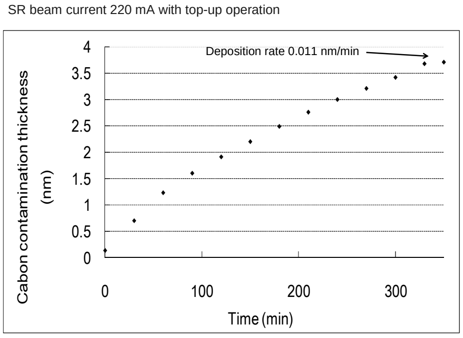

Fig.3 EUV irradiation time dependency of carbon contamination deposition

4. Conclusions

It is confirmed that the effectiveness of the carbon contamination thickness utilizing the in-situ ellipsometer. In addition, it is confirmed that the relationship between the resist outgas species by EUV irradiation and the adhesion thickness of the carbon contamination under the EUV light intensity required for the HVM.

Optical element evaluation system

Tetsuo Harada, Takeo Watanabe, and Hiroo Kinosh8ita

Center for EUVL, LASTI, University of Hyogo

1. Introduction

Multilayer reflectivity measurement plays an significant role of the lithographic throughput in the EUVL technology. At NewSUBARU, since 2000, the reflectometer beamline for the multilayer reflectivity measurement had been constructed, and this beamline has been opened for common use for two companies of the mask blanks.

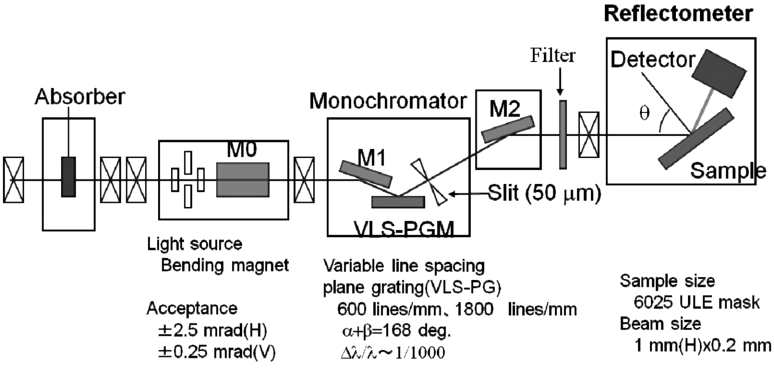

Fig. 1. Configuration of the reflectometer at BL-10 beamline

2. System Configuration

Figure 1 shows the configuration of BL-10 beamline. Monk-Gillieson type monochrometer, on the basis of the variable-line-spacing plane-grating-monochrometer (VLS-PGM) is employed as a monochrometer. Influence of the higher order light is reduced by a Si filter.

By adjusting the inclination angle of the monochrometer , the incident light can be monochromated to the wavelength from 6.0 nm to 24 nm using the VLS-PGM with the line density of 600 lines/mm. In addition, in the case of the VLS-PGM with the line density of 1800 lines/mm line, it can be monochromated to the wavelength from 3.0 nm to 8 nm and the K absorption edge of the oxygen can be analyzed. The reflectometer consists of the -2 stage, and x-y stage is attached on the -stage which can cover the whole mask area size of 150×150 mm^2 for the reflectivity measurement. Since the - and 2 - stages can be moved by the individual stepping motors through ferrofluidic seal from outside the vacuum chamber, high speed and high accurate movement of 1 to 89 degrees for the mask incident angle can be controlled.

3. Example of the Reflectivity Measurement

Figure 2 shows the reflectivity spectra of same Mo/Si ML sample at NewSUABRU and Advanced Light Source (ALS). From this figure, it can be confirmed that the reflectivity spectrum measured at BL10 beamline at NewSUBARU is almost same as that measured at ALS. In addition, comparison results of the centroid wavelength and the reflectivity for that are shown in Table 1. As results, the reflectivity measurement accuracy becomes to be a world standard.

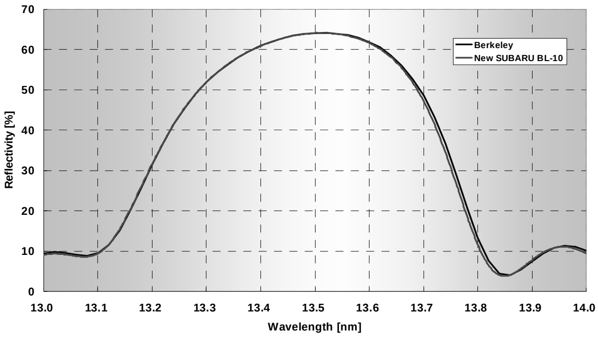

Fig. 2. Reflectivity spectra measured at NewSUBARU

Table 1. Measurement accuracy comparison with NewSUBARU and ALS

	CWHM （Measurement accuracy of the centroid wavelength）	Measurement accuracy of the reflectivity
ALS	0.007 nm	0.08%
NewSUBARU	0.0064 nm	0.11%

Classification of Near-Edge X-ray Absorption Fine Structure Spectra of Si-containing DLC Thin Films

Kazuhiro Kanda[a,*], Masahito Niibe[a], Akira Wada[b], Haruhiko Ito[b], Tsuneo Suzuki[c], and Hidetoshi Saitoh[b]
[a]*LASTI, University of Hyogo, 3-1-2 Koto, Kamigori, Ako, Hyogo 678-1205, Japan*
[b]*Department of Materials Science and Technology, Nagaoka University of Technology,*
1603-1 Kamitomioka Nagaoka, 940-2188, Japan
[c] *Extreme Energy-Density Research Institute, Nagaoka University of Technology,*
1603-1 Kamitomioka Nagaoka, 940-2188, Japan

Abstract

Structural analysis was performed on the 23 kinds of silicon-containing diamond-like carbon (Si-DLC) films fabricated with various synthesis methods by the measurement of carbon K-edge near-edge x-ray absorption fine structure (NEXAFS) using synchrotron radiation. Observed NEXAFS spectra of Si-DLC films were classified to 4 kinds of type. The shrinking and shift of σ* band and broadening of π* peak were founded. The change of C K-edge NEXAFS spectrum of Si-DLC film was strongly related to the content of Si in the Si-DLC film.

1. Introduction

One of the important issues for the use of DLC films as wear-resistive coatings is their internal stress. The containing of hetero-atom in DLC films posses the potential to improve wear performance. However, comprehensive analysis of C K-edge NEXAFS spectra has not investigated as for many Si-DLC films fabricated with various synthesis methods. In the present study, local structures of 23 kinds of Si-DLC films were studied using C K-edge NEXAFS spectroscopy . The elementary analysis was performed from the combination of Rutherford backscattering spectrometry (RBS) and elastic recoil detection analysis (ERDA).

2. Experimental

The NEXAFS measurement was performed at the BL05B and BL09A of NewSUBARU in the University of Hyogo. Synchrotron radiation dispersed by a invalid spacing planer grating monochromator was irradiated on the sample film at 54.7° (magic angle) with respect to surface normal of samples. The electrons coming from the sample were detected in the total electron yield (TEY) mode. The RBS and ERDA with MeV-He^+ irradiation were performed using an electrostatic accelerator (NT-1700HS: Nisshin-High Voltage Co.) located at the Extreme Energy Density Research Institute, in Nagaoka University of Technology. The He^+ ions accelerated to 2.5 MeV were used as incident beam at 72° with respect to surface normal of samples.

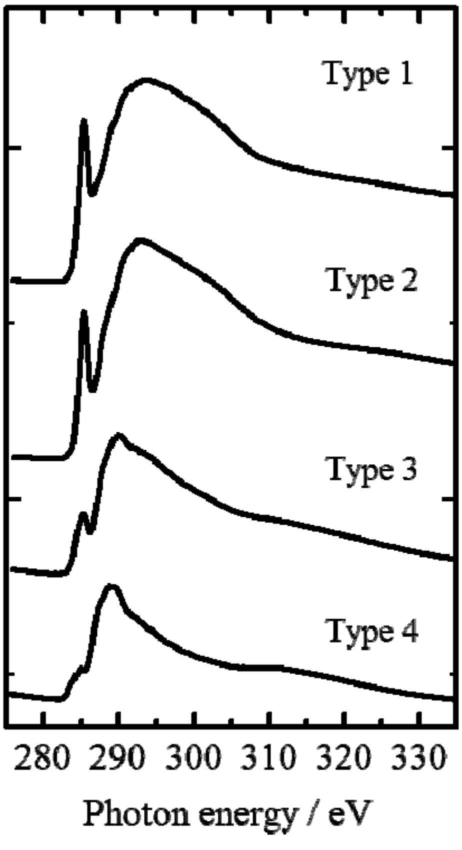

Fig. 1 The C *K*-edge NEXAFS spectra of Si-DLC films

3. Results and Discussion

The NEXAFS spectra of Si-DLC films can be classified to 4 types by its spectral profile as shown Fig. 1. Figure 2 depicts NEXAFS spectra of a typical DLC film, which contains only carbon and hydrogen without Si and other hetro-elements, and β-SiC powder as references. A sharp peak was observed at 285.4 eV in the NEXAFS spectrum of typical DLC film. This peak is originated from the transition from 1s orbital to unoccupied π orbital. In other words, this peak indicates the sp^2 hybridized orbital, therefore this peak is not observed in the NEXAFS spectrum of diamond. The broad band at around 293 eV is generated from the transition from 1s orbital to unoccupied σ orbital. In this region of NEXAFS spectra of diamond and graphite, structural peaks were observed, but in the spectra of DLC film, only broad band was observed due to its amorphous structure. In the NEXAFS spectrum of β-SiC powder, a sharp peak was observed at 289 eV. This peak was assignable to the 1s→σ* transition generated from the carbon bonded to silicon.

In the type 1 of NEXAFS spectra of Si-DLC films, spectral profile resembled that of typical DLC film without hetro-atoms. In the type 2 of NEXAFS spectra of Si-DLC films, the shrinking of the band generated from the 1s→σ* transition was found. In the type 3 of NEXAFS spectra of Si-DLC films, the shrinking of 1s→σ* band advanced and this band was shifted to lower energy side. In addition, the peak generated from the 1s→π* transition was found to broaden. In the type 4 of NEXAFS spectra of Si-DLC films, the 1s→π* peak cannot be observed as isolated peak by the advancement of the shrinking and shift of σ* band.

Figure 3 depicts the relation of type of NEXAFS spectrum of Si-DLC film with elementary composition determined by the measurement of the combination of RBS and ERDA techniques. The type of NEXAFS spectrum increased from 1 to 4 with increasing Si content in Si-DLC film. The boundary between type 1 and type 2 was located at ≈6 % of Si content. Type 3 was appeared in the region where Si content was larger than 10 % and type 4 was appeared beyond 25 % of Si content. In other words, the type of NEXAFS spectrum increased from 1 to 4 with increasing Si content in Si-DLC film. In addition, the type of NEXAFS spectrum also increased with H content. This indicated that the type of NEXAFS spectrum is determined by the Si/(Si+C) rather than Si/(Si+C+H). From these observations, the shrinking and shift of σ* band was interpreted that the 1s→σ* transition of C-C site was altered to that of C-Si site with the increase of Si content in the film. In the type 3 of NEXAFS spectra of Si-DLC films, the broadening of 1s→π* peak was observed as described above. The peak width of 1s→π* transition was plotted against Si-content in Fig. 4. The peak width of 1s→π* transition slightly increased with Si-content. It can be considered that the peak width of 1s→π* peak was broadened by the appearance of C=C-Si site with Si-content in the Si-DLC film.

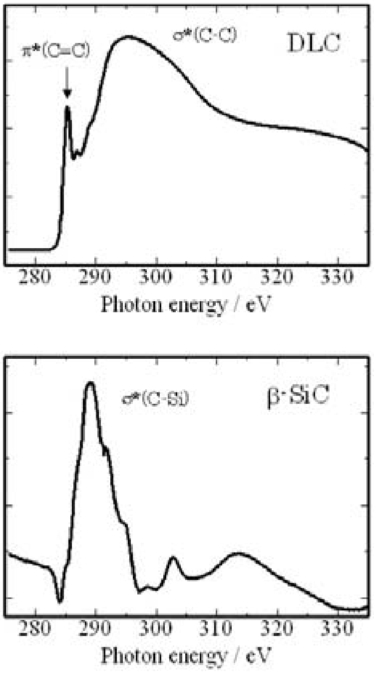

Fig. 2 The C *K*-edge NEXAFS spectra of a) a typical DLC film and b) β-SiC powder

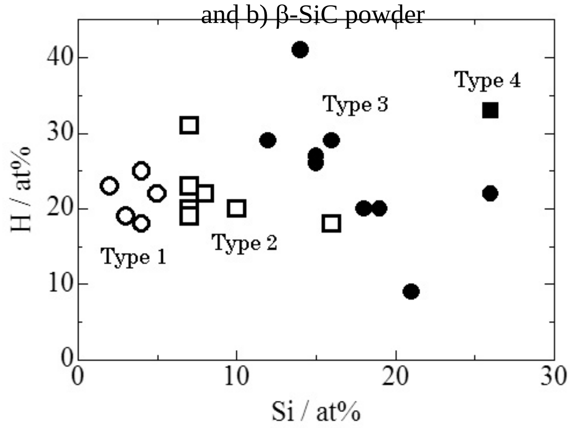

Fig. 3 The relation of type of NEXAFS spectrum of Si-DLC film with elementary composition; open circle: type 1, open square: type 2, closed circle: type 3,.and closed square: type 4.

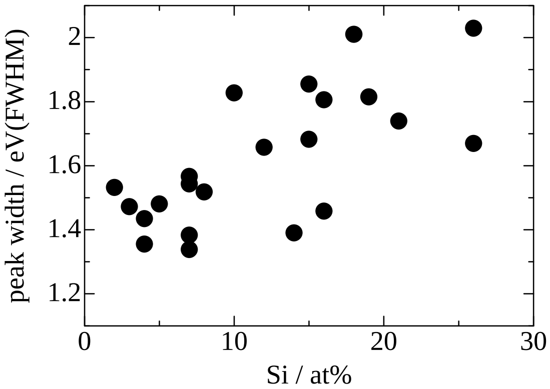

Fig. 4 The dependence of the peak width of 1s→π* transition against Si-content in the Si-DLC film.

4. Conclusions

The C K-edge NEXAFS spectra of 23 kinds of Si-DLC film fabricated by various synthesis methods were using synchrotron radiation. C K-edge NEXAFS spectra of Si-DLC films were classified to 4 kinds of type. Shrinking of σ* band was due to the change from σ(C–C) to σ(C–Si). Broadening of π peak can be considered to increase of C=C–Si site. The type of C K-edge NEXAFS spectrum of Si-DLC film was strongly related to the content of Si. Classification of Si-DLC NEXAFS spectrum can be considered to good index for the classification of Si-DLC films.

Sulfur $L_{3,2}$-edge XANES spectroscopy reveals differences in sulfur speciation of reference S compounds

Toko Tanikawa[1)], Kazuhiro Kanda[2)], Masaharu Uemura[3)], Takayuki Hasegawa[3)],
Mizue Ohashi[4)], Yashuhiro Hirano[5)]

1) Kansai Research Center, Forestry and Forest Products Research Institute, Nagai-kyutaro, Momoyama, Fushimi, Kyoto; 2) Laboratory of Advanced Science and Technology for Industry, University of Hyogo, 3-1-2 Koto, Kamigori-cho, Ako-gun, Hyogo; 3) Synchrotron Analysis L.L.C., 3-1-2 Koto, Kamigori-cho, Ako-gun, Hyogo; 4) School of Human Science and Environment, University of Hyogo, 1-1-12 Shinzaike-Honcho, Himeji, Hyogo; 5) Graduate School of Environmental Studies, Nagoya University, Furo-cho, Chikusa, Nagoya, Aichi

Abstract

In forest soils, sulfur exists in a large variety of organic and inorganic forms with different electronic oxidation states, ranging from -2 to +6. Because an excess S from atmospheric depositions is supposed to disturb soil ecosystems, and the disturbance would be repressed by a soil sulfur retention function, it is needed to clear sulfur retention mechanism. An advanced technique, X-ray absorption near-edge structure (XANES) has recently been adapted for S fractionations in environmental samples. Previous studies reported that the technique was superior to traditional wet-chemical methods for the S fractionations. Thus, we examined whether S L-edge XANES is able to fractionate 6 analysis-grade reference S compounds by different oxidation states or not. The differences in compound structures were reflected clearly in the spectra at BL05B. These results suggest that a beamline BL05B can be used reliably to separate and quantify sulfur species with different oxidation states.

Introduction

Sulfur, an essential element for the growth of plants and microorganisms, continuously cycles between organic and inorganic forms in the soil. An excess S from atmospheric depositions is supposed to disturb soil ecosystems. The soil retention of organic S is a key process regulating a S cycling in terrestrial ecosystems, and the process can diminish or delay the net acidification of soils. In general, the soil organic S is classified into hydroiodic acid-reducible and -nonreducible S, both of which are considered to represent an ester sulfate-S and a carbon (C)-bonded S, respectively. The former is corresponded to the soil organic S in highly oxidized states, and the latter is corresponded to highly reduced and intermediate oxidation states. These traits were determined by a recent advanced technique, S K-edge XANES spectroscopy. The traditional classification of organic S based on bond classes might not have an enough sensitivity to distinguish between labile and refractory organic S forms. Detail fractionations of the organic S using the advanced techniques are needed to clarify the mechanism of organic S retentions in forest soils. Although the K-edge XANES is not be able to detect the difference between organic and inorganic S, a L-edge analysis is expect to be suitable for S fractionations. However, the application of soil sulfur fractionation using L-edge XANES analysis has not been reported yet. To establish a S fractionation method, we examined whether the S L-edge XANES is available to fractionate 6 analysis-grade reference S compounds by different oxidation states or not.

Experiments and Results

Analysis-grade reference S compounds; L-methione DL-methionine sulfoxide, sodium sulfite, ethyl phenyl sulfone, L-cysteric acid, and sodium dodecyl sulfate were used for the XANES analysis at either beamlines of BL05B in the NewSUBARU synchrotron radiation facility, University of Hyogo. The spectra obtained by a total electron yield method at BL05B clearly reflected compound structures in the references, suggesting that BL05B was suitable for S fractionations. Because the differences in the compound structures were reflected clearly in the spectra at BL05B, this beamline can be used reliably to separate and quantify sulfur species with different oxidation states.

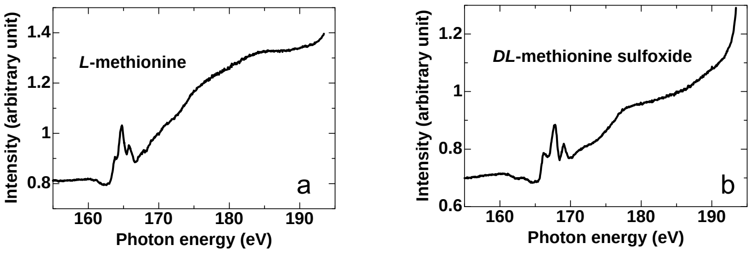

Grating=100 l/mm
Slit width=50 μm, Insident angle=90°

Grating=100 l/mm
Slit width=50 μm, Insident angle=90°

Fig.1 Sulfur $L_{3,2}$-edge XANES spectra obtained by total electron yield method at beamline BL05B.
a) L-methione; b) DL-methionine sulfoxide

The Present Status of Material Analysis Beamline at BL05 for Industrial Enterprises

T. Hasegawa[1], M. Uemura[1], M. Motoyama[2] and K. Kanda[2]
1 Synchrotron Analysis L.L.C., Hyogo-ku, Kobe, Hyogo 652-0863 Japan
2 University of Hyogo, Kamigori, Ako, Hyogo 678-1205 Japan

Abstract

A material analysis beamline for the industrial enterprises’ use was completed at BL05 in March 2008. BL05 consists of two branch lines, one is a double crystal monochromator beamline (BL05A) for the use in the higher-energy region (1300-4000 eV) and the other is a varied line spacing plane grating (VLSPG) monochromator beamline (BL05B) for the use in the lower-energy region (50-1300 eV). These two branch lines can be operated simultaneously. The whole useful energy range of the BL05 is the soft X-ray region from 50 to 4000 eV. The X-ray absorption fine structure (XAFS) measurements in the total electron yield (TEY) and fluorescence yield (FLY) can be performed at BL05A and BL05B. In addition, the X-ray photoelectron spectra (XPS) can be measured at BL05B.

Introduction

A material analysis beamline for the industrial enterprises’ use was completed at BL05 in March 2008 [1]. The light source of BL05 is the bending magnet, which can provide the photon in the region up to 4000 eV. BL05 consists of two branch lines for the use in the higher-energy region (1300-4000 eV) and lower-energy region (50-1300 eV), respectively. The whole useful energy range of the BL05 is the soft X-ray region from 50 to 4000 eV and X-ray absorption spectrum can be measured with a high-energy resolution. Because the incident beam from the bending magnet is provided for two branch lines through the different windows of mask, these two branch lines can be operated simultaneously. BL05 will be managed and maintained by the Synchrotron Analysis L.L.C. (SALLC), which is composed of the industrial companies, in cooperation with the staffs of the Laboratory of Advanced Scienece and Technology for Industry in University of Hyogo. Industrial users can be assisted by staffs of SALLC in the measurement at BL05. In this paper, we will introduce BL05 and report recent activities, which succeeds in the improvement of the optical alignment of BL05B.

Specifications of BL05A

Toroidal mirrors are used as a pre-mirror (M0) and a focusing mirror (M1) of BL05A, for the purpose to introduce a high-photon flux to the end station (Fig.1). InSb (111) crystals and Si (111) crystals are prepared for a Golovchenko-type double crystal monochromator. The XAFS measurements in the total electron yield (TEY) and fluorescence yield (FLY) using SDD (SII, Vortex) can be performed. The SDD can operated without liquid nitrogen.The fluorescence XAFS spectra can be measured samples at the under an atmospheric pressure by the replacement of an end station to He using Be window. It can keep 8 samples of 25 mm corner in the chamber because of industrial use.

Specifications of BL05B

Fig.2 shows optical layout of BL05B. The light beam is focused on the entrance slit S1 horizontally by the cylindrical mirror M0 and vertically by the cylindrical mirror M1. The constant-deviation monochromator consisting of a demagnifying spherical mirror and VLSPG, which can provide to high resolution, simple wavelength scanning with fixed slits, was mounted on BL05B. The including angle of the monochromator is 175°. The grating holder of VLSPG can keep three gratings (100-, 300- and 800-lines/mm) and change the active grating without braking vacuum condition. Two measurement chambers are prepared at the end station of BL05B. The XAFS spectra in the total electron yield mode and fluorescence XAFS spectra using SSD (EDAX) can be measurement in the high vacuum chamber. In addition, the X-ray photoelectron spectra (XPS) using spherical electron analyzer (VG Scienta, R3000) can be measured in the ultra high vacuum chamber. These chambers can be replaced each other within 1 hour. It can keep 16 samples of 25 mm corner in the respective chamber.

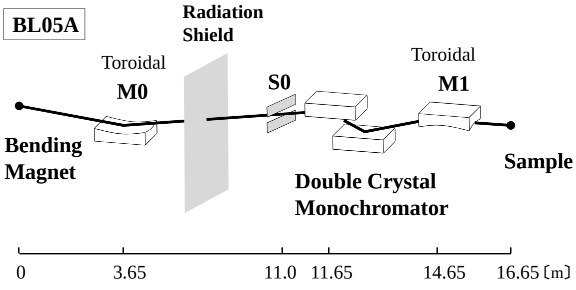

Fig.1 Optical layout of BL05A.

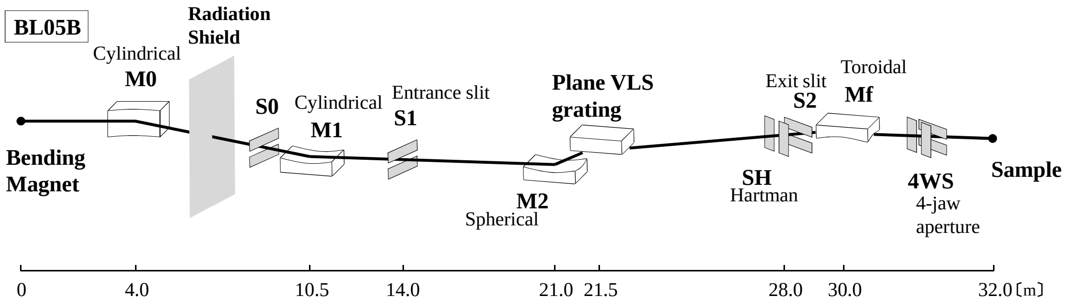

Fig.2 Optical layout of BL05B.

Measurement

We did readjustment of the optical mirror and measured standard samples by means of the TEY method in BL05B. Fig.3-5 show the absorption spectra which are obtained in each grating, 100- or 300- or 800-lines/mm, boron *K*-edge, calcium and nickel $L_{3,2}$-edge near-edge X-ray absorption fine structure (NEXAFS) spectra of hexagonal boron nitride (*h*-BN), calcium fluoride (CaF_2) powder and Nickel (Ni) sheet. The spectrum have been normalized to I_0 and had a linear pre-edge background removed. After the optical adjusting (slit width : 50 μm), improvement of resolution is verified by comparison with before the optical adjusting (slit width : 200 μm). For *h*-BN, an intense peak at 192 eV and a structured absorption band of 197-201 eV are assigned to the transitions from B1s to the unoccupied B2p π^* and σ^* states, respectively in Fig.3 [2]. Additionally, the calcium $L_{3,2}$-edge spectral shape of CaF_2 almost corresponds to the spectrum reported by Naftel et al. [3]. The nickel $L_{3,2}$ absorption peaks are observed at 853 and 871 eV, respectively [4].

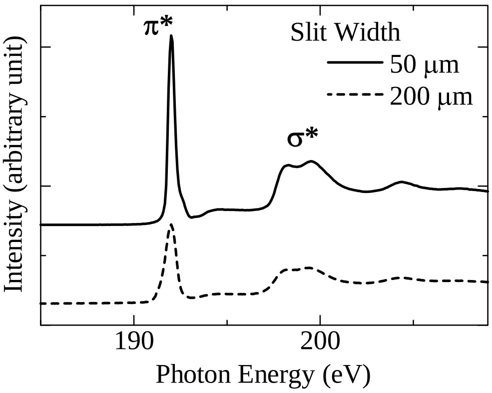

Grating=100 lines/mm, Incident Angle=45 °

Fig.3 *h*-BN B *K*-edge NEXAFS spectra.

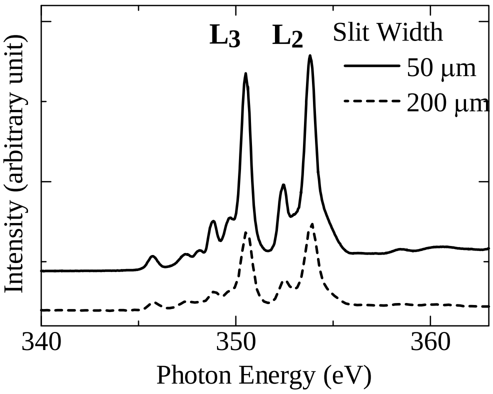

Grating=300 lines/mm, Incident Angle=45 °

Fig.4 CaF_2 Ca $L_{3,2}$-edge NEXAFS spectra.

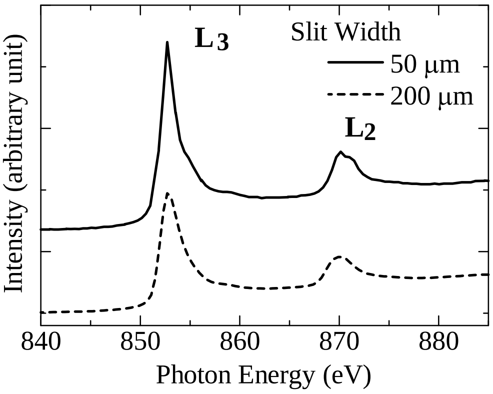

Grating=800 lines/mm, Incident Angle=45 °

Fig.5 Ni $L_{3,2}$-edge NEXAFS spectra.

References

[1] T.Hasegawa *et al.*, *Advances in X-ray Chem. Anal. Jpn.*, **41**, pp.99-106 (2010) [in Japanese].
[2] I.Jiménez, A.F.Jankowski, L.J.Terminello, D.G.J. Sutherland, J.A.Carlisle, G.L.Doll, W.M.Tong, D.K. Shuh, F.J.Himpsel, *Phys. Rev.*, **B55**, 12027 (1997).
[3] S.J.Naftel, T.K.Sham, Y.M.Yiu, B.W.Yates, *J. Synchrotron Rad.*, **8**, 255 (2001).
[4] J.A.Bearden, A.F.Burr, *Rev. Mod. Phys.*, **39,** 125 (1967).

Low-Temperature Crystallization of a-Si, a-Ge and a-SiGe Films by Soft X-ray Irradiation

Akira Heya, Yuki Nonomura, Shota Kino, Kazuhiro Kanda and Naoto Matsuo
University of Hyogo

Abstract

We investigated novel low-temperature crystallization of a-Ge, a-Si and a-SiGe films by the SR soft X-ray irradiation at storage ring current of 25-220 mA and dose quantity of 50 mA・h. The relationship between electron excitation followed by atom migration process, thermal process and the storage-ring current are investigated. Crystallization of SiGe caused by the vibration due to soft X-ray irradiation is effective as compared with the thermal annealing.

Introduction

Flexible organic light emitting diode (OLED) display is one of the most expected displays for next generation because of its light weight and flexibility. Polycrystalline Si, Ge and SiGe films on the polymer substrate are attractive for thin film transistor (TFT) in flexible flat panel display and solar cell. The process temperature to produce the poly-Si, Ge and SiGe films by excimer laser annealing is too high to apply the plastic substrate. We have proposed a novel low temperature crystallization method of soft X-ray irradiation using short undulator BL07A of NewSUBARU of SR facilities. In this study, we investigate the crystallization mechanism of a-Si, a-Ge and a-SiGe irradiated using soft X-ray undulator source.

Experiments and Results

a-Si films was deposited on SiO_2/glass substrate by PECVD and a-Ge and a-SiGe were deposited by MBD (deposition rate: 0.02 nm/s, base pressure: ~10^{-10} Torr). The thickness of a-Ge, a-Si and a-SiGe was 50 nm. The storage ring energy, storage ring current, photon energy and dose quantity were 1.0 GeV, 25 to 220 mA, 115 eV and 50 mA・h (Irradiation times was 30min in case of 100mA), respectively. The characteristics of the film were measured by Raman spectroscopy. Raman spectroscopy condition that laser power and object lens were 1.5 mW and 100 times. In the case of Si films, the crystalline fraction was determined from the areal ratio of the signal due to the crystalline phase around 521 cm^{-1} to the sum of the signals due to both the crystalline phase and the amorphous phase around 480 cm^{-1}.

Figure 1 shows crystalline fraction of Si, Ge SiGe films as a function of storage-ring current. The crystallization threshold of Ge sample was 75 mA. Sample temperature and crystalline fraction were 420°C and 80%, respectively. On the other hand, Si sample did not crystallize at 75 mA, although the sample temperature rised up to 390°C. Crystalline fraction at the center of Ge and Si were 80 % and 0 %, respectively. The difference of crystalline fraction between a-Si and a-Ge is thought to be due to the energy band gap (Eg) of Ge and Si. The electron excitation of Ge was 10^7 times larger than Si. The density of state in the valence band of Si and Ge was almost the same. Therefore, it is thought that electron in valence band of Ge is excited easily, the sample temperature becomes high by relaxation process of electron.

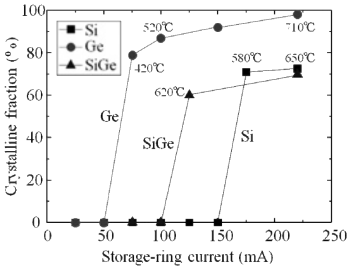

Fig. 1. Crystalline fraction of Si, Ge SiGe films as a function of storage-ring current.

Figure 2 shows Raman spectra of SiGe with irradiation area at 220mA and non irradiation area. The crystalline fraction of Si-Si, Ge-Ge and Si-Ge were 57%, 67% and 86%, respectively. It is known that binding energy of Ge-Ge and Si-Si are 2.8 eV and 3.4 eV, respectively. Atomic migration of Ge atoms is influenced by soft X-ray irradiation more strongly than Si atoms. Therefore, it is easy to form quasi-nuclei of Ge compared with Si.

For SiGe, the crystalline fraction estimated from Ge-Ge peak is larger than that of Si-Si peak. The Si-Si bond is stronger than the Ge-Ge bond. Therefore, it is easy to make quasi nuclei of Ge. Crystallization of SiGe caused by the vibration due to soft X-ray might be effective compared with thermal annealing.

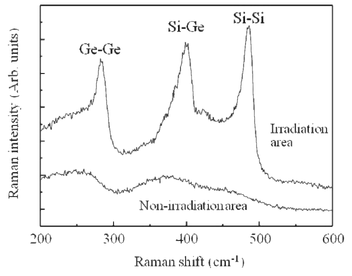

Fig. 2. Raman spectra at irradiated and non -irradiated area of SiGe film.

Photoelectron Spectroscopy Study of the Valence Band Region in Diamond-Like Carbon Thin Films

Yuichi Haruyama[1], Teruyuki Kitagawa[1], Shinji Matsui[1], Noriaki Toyoda[2], and Isao Yamada[2]
[1] Laboratory of Advanced Science and Technology for Industry, University of Hyogo
[2] Graduate School of Engineering, University of Hyogo

Abstract

Photoelectron spectra of the valence band region in diamond, diamond-like carbon (DLC), glassy carbon, and graphite were measured in order to investigate the influence of the carbon atom coordination on photoelectron spectra. Differences in the photoelectron spectra were observed, depending on the coordination of the carbon atoms. The photoelectron spectra for DLC and glassy carbon were compared to those simulated using the photoelectron spectra for diamond and graphite. From this comparison, it was found that the photoelectron spectra in DLC could not be simply reproduced using those for diamond and graphite. In addition, the photoelectron spectra of the valence band region in DLC were compared to the density of states previously calculated using the molecular dynamics method.

Introduction

Diamond-like carbon (DLC) is an amorphous material composed of sp^2 and sp^3 carbon, with negligible presence of sp carbon. DLC thin films have very interesting properties, such as high hardness, low friction coefficient, and chemical inertness, and therefore, studies on DLC films have attracted significant attention for a potentially wide range of applications. The properties of DLC films are related to the coordination of C atoms, such as sp^2 and sp^3 carbon [1]. Estimation of the sp^2 content is one of the important subjects in studies on DLC films; the sp^2 content in DLC films has been determined using electron energy loss spectroscopy and near-edge X-ray absorption fine structure (NEXAFS) studies [1]. Recently, the sp^2 and sp^3 content of DLC films was directly evaluated from X-ray photoelectron spectroscopy (XPS) spectra of the C 1s core-level region. Although photoelectron spectroscopy studies of the valence band region are important to investigate the electronic structure, such as the density of states, the orbital characteristic, there are few reports on photoelectron spectra of the valence band region in DLC. In particular, the evolution of photoelectron spectra of the valence band region as a function of the sp^2content has not been clarified.

Experiments and Results

DLC films obtained using gas cluster ion beam (GCIB) assisted deposition were formed by irradiating Ar cluster ion beams. Three DLC films were formed with acceleration energy of the Ar cluster ions of 5, 7, and 9 kV. Glassy carbon, graphite, and diamond were also prepared for comparison. In our previous XPS study of the C 1s core level in DLC films formed by GCIB deposition [1], the sp^2 and sp^3 content were estimated. With increasing acceleration energy of the Ar cluster ions, from 5 to 9 kV, the sp^2 content in the DLC films increased from 49 to 62 %. Similarly, the sp^2 and sp^3 content in the glassy carbon were estimated to be 95 and 5 %, respectively. For the DLC films formed by the GCIB deposition, the sp^2 content was estimated [1].

Figure 1 shows the photoelectron spectra of the valence band region in graphite, glassy carbon, three different DLC films, and diamond. All the photoelectron spectra are composed of a dominant feature between 12 and 0 eV and a small feature between 22 and 12 eV. As discussed later, the features between 22 and 12 eV and between 12 and 0 eV are predominantly derived from the C 2s and C 2p states, respectively. In the case of graphite, several peaks were observed at ~19.0, ~13.0, ~10.0, ~7.8, ~5.5, and ~3.0 eV. In glassy carbon, three peaks at ~19.0, ~13.0, and ~7.8 eV were clearly observed. However, the other three peaks at ~10.0, ~5.5, and ~3.0 eV were barely visible. In the case of the three DLC films, five peaks were observed, at ~19.0, ~13.0, ~10.0, ~7.0, and ~3.8 eV. The intensity of the peak at ~10.0 eV was higher than that in graphite and glassy carbon. Also, the intensity of the peak at ~3.0 eV decreased compared to that in graphite and glassy carbon. Therefore, a clear peak at ~3.0 eV was not observed. A peak at ~3.8 eV instead of ~3.0 eV appeared in the spectra for the three DLC films. With decreasing acceleration energy of the Ar cluster ions from 9 to 5 kV, the feature between 12 and 0 eV in DLC films was broader. In diamond, several peaks were observed, at ~19.0, ~16.5, ~13.0, ~10.0, ~6.5, and ~3.8 eV. We discuss the evolution of the photoelectron spectra in the valence band region as a function of the sp^2 content. At first, the photoelectron spectra in graphite and diamond were convoluted by a Gaussian function to simulate the amorphous state. Next, the convoluted photoelectron spectra in graphite and diamond were summed, depending on the ratio of the sp^2 and sp^3 content. The simulated photoelectron spectra (thin lines) in glassy carbon and the three DLC films are shown in Fig. 1. In glassy carbon, the photoelectron spectrum is similar to the simulated one. It was found that the photoelectron spectrum in glassy carbon is well reproduced using the simulated photoelectron spectra. In the case of the three DLC films, the intensity of the peak at ~10.0 eV is larger while the intensity of the peak at ~3.0 eV is smaller than the simulated photoelectron spectra. With increasing the sp^3 content, the intensity of the peaks at ~10.0 and ~3.0 eV increased. Thus, except for the peaks at ~10.0 and ~3.0 eV, the photoelectron spectra seem to be reproduced using the simulated photoelectron spectra.

Figure 2(a) shows the photoelectron spectra of the valence band region in the DLC film with acceleration energy of the Ar cluster ions at 5 kV as a function of the excitation energy. The photoelectron spectrum at 70 eV is composed of a dominant feature between 12 and 0 eV and a small feature between 22 and 12 eV. From the photon energy dependence, the feature between 22 and 12 eV is predominantly derived from the C 2s state, respectively. On the other hand, the feature between 12 and 0 eV is predominantly derived from the C 2p state. In a previous study on amorphous carbon [2], the total and partial density of states were calculated by the MD method. The partial s and p_σ density of states were distributed with peaks at ~18 and 8 eV, respectively. In the previous study [2], the total density of states was also compared to the photoelectron spectrum measured at 1486.6 eV. For the excitation energy, the intensity of the C 2s state was dominant. Since the intensity of the C 2p state is relatively small, it is difficult to compare the photoelectron spectrum and the density of states calculated by the MD method as for the C 2p state. At lower excitation energies, the cross section of the C 2p states is almost identical to that of the C 2s states. Therefore, at a lower excitation energy, the photoelectron spectrum would be compared to the density of states with reasonable intensity as for the C 2p states as well as the C 2s states. In Fig. 2(b), the photoelectron spectrum in the DLC film with acceleration energy of the Ar cluster ions of 5 kV was compared to the density of states (solid line) as calculated by the MD method [2]. In the MD calculation, the sp^3 content was 61 % while it was estimated to be 51-57 % in the DLC film. Since the difference in the sp^3 content is within 10 %, it is considered that there is no significant variation for the comparison between the density of states calculated by the MD method and our photoelectron spectra. Partial s, p_σ and p_π density of states (dotted line) are also plotted in Fig. 2(b). On the whole, the photoelectron spectrum seems to be consistent with the density of states calculated by the MD method. However, the position of the p_σ state shifted to the higher binding energy side as compared to the photoelectron spectrum. In addition, the intensity of the p_π state was larger compared to the photoelectron spectrum. As discussed in the previous paper [2], the binding energy of the p_σ state was overestimated in the MD calculation. In addition, the p_π state was enhanced since the interlayer interaction was neglected [2]. If these were modified, the density of states calculated by the MD method would be much more in correspondence with the photoelectron spectrum.

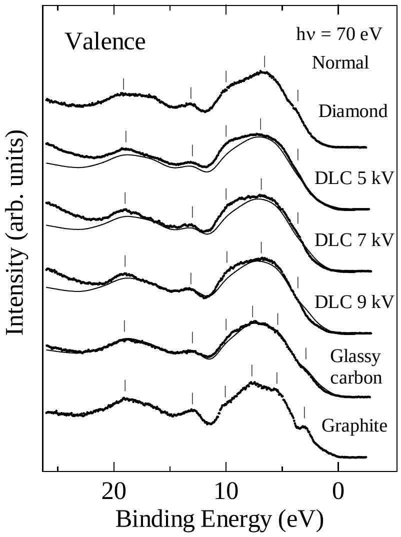

Figure 1. Photoelectron spectra (dots) of the valence band region in graphite, glassy carbon, three DLC films, and diamond. In glassy carbon and the three DLC films, simulated photoelectron spectra (thin lines) are also shown. The spectra were normalized by the maximum peak intensity.

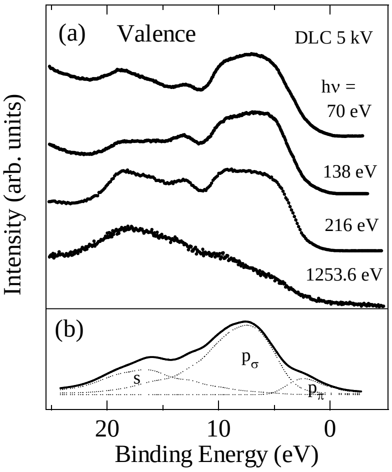

Figure 2. (a) Photoelectron spectra (dots) of the valence band region in the DLC film formed with acceleration energy of the Ar cluster ions at 5 kV as a function of the excitation energy. (b) Photoelectron spectrum (dots) of the valence band region in the DLC film formed with the acceleration energy of the Ar cluster ions at 5 kV and the total (solid line) and partial (dotted lines) density of states calculated by the MD method.

References

[1] Y. Haruyama *et al.*, Jpn. J. Appl. Phys. **47**, 3380 (2008).
[2] J. Schafer *et al.*, Phys. Rev. **B 53**, 7762 (1996).

Characterization of Crystalline Structure of BN Thin Film using Soft X-ray Absorption Spectroscopy

Masahito Niibe[1], Takuya Kotaka[1], Satoko Hori[2], and Shozo Inoue[2]
LASTI [1] & Graduate School of Eng., [2] University of Hyogo

Abstract

Crystalline structure of BN thin film prepared by magnetron sputtering technique was characterized using the soft X-ray absorption spectroscopy (XAS). Boron and nitrogen K-edge X-ray absorption near edge structures (XANES) of the BN thin film were measured with total electron yield (TEY) method and total fluorescence yield (TFY) method. The obtained spectra indicate that the crystal structure of prepared BN film is very similar to that of cubic boron nitride (c-BN) powder. This study also suggests the effectiveness of XANES spectroscopy for evaluation of crystalline structure of BN thin films.

Introduction

As similar to carbon allotropic forms, boron nitride presents a polymorphism of hexagonal structure (h-BN) having a hexagonal plane network, such as graphite, and cubic structure (c-BN) having a steric structure, such as diamond. It is well known that h-BN is a relatively soft material. However, c-BN is known to be the second hardest material after diamond, and preparation of c-BN thin film is extensively studied for a coating material onto cutting tools. Moreover, it comes to the front of application to electronic and photo-electronic devices as one of the wide-gap semiconductor materials.

In cases of BN thin film fabrication by sputtering or ion plating depositions, h-BN structure is preferentially formed because it is a stable phase at normal pressures. Stably-forming technology for c-BN structured thin film was not confirmed as affairs. Characterization of crystalline structure of BN thin film is indispensable to confirm the fabrication technology. However, application of X-ray diffraction method to the thin film characterization is very difficult because the atomic scattering factors for these light elements (B and N) are very small.

On the other hand, X-ray absorption near edge structure (XANES) measurement is an appropriate technique to identify the crystal structure of BN thin film because the spectra of c-BN and h-BN are quite distinct and the bonding state on sp^2 and sp^3 can be observed in isolation. In this study, XANES spectroscopy at B-K and N-K edge was carried out for the characterization of crystalline structure of BN thin film prepared by an RF magnetron sputtering method.

Experiments

BN thin films were prepared on Si wafer (100) by the RF magnetron sputtering system. An h-BN disk (38 mm in diameter) was used as target material. The substrate holder was electrically floated for applying a bias voltage and could be heated up to 600 ℃ simultaneously. Ar+N_2 mixed gas was used as working gas, and its pressure was changed from 0.2 to 1.0 Pa. The DC bias was changed from -75 to 120 V in this study. Atomic composition of the prepared sample was determined by an Auger electron spectroscopy (AES).

B-K and N-K XANES spectra of prepared samples were measured in the analyzing station of the beamline BL9a at the NewSUBARU SR facility. The beamline monochromator was mounted with a plane varied-space grating with central groove density of 1200 l/mm, the energy resolution of which was about 0.2 eV at the photon energy of 400 eV [1].

The measurement was conducted with a total electron yield (TEY) method with sample current mode and with a total fluorescence yield (TFY) method with measuring the amount of fluorescence by a photodiode. The TEY and TFY measurements were carried out simultaneously for the same sample at the same position. Self-absorption effects in TFY measurement were not corrected here for simplicity. It is well known that the TEY method can yield information in a shallow region from the sample surface because of the small escape length of photo-generated electrons of less than about 5nm [2]. Meanwhile, the TFY method can yield information in a deeper region (bulk) of the sample of more than 100 nm because of the much longer penetration depth of soft X-ray photons.

Results and discussion

Figures 1 and 2 show the B-K and N-K absorption spectra, respectively, of a prepared BN thin film together with the spectra of the standard samples of h-BN and c-BN powder. The spectra of B-K and N-K absorption for h-BN powder sample have sharp π* resonance peaks at 192 eV for B-K and at 401 eV for N-K edges, respectively, which are caused from sp^2 bonding states like a graphite. The π* resonance peaks have a dependency of incident angle, which is originated from an orientation of hexagonal plane network of h-BN structure. On the other hand, the spectra of B-K and N-K absorption for c-BN powder sample do not have a π* resonance peaks and also do not have a dependency of incident angle.

In the spectra of the prepared sample as shown in Fig. 1 and 2, the π^* resonance peaks in B-K or N-K edges are almost not observed. These results indicate that the crystalline structure of the prepared BN film could be very close to that of the c-BN crystal. The results also correspond well to the result of infrared absorption spectra measured with FTIR spectrometer [3].

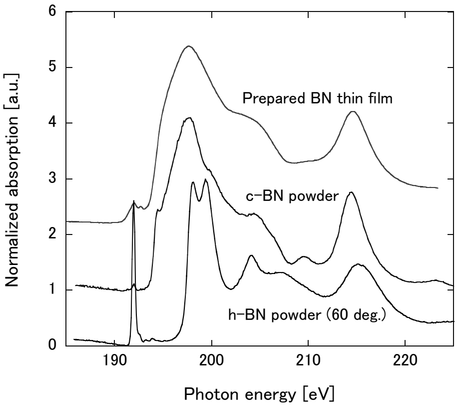

Fig. 1 B-K XANES spectra of a prepared BN thin film and standard h-BN and c-BN powders.

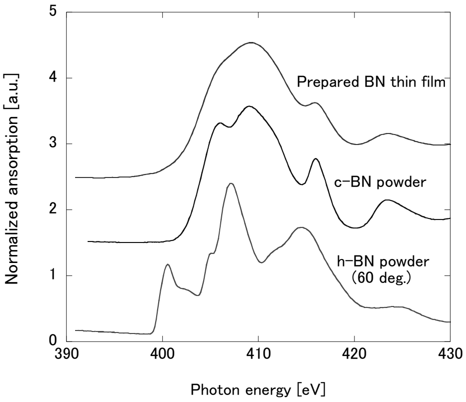

Fig. 2 N-K XANES spectra of a prepared BN thin film and standard h-BN and c-BN powders.

B-K XANES spectra (TEY) at angles of incidence of 90° and 45° for the prepared BN film with mixture of c-BN and h-BN phases are shown in Fig. 3. Although the spectra for the h-BN rich mixture phase sample are not shown here, the π^* resonance peak of the h-BN rich sample shows a small dependency of incident angle. However, the angular dependency almost disappeared for the c-BN rich mixture phase sample as shown in Fig. 3.

Figure 4 shows the N-K XANES spectra (TEY and TFY) at angles of incidence of 90° and 45° for the prepared BN film with mixture of c-BN and h-BN phases. The angular dependency of the π^* resonance peak was almost not observed as same as that of the B-K spectra in Fig. 3. Comparing the spectra obtained by TEY and TFY method, the intensity of π^* resonance peak at 401 eV in the TFY spectra is much higher than that in the TEY spectra. This result indicates that the concentration ratio of h-BN phase could be relatively higher inside the thin film, though the ratio of c-BN could be much higher at the film surface.

The results obtained in this study suggests the effectiveness of X-ray absorption (XANES) spectroscopy for evaluation of crystalline structure of BN thin films.

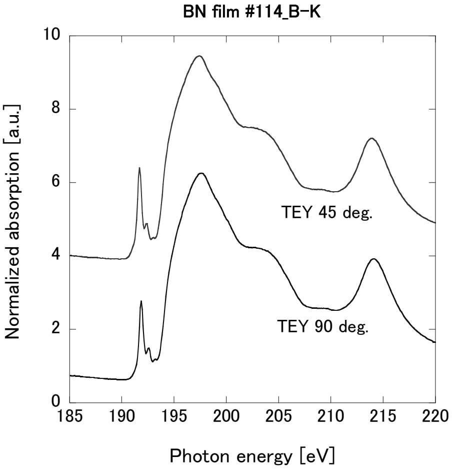

Fig. 3 B-K XANES spectra of a prepared BN thin film with mixture phases of h-BN and c-BN.

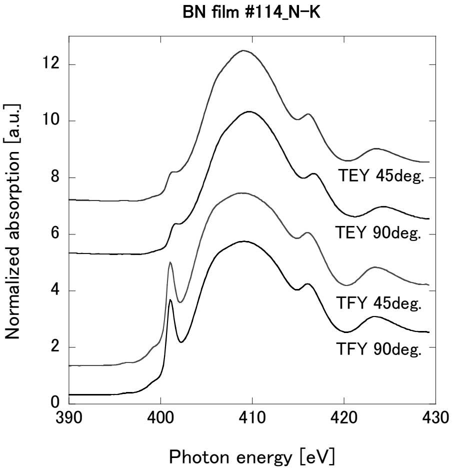

Fig. 4 N-K XANES spectra of a prepared BN thin film with mixture phases of h-BN and c-BN.

References

[1] M.Niibe *et al.*, AIP Conf. Proc., **705**, 576, (2004).
[2] J. Stohr, “NEXAFS Spectroscopy” Springer, Berlin (2003).
[3] S. Hori *et al.*, Proc. ISSP2011, Kyoto, (2011) accepted.

Modification of Electronic States of Multi-walled Carbon Nanotubes by Ion Irradiation

S. Honda[1], S. Nanba[1], Y. Hasegawa[1], M. Niibe[2], and M. Terasawa[2]
[1]*Univ. of Hyogo*, [2]*LASTI Univ. of Hyogo*
R. Hirase[3], H. Yoshioka[3], and H. Izumi[3]
[3]*Hyogo Pref. Inst. of Tech.*

Abstract

Low energy Ar ions (0.5 - 2 keV) were irradiated to vertically aligned multi-walled carbon nanotube (MWCNT) films. The structural properties and local bonding configurations of the irradiated vertically aligned MWCNT films were characterized. It was found that the irradiation disrupted π and σ bonds, and after the high ion dose, MWCNT bundles were formed. This may be originated from bending of MWCNTs or welding between plural MWCNTs under the ion irradiation.

Introduction

Irradiating carbon nanostructures with energetic particles is thought to tailor the structure and properties of the carbon nanostructures, and can be applied to nanodevice fabrication. It was reported that spatially localized Ar ion irradiation of individual MWCNTs deposited SiO_2 substrates was used for fabrication of quantum dots [1]. Moreover, Ar ion irradiation of MWCNTs enhanced the field-emission properties due to defects induced by the ion irradiation [2]. In this study, low energy Ar ions (0.5 - 2 keV) were irradiated to vertically aligned MWCNT films, and the structural properties and local bonding configurations of the irradiated vertically aligned MWCNT films by Raman spectroscopy and X-ray absorption near-edge structure (XANES), respectively. In addition, scanning electron microscopy (SEM) and transmission electron microscopy (TEM) were utilized to characterize structural properties of the irradiated MWCNT films.

Experiments and Results

Vertically aligned MWCNT films were synthesized by catalytic chemical vapor deposition (CCVD). Figure 1(a) and 1(b) show SEM image of a vertically aligned MWCNT film and its magnified image, respectively. Aligned MWCNTs ~160 μm in length with radii ranging between 20 and 40 nm were grown densely. An ion gun (ULVAC-PHI, USG-3) is employed as the ion source. Ar ions with energies ranging between 0.5 and 2 keV were irradiated to the MWCNT films. The ion dose was varied between 1×10^{15} and 1×10^{17} cm^{-2}. Micro-Raman spectra were taken with Ar ion laser (514.5 nm) using a Raman spectroscope (JASCO, NRS-2100). The carbon K-edge XANES measurement was performed in beam line BL9 at NewSUBARU.

Raman spectroscopy showed that Ar ion irradiation changed the intensity ratio of integrated D (1355 cm^{-1}) and G peak (~1580 cm^{-1}) areas, I_D/I_G, indicating disorder changes the nature of in-plane bonding of MWCNT sheets, deviating away from intrinsic sp^2 character [3,4]. The XANES spectra of vertically aligned MWCNT films irradiated with different energies of Ar ion at a dose of 5×10^{15} cm^{-2}, and vertically aligned MWCNT films irradiated with a 1 keV Ar ion at different doses are shown in Fig 2(a) and 2(b), respectively. In the spectrum for as-prepared MWCNT films, π^* peak at 285 eV related to carbon sp^2 atoms and σ^* peak at 292 eV related to carbon sp^2, sp^3 atoms were clearly observed. On the other hand, after the Ar ion irradiation, with increasing the ion accelerated energy and dose, both heights of π^* and σ^* peaks are decreased, and width-broadening of σ^* peak is recognized. The XANES analysis supports the results from Raman spectroscopy.

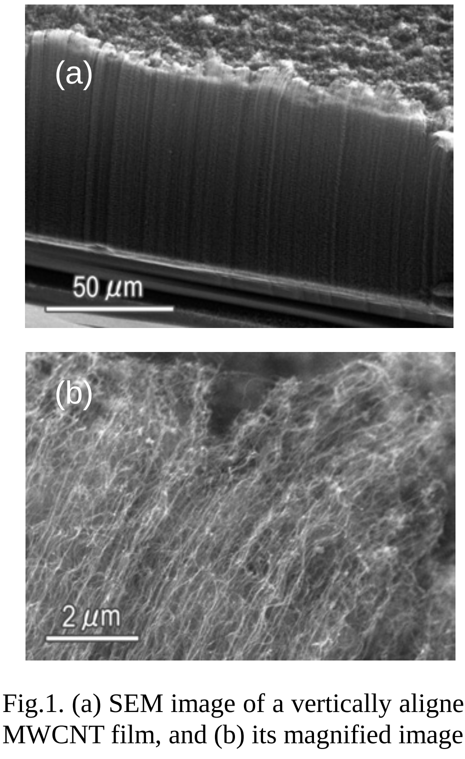

Fig.1. (a) SEM image of a vertically aligned MWCNT film, and (b) its magnified image.

Figure 3(a) and 3(b) show SEM images of an as-prepared vertically aligned MWCNT film, and a vertically aligned MWCNT film irradiated with 1 keV Ar ion at a dose of 5×10^{16} cm^{-2}, respectively. SEM observation revealed that irradiation with the higher dose of 5×10^{16} cm^{-2} led to self-organization in the MWCNT films that tended to form bundles. This may be originated from bending of MWCNTs or welding between plural MWCNTs under the ion irradiation.

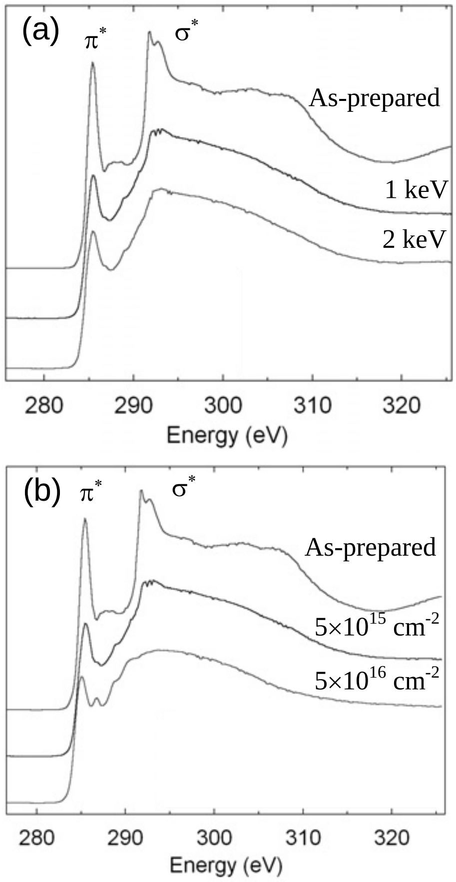

Fig.2. (a) XANES spectra of vertically aligned MWCNT films irradiated with different energies of Ar ion at a dose of 5×10^{15} cm^{-2}, and (b) vertically aligned MWCNT films irradiated with a 1 keV Ar ion at different doses.

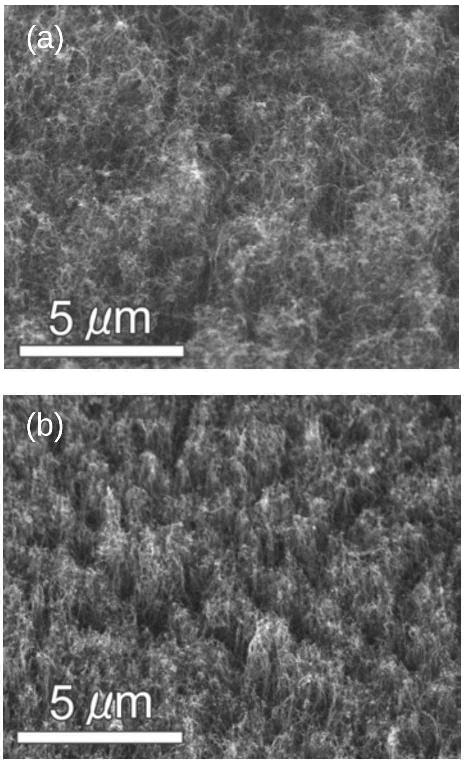

Fig.3. SEM images of (a) an as-prepared vertically aligned MWCNT film, and (b) a vertically aligned MWCNT film irradiated with 1 keV Ar ion at a dose of 5×10^{16} cm^{-2}.

References

[1] M. Suzuki *et al.*, *Appl. Phys. Lett.* **81**, 2273 (2002).

[2] D. -H. Kim *et al.*, *Chem. Phys. Lett.* **378**, 232 (2003).

[3] F. Tuinstra and J. L. Koenig, J. Chem. Phys. **53**, 1126 (1970).

[4] K. Niwase and T. Tanabe, Mater. Trans., JIM **34**, 1111 (1993).

Damage analysis of gallium nitride crystals etched by He and Ar plasma

Takuya KOTAKA[1], Masahito NIIBE[1], Retsuo KAWAKAMI[2], Takeshi INAOKA[2],
Kikuo TOMINAGA[2], and Takashi MUKAI[3]
[1]Laboratory of Advanced Science and Technology for Industry, University of Hyogo
[2]Institute of Socio-Techno Science Technology, The University of Tokushima, Japan
[3]NICHIA Corporation, Japan

Abstract

Effect of etching damage on n-GaN crystal using a capacitively-coupled radio frequency plasma with He and Ar gases was investigated. Local atomic structure of the etched surface was evaluated by soft X-ray absorption spectroscopy (XAS) method. From N-K absorption spectra of GaN surfaces etched by Ar plasma, disordered crystal structure was observed. From the spectra of the surfaces etched by He plasma, the observed disarray of crystal structure was lower than that etched by Ar plasma.

Introduction

GaN is expected to apply as semiconductor devices using under a harsh environment. Precise control of etching by nanoprocess plasma is necessary to realize higher performance of the GaN semiconductor devices. However, the reaction of nanoprocess plasma on the surface is so complicated that the understanding for precise control is insufficient at the present [1]. To understand a mechanism of defect creation by physical etching, Kawakami et al. have etched n-GaN crystal using a capacitively-coupled radio frequency (RF) plasma reactor with rare gas of Ar and evaluated various characteristics [2,3].

In this work, to deepen the understanding of the control of etching plasma, n-GaN crystal surfaces were etched by capacitively-coupled RF plasma reactor using He and Ar gases. Effect of etching damage on the surface was analyzed by soft X-ray absorption spectroscopy (XAS). The results of etching damage by He and Ar plasma are compared.

Experiment

GaN crystal was etched using a capacitively-coupled RF plasma reactor with unbalanced electrode structure [4] at the constant self-bias voltage of 200 V with changing gas pressure (10~100 mTorr) and treatment time (5~200 min). Rare gases of He or Ar were used as plasma source gas. The sample was a Si-doped GaN with a thickness of 2μm grown on sapphire substrates by Metal Organic Chemical Vapor Deposition (n-GaN, Nichia Co.).

The XAS measurement was carried out at the BL-9A. N-K edge absorption spectra were obtained to analyze the atomic local structure of the etched surfaces. The measurement was carried out with a total electron yield (TEY) method with sample current mode and with a total fluorescence yield (TFY) method with measuring the amount of fluorescence by a photodiode. An escape depth of electron by a photoelectric effect at the energy of 400 eV is less than about 5 nm [5]. Therefore, TEY method can analyze in a shallow region at the surface. TFY method can analyze in a deep region from the surface (bulk), because the penetration depth of soft X-rays is more than 100 nm. The photodiode was set at the angle of 30 deg. from the incidence light and lower left sight from the sample. The distance between the photodiode and the sample was about 20 mm. The used photodiode was AXUV-100 (IRD Co.) with Al coating of 40 nm thick for avoiding the yellow band secondary emission.

Results and discussion

Figure 1 shows the N-K absorption spectra of n-GaN etched with He and Ar plasma at the treatment time of 200 min and normalized by peak intensities at the photon energy of 404 eV. Figs. 1(a), (b) and Figs. 1(c), (d) are the spectra measured by TEY and TFY methods, respectively. Figs. 1(a) and (c) are the spectra of the surfaces etched with He plasma. Figs. 1(b) and (d) are the spectra of the surfaces etched with Ar plasma.

The peak at photon energy of 400 to 412 eV shown in the as-grown sample has complicated shape. According to the previous report by Katsikini et al. [6], those peaks are explained with superposition of six Gaussian peaks named G1~G6.

Deenapanray et al. reported [7] that the N-K absorption spectra of GaN were changed by Ar ion bombardment. In Fig. 1(b), the peak shapes (two shoulders at both sides of the sharp peak near 404 eV and others) became smoother (dull) with increasing gas pressure from 10 to 100 mTorr. The change indicates that the crystal structure of GaN was disordered by Ar plasma etching. In Fig. 1(a), the peak shapes (two shoulders at both sides of the sharp peak near 404 eV and others) became a little smoother (dull) with increasing gas pressure from 10 to 100 mTorr. The change indicates that the crystal structure of GaN was disordered by He plasma etching. As shown in Fig. 1(c) and (d), the peak shape in spectra measured by TFY method was not changed. Therefore, the disarray of crystal structure was occurred at shallow region in sample surface.

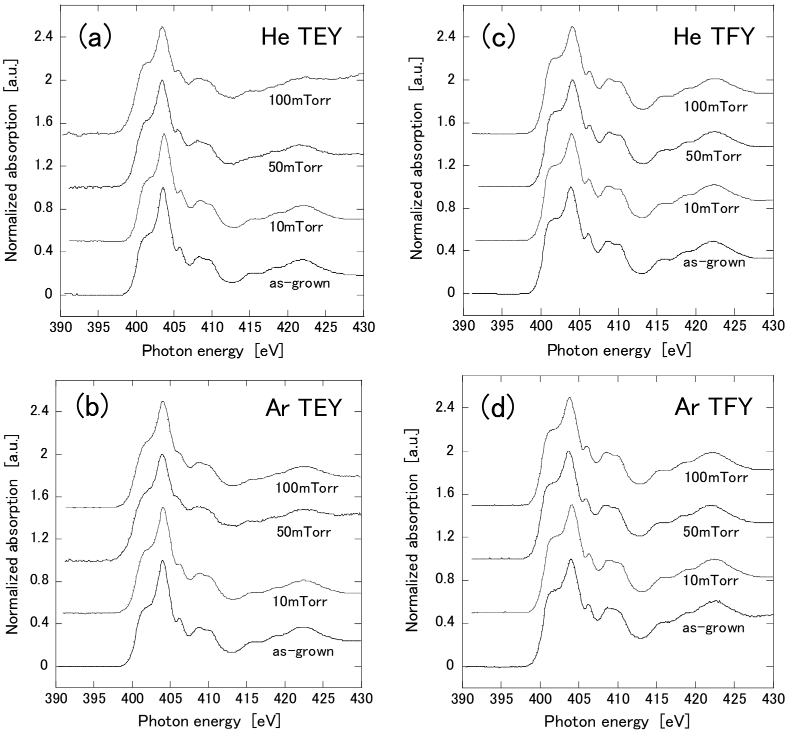

Figure 1 Normalized N-K absorption spectra of GaN crystal etched and measured by (a): He plasma and TEY method, (b): Ar and TEY, (c): He and TFY, (d): Ar and TFY, respectively, at the treatment time of 200min.

Figure 2 shows the maximum elastic energy transfer ratio of He and Ar ion to atoms in various nitride solid calculated with the PIS (Plasma behavior and its Interaction with Surface reaction) particle model [4]. In Fig. 2, the elastic energy transferred from He ion to N and Ga atoms is less than the one from Ar ion. That is, the impact of He ion on N and Ga atoms have a less influence on N and Ga atoms than the one of Ar ion. In Fig. 1(a), the change in spectra of the surfaces etched by He plasma was less pronounced depending on gas pressure than the one etched by Ar. Therefore, the disarray of crystal structure in GaN etched by He plasma is lower than that etched by Ar plasma.

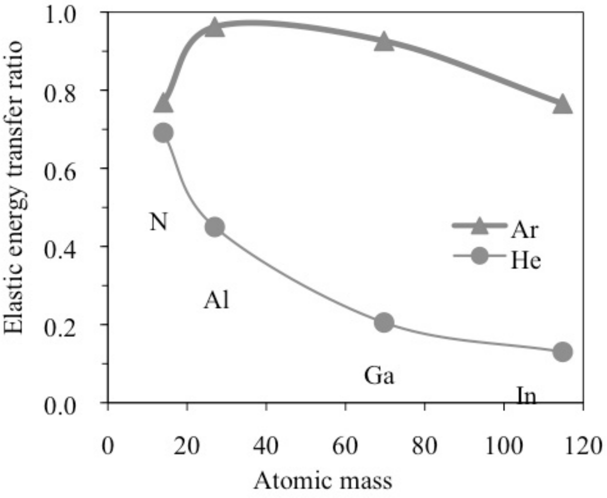

Figure 2 Maximum elastic energy transfer of He and Ar ion to atoms in various nitride solid.

Conclusions

The disordering of crystal was observed on the GaN surfaces etched by Ar plasma, and it became greater with increasing gas pressure. However, the disarray of crystal structure on the surface etched by He plasma was less pronounced. Comparing the XAS spectra obtained by TEY and TFY method, it was found that the changes in surface composition and crystalline disordering were occurred only in the shallow region from the n-GaN surface.

References

[1] S. J. Pearton, J. C. Zolper, R. J. Shul, and F. Ren, J. Appl. Phys. **86** (1999) 1.
[2] R. Kawakami, T. Inaoka: Vacuum, **83** (2009) 490.
[3] R. Kawakami, T. Inaoka, K. Tominaga, and T. Mukai, Jpn. J. Appl. Phys. **48** (2009) 08HF01.
[4] R. Kawakami, T. Inaoka, K. Tominaga, A. Kuwahara, and T. Mukai, Jpn. J. Appl. Phys. **47** (2008) 6863.
[5] J. Stohr: "*NEXAFS Spectroscopy*", Springer-Verlag, 1996.
[6] M. Katsikini, E. C. Paloura, and T.D. Moustakas, J. Appl. Phys. **83** (1998) 1437.
[7] P. N. K. Deenapanray, M. Petravic, K. –J. Kim, B. Kim, and G. Li, Appl. Phys. Lett. **83** (2003) 4948.

A Development Plan of Sputtering System for Large Scale Telescope Mirror Coating at Nishi-Harima Astronomical Observatory

Makoto Sakamoto[1], Fumiaki Tsumuraya[1] and Masahito Niibe[2]
[1]Nish-harima Astronomical Observatory, University of Hyogo,
407-2 Nishigaichi, Sayo-cho, Sayo-gun, Hyogo 679-5313, Japan
[2]Laboratory of Advanced Science and Technology of Industry, University of Hyogo
3-1-2 Kouto.Kamigoori-cho, Ako-gun, Hyogo 678-1205, Japan

Abstract

The “Nayuta” astronomical telescope, having the largest mirror in Japan of 2 m diameter, is operating at the Nishi-Harima Astronomical Observatory. To maintain the reflectivity of the telescope mirrors, we are planning to develop a recoating system for large scale mirrors. The system is necessary to meet the following requirements. 1: The coating quality satisfies the demands in astronomical observation. 2: The coating can be carried out with mirror surface in upward direction. 3: The system is possible to pile up a protection coating. 4: silver metal can be also coated instead of standard aluminum metal in the future. We selected a downward sputtering as a coating system that enabled these requirements. In this paper, we report the specification of the sputtering system and the preliminary experiment for extracting problem in the coating of telescope mirrors.

1. Introduction

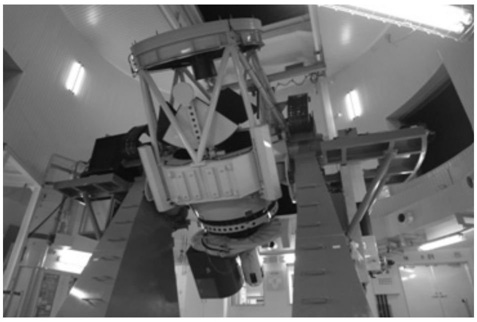

A large scale astronomical telescope, named “Nayuta”, has been operated at the Nishi-Harima Astronomical Observatory in Hyogo prefecture (Fig.1). The telescope is Cassegrain type constructing with a 2m primary mirror and a 30 cm secondary mirror, and the scale is the largest within Japan. The mirrors used in the telescope must be recoated at least in every five years, because of aging deterioration and resulting decrease in reflectivity. However, there is no appropriate coating system inside Japan in the present state of affairs. Therefore, we are planning to develop a recoating system operating within the observatory facility for reductions of shipping cost, risk of fatal damage to the mirrors and dead time of the telescope operation.

Traditionally, coating of many telescope mirrors was conducted by vacuum evaporating deposition. However, because of the expectation of improving reflectivity and environmental durability, we chose a sputtering method for the coating. Sputtering method is also advantageous for the risk of fatal damage because the method can easily deposit material to downward direction on a large scale mirror substrate keeping the surface with upward direction.

2. Coating material

A large part of electro-magnetic radiation from celestial objects is reflected or absorbed by earth’s atmosphere. The wavelength regions of the electric-magnetic radiation reached to ground is limited as shown in Fig. 2. A lot of ground-based optical telescope can observe these wavelengths in visible light and a part of near-infrared (NIR) and ultraviolet (UV) radiations. The reflective coating must have enough reflectivity in these observing wavelengths. Moreover, we must examine protective coating because the environment of observation is similar to that of out-door. The coated surface has to be guarded from dust and humidity.

2-1. Reflective coating

Aluminum coating has been used in a lot of telescope mirrors because aluminum has good reflectivity from UV to NIR region as shown in Fig. 2. However, the number of observatories having silver coated telescope was increasing, recently, because the CCD camera, the sensitivity of which is rather low in the UV region, became a mainstream

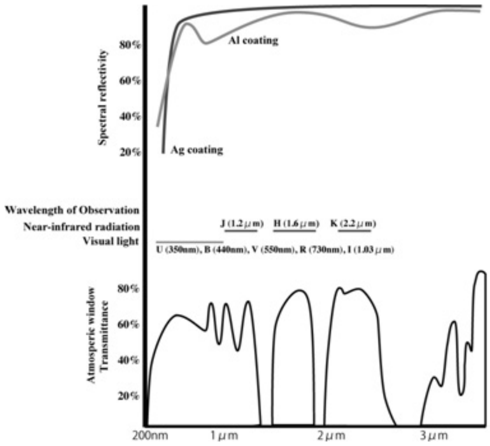

Fig. 2 Spectral reflectivity of coating

observation instrument. It is also because the infrared camera has been developed, which enable us to observe NIR regions of J(1.2 μm), H(1.6 μm), and K(2.2 μm) bands.

In Nayuta telescope, the dominant observing wavelength is visible light using CCD camera and NIR radiation using infrared camera. Therefore, we plan to provide the function of silver coating in a future.

2-2.Protection coating

The telescope is exposed to the open air during the observation. It was reported that the reflectivity of the telescope mirror was deteriorated to the level of 60% even in a year [1] because of the high humidity in Japan.

A lot of telescopes specialized to academic studies are without protection coating. On the other hand, a number of telescopes opened to the public, including Nayuta, have a protection coating. It will take one month or longer to recoat the mirror involving the work of removing from and installing to the Nayuta mirror cell. The working time corresponds to above 10% of all the operation time. It is hard to keep the maintenance time of one month for every year.

The suppression of the reflectivity deterioration can be expected by the additional protection coating. And it will enable us to clean the dust of the mirror surface without fatal damages, too.

3. Quality of coating

Several factors have to be taken into account for the error of mirror accuracy, such as an accuracy of polishing, changing posture of telescope, and thermal deformation of both mirror and cell. The specification of Nayuta telescope permits the error of mirror polishing within 0.07". The surface accuracy of mirror glass is less than 16.8 nm(rms). The surface accuracy of coated mirror is less than 26.3 nm(rms). The surface roughness of the coating on the mirror is under 2 nm(rms) [2]. In this experiment, target of the surface roughness of the coated mirror is 3% or less of the coating film thickness. Considering above, we estimate the thickness of coating film that will have an enough reflectivity.

4. Basic specifications of the coating system

According to the consideration as mentioned above, the basic specifications of the coating system are as follows,

1) The coating on the mirror surface is performed by a downward-sputtering method.
2) The size of mirror substrate is 2 m in diameter and 20 cm thick with central hole of 50 cm in diameter.
3) The reflection coating material is aluminum or silver.
4) The roughness of coated surface is less than 2 nm(rms).
5) The protection coating is available. The material is SiO.

5. Preliminary experiment

To understand the details of the coating and removal of reflection film on the mirror, we are carrying out a preliminary experiment with the use of a small size vacuum evaporation system (ANELVA EVD-500A) and the magnetron sputtering system (TOKUDA CFS-8EP). We are optimizing the deposition condition for aluminum thin film. The deposited thin films were evaluated with film thickness by stylus profiler (Veeco Dektak2A) and with surface roughness by atomic force microscope (Seiko Instruments Inc. NanoNavi , S-image). Fig. 3 shows the surface profile of aluminum thin films deposited by (a) EB evaporation and (b) sputtering deposition. We are also examining a protection coating using SiO.

Moreover, we are developing a spectral reflectometer for visible light and near infra-red radiation using a fiber spectrometer (Ocean Optics USB4000). The measuring method is relative reflectivity comparing with aluminum reference mirror. Using the reflectometer, we will evaluate not only the reflectivity of the coating but also the time deterioration of the reflectivity. We are also examining the method of removal of coated materials by wet chemical process and evaluating the damage to the mirror glass surface. Finally, we are also examining the cost of coating system and its running cost.

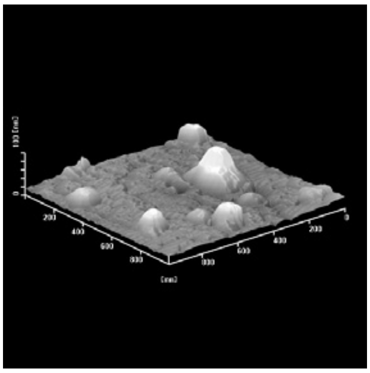

(a)EB evaporation

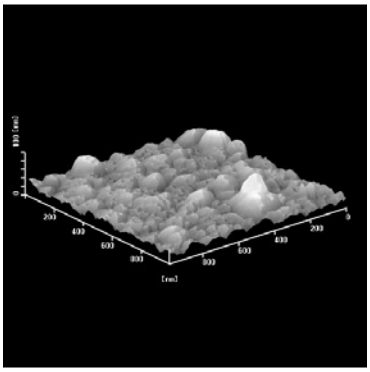

(b)Sputtering

Fig.3 Surface profile of aluminum thin films.

[1]E.Watanabe,et.al: REPORT OF THE NATIONAL ASTRONOMICAL OBSERVERTORY OF JAPAN (1995) Vol.2,No.3

[2]Mitsubishi Electric Corporation: Detailed specification in production of large-scale telescope (2004)

Fabrication of Carbon Membrane X-ray Mask for Deep X-ray Lithography Technique

Daiji Noda[1], Atsushi Tokuoka[1], Megumi Katori[2], Yasuto Minamiyama[2], and Tadashi Hattori[1]
[1]Laboratory of Advanced Science and Technology for Industry, University of Hyogo,
[2]Nanocreate Co., Ltd.

Abstract

For X-ray lithography, the accuracy of the fabricated structure depends largely on the accuracy of the X-ray mask. Conventionally, a resin material is used for the support membrane for large area X-ray masks. However, resin membranes have the disadvantage that they can sag after several cycles of X-ray exposure due to the heat generated by the X-rays. For our new proposal we used thin carbon wafers for the membrane material because carbon has an extremely small thermal expansion coefficient. This new type of X-ray mask is very easy to process, and it is expected that it will lead to more precise X-ray masks.

Introduction

X-ray imaging techniques have found applications in many fields such as medicine, biology, inspection, material science, and so on. However, clear X-ray images of samples with low absorbance, such as biological soft tissue, are not easy to obtain. To resolve this problem, several methods which use X-ray phase information have been investigated [1]. In these methods, techniques using X-ray gratings have been demonstrated [2]. X-ray Talbot interferometry (XTI) [2] is one of those techniques used for X-ray phase imaging. In XTI two X-ray gratings are used. However, the fabrication of X-ray gratings is very challenging because a thickness of 20 μm or more is required for use with 10-40 keV X-rays, even for gold which has a high X-ray absorption coefficient.

X-ray lithography [3], which uses highly directional synchrotron radiation, is one of the technologies that can be used for fabricating micrometer sized structures. The X-ray mask pattern is transferred onto the structure being fabricated due to the difference between the X-ray transmittance in the absorber and clear areas, and the precision with which the structure can be fabricated depends largely on the precision of the X-ray mask. Since, in X-ray lithography, the radiation is highly directional, a micro-fabrication technology that produces untapered and high aspect ratio highly absorbent structures on a low absorbent membrane is required.

Fabrication of carbon X-ray mask

The conventional resin membrane X-ray masks have the disadvantage that, after several cycles of X-ray exposure, they crease and sag due to X-ray-derived heat. As a substitute for the conventional resin membrane, we proposed to fabricate a new X-ray mask using a carbon wafer membrane that has an extremely small thermal expansion coefficient and is easy to process.

Figure 1 shows fabrication process using carbon wafer for membrane material. The fabrication process consists of three steps: (a) depositing a seed layer on the carbon wafer, (b) applying resist over the seed layer to perform patterning by irradiation with UV and development, (c) forming an X-ray absorber, i.e. an Au film, by electrolytic plating, We succeeded in making new X-ray mask with pitch pattern of 5.3 μm and large effective area of 100 × 100 mm^2, as shown in Fig. 2. In contrast to conventional silicon substrates, the newly devised mask fabrication process does not require further membrane application, frame adhesion or substrate etching. Thus, this is very simple process.

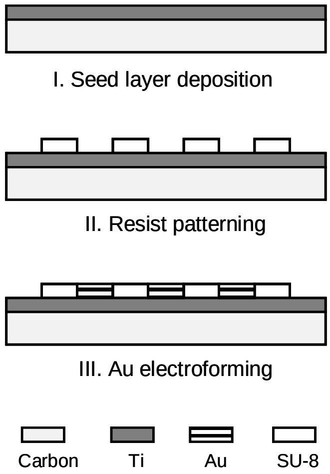

Fig. 1: *New fabrication process of X-ray mask*

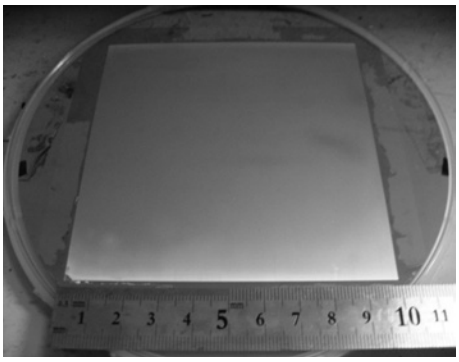

Fig. 2: *Picture of carbon X-ray mask*

Fabrication of X-ray grating

We used SU-8 photoresist for the X-ray lithography. SU-8 was originally designed for UV lithography, but it can also be used in deep X-ray lithography to produce highly accurate, high aspect ratio patterned structures. With the resin membrane X-ray masks, we can fabricate photoresist structures of about 30 μm in height with an X-ray exposure dose of 4,000 mA·s/mm. The X-ray transmittance of carbon is less than that of resin, therefore, for masks supported on carbon membranes, we varied the dose from 6,000 to 20,000 mA·s/mm and checked the photoresist structures to determine the optimal exposure dose. From the results, we concluded that an X-ray exposure dose of approximately 12,000 mA·s/mm was optimal for fabricating structures with 1:1 line-to-space ratio patterns with a pitch of 5.3 μm [4]. Figure 3 shows a picture of an X-ray grating on a 4 inch Si substrate made using the new carbon X-ray mask. The structure of the patterned photoresist over the whole area is excellent. On the other hand, the results obtained using the resin membrane X-ray mask, shown in Fig. 4, show the photoresist structure to be very poor. Pattern errors and sticking were observed from the bottom of the mask. These results demonstrate the superior performance of the carbon membrane-based X-ray masks.

We succeeded in fabricating an X-ray grating with a large effective area of 100 × 100 mm^2 on a 6 inch Si substrate, as shown in Fig. 5. This result shows that new carbon X-ray mask give the best performance.

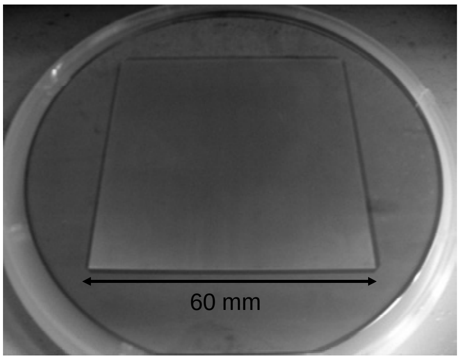

Fig. 3: *Picture of resist structure using newly carbon X-ray mask.*

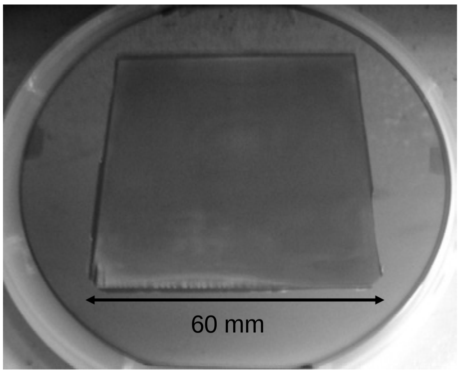

Fig. 4: *Picture of resist structure using resin membrane X-ray mask.*

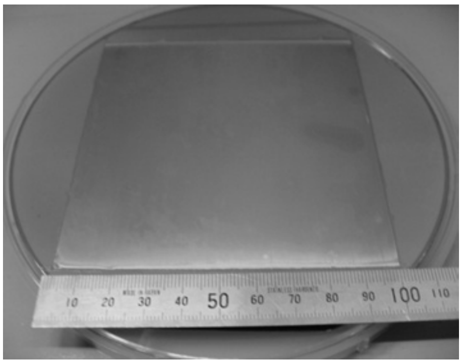

Fig. 5: *Picture of large area X-ray grating on 6 inch Si substrate.*

Conclusions

We fabricated a new type of X-ray mask on both 4 inch and 6 inch carbon wafers. The carbon wafer serves as the support membrane for the X-ray mask and resolves the problem of thermal deformation during X-ray exposure obtained when using masks with resin membranes.

We successfully fabricated large area X-ray masks on thin carbon wafers with patterns with a pitch of 5.3 μm. The 200 μm thick carbon wafer was sufficiently strong that further support around the edges of the membrane was unnecessary. Thus, the fabrication process is very easy compared to that using a resin support membrane which requires a frame bonded to the edges and etching to remove the Si substrate. The X-ray mask pattern formed on a 6 inch carbon wafer had a pitch of 5.3 μm and a height of 4 μm covering a large effective area of 100 × 100 mm^2. Using this new carbon X-ray mask, large area X-ray gratings were fabricated on 6 inch Si substrates.

Acknowledgment

This research was supported by the research project “Development of Systems and Technology for Advanced Measurement and Analysis” from the Japan Science and Technology Agency (JST).

References

[1] A. Momose, Jpn. J. Appl. Phys., **44**, 9A, pp. 6355-6367 (2005).

[2] A. Momose, W. Yashiro, T. Takeda, Y. Suzuki, and T. Hattori, Jpn. J. Appl. Phys., **45**, 6A, pp. 5254-5262, (2006).

[3] E. W. Becker, W. Ehrfeld, P. Hagmann, A. Maner, and D. Münchmeyer, Microelectron. Eng., **4**, 1, pp. 35-56, (1986).

[4] N. Takahashi, H. Tsujii, D. Noda, and T. Hattori, Proc. 2008 IEEE Int. Symp. Micro-Nano Mech. Human Sci. Nagoya, Japan, pp. 414-419 (2008).

Fabrication of Au Structure Using Direct Electroplating on Si Structures

Atsushi Tokuoka, Daiji Noda, and Tadashi Hattori
Laboratory of Advanced Science and Technology for Industry, University of Hyogo

Abstract

Good quality metallic structures can only be obtained by plating up from the bottoms of the etched grooves. Because it is difficult to form a seed layer just on the bottoms of the grooves, it is difficult to fabricate metallic microstructures in high aspect ratio grooves etched using silicon dry etching technology. To solve this problem, we developed a new fabrication method in which metallic microstructures are fabricated by electroplating directly into grooves etched in the Si after the sidewalls of the grooves have been coated with an insulating film. The depth of the grooves, and hence the thickness of the Au was 4 μm, and the pitch was 5.3 μm. Moreover, fabricating Au microstructures in deeper higher aspect ratio grooves were also attempted. As a result, 20 μm deep grooves were filled to a depth of 18 μm with Au. It is expected that this technology can be used in the production of a wide variety of devices.

Introduction

Recently, the miniaturization and efficient of machine parts and electronic parts are advanced, and highly precise microfabrication is requested for making a variety of microstructure needed. An X-ray lithography that uses the synchrotron radiation with a high directivity is paid to attention to make the highly accurate and high aspect ratio microstructure. Moreover, it is possible to make a metallic microstructure of a high aspect ratio by making the structure by X-ray lithography and the metal plating if the substrate is made a conductor. However, the use of the synchrotron radiation facilities where it requires a high cost is indispensable to need the synchrotron radiation with a high directivity for X-ray lithography. Then, a new fabrication process that the synchrotron radiation facilities are not used and the accuracy of the structure is not ruined is requested. Even if making the microstructure of the Si dry etching that uses Inductively Coupled Plasma Reactive Ion Etching (ICP-RIE) doesn't use X rays, the processing accuracy can make the microstructure of a high aspect ratio, as shown in Fig. 1.

It has been examined to make a metallic microstructure of a high aspect ratio by using the Si structure with the ICP-RIE in our laboratory. The metal used Au that was able to be formed with plating [1]. It was necessary to form the metallic seed layer only to the bottom of the groove of the microstructure to form the Au structure in the groove of the Si structure by the electroplating. If Au doesn't extract it only from a bottom of the structures, the cave can be done in the structure, and an excellent Au structure cannot be obtained as shown in Fig. 2. However, the method of having a metallic seed only to the bottom of the micro structure made by the Si dry etching is difficult for having a complex process and forming the microstructure to a large area and high aspect ratio.

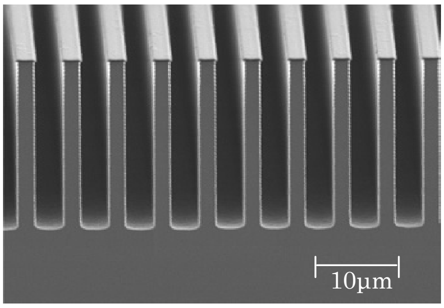

Fig. 1: *SEM image of Si microstructures with aspect ratio of 7.*

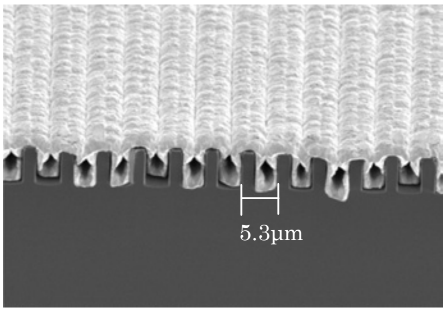

Fig. 2: *SEM image of defective Au structure.*

Fabrication of proposal Au microstructure

The new method for fabricating Au structures by directly electroplating on a structured Si substrate is shown in Fig. 3. The fabrication process consists of five steps: (1) applying resist to the Si substrate and forming a mask pattern in it using UV lithography, (2) etching grooves into the silicon by Si dry etching using an ICP etching system, (3) covering the Si structure and the remaining resist with a polymer film using the technique used in the Bosch process, (4) removing the polymer film from the bottoms of the grooves by vertical anisotropic etching (5) depositing Au in the grooves by electroplating up from the bottoms of the grooves only. This new Au microstructure fabrication method uses the polymer coating process normally used in the Bosch process.

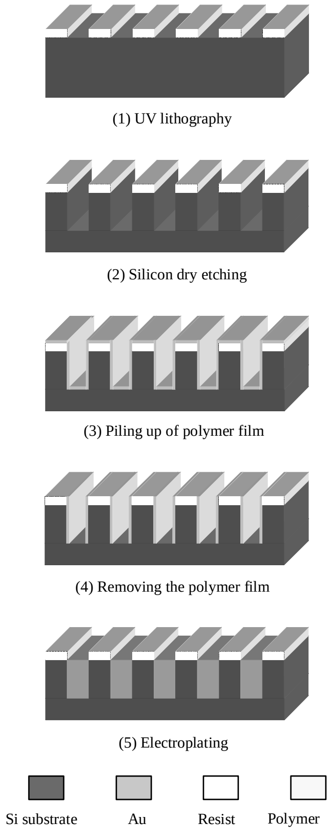

Fig. 3: *Fabrication process of new Au microstructures.*

It is necessary that growth takes place from the bottoms of the grooves only in order to form good quality Au structures. The polymer coating forms an insulating layer that prevents electroplating on the sidewalls.

Fabrication of Au structure

In our first attempts to deposit polymer films on Si microstructures, there was a tendency for the polymer to accumulate near the bottom of the groove, resulting in a thick layer at the bottom. This led to two problems. First, in addition to Au forming at the bottom of the groove, it was also formed near the top where the polymer was thin. Secondly, the thick polymer layer had an effect on the shape of the electroplated Au microstructure. Further attempts produced polymer films with much more uniform thickness as shown in Fig. 4. With these more uniform coatings, we were able to fabricate high-quality Au structures by electroplating as shown in Fig. 5. As the figure shows, Au formed by electroplating completely fills the 4 μm deep grooves etched in the substrate. However, to achieve a given width for the Au microstructure it is necessary to take into consideration both the width of the grooves in the Si structure and the thickness of polymer deposited on the sides. Nevertheless, these results reinforced our expectation that it is possible to fabricate much higher Au structures in more deeply etched Si.

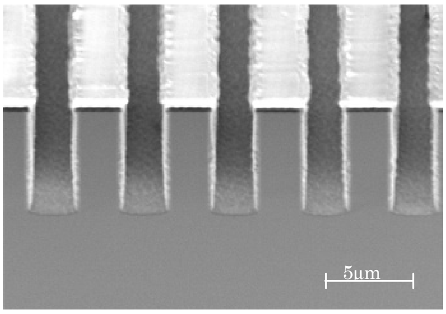

Fig. 4: *SEM image of uniformity polymer layer on Si microstructure.*

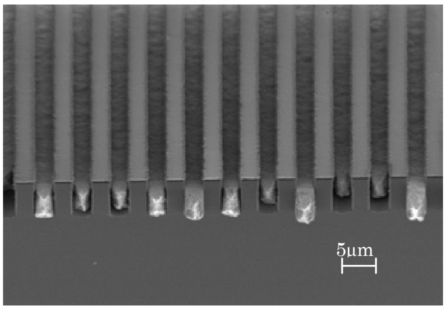

Fig. 5: *SEM image of Au structures*

Conclusions

In the present study, metallic microstructures were fabricated by filling with Au grooves etched in silicon by Si dry etching. The Au structures were fabricated by electroplating directly on the Si. However, good quality Au microstructures cannot be obtained by electroplating in etched grooves since growth takes place from both the bottoms and the sidewalls of the grooves. This can be achieved by coating the sidewalls with polymer, such as that used in the Bosch process used for Si dry etching. A 0.2 μm thick polymer film was found to be sufficiently insulating, so a film of about this thickness was deposited on the sidewalls of the etched grooves, which were then filled with Au by directly electroplating on the Si. As a result, Au structures 4 μm deep without voids were made. In addition, we were able to fabricate these Au structure over an area of 60 mm squares.

Acknowledgment

This research was supported by the research project “Development of Systems and Technology for Advanced Measurement and Analysis” from the Japan Science and Technology Agency (JST).

References

[1] H. Tsujii, K. Shimada, M. Tanaka, D. Noda, and T. Hattori, J. Advanced Mech. Design, Systems, Manuf., **2**, 2, pp. 246-251 (2008).

[2] F. Lamer, A. Schilp, K. Funk, and M. Offenberg, Tech. Digest MEMS ’99, pp.211-216 (1999).

Fabrication of High Performance Light Guide Plate

Takaya Fujimoto[1], Kenji Yamashita[2], Satoshi Nishida[2], Daiji Noda[1], and Tadashi Hattori[1]
[1]Laboratory of Advanced Science and Technology for Industry, University of Hyogo,
[2]Nanocreate Co., Ltd.

Abstract

Recently, LED (Light Emitting Diode) is paid to attention as a new source of light. However, it doesn't turn to shine on a wide area efficiently because LED is a point light. Then, the method of the light guide plate technology used for the liquid crystal display etc, and use as the LED lighting is examined. In the process of study, it has been understood that luminance increases by increasing the number of dots. Therefore, an accumulating method of piling up two or more light guide plates was proposed as a method of achieving high luminance for highly effective lighting usage, and the device was analyzed with an optical simulator. As a result of optimization, the average luminance has improved by 15 %.

Introduction

In recent years, the LED has received attention as a light source for a new form of lighting, taking the place of lighting forms such as fluorescent lamps [1]. Recently, LEDs with the luminous efficacy equal to that of a fluorescent lamp have been developed. Generally, the fluorescent lamp and the incandescent lamp are enumerated as forms of lighting. However, as for the advantages of using LEDs as a lighting source, low power consumption, high durability, and long life are enumerated. The power consumption of an LED is about half that of a fluorescent lamp; the longevity about five times as much. A considerable reduction in power consumption and the amount of waste generated can be expected through the replacement of the currently used incandescent and fluorescent lamp lighting with LED lighting. However, LED is not suitable for efficiently illuminating a wide area, because LED is a point light source. Products have been made using a method of arranging a large quantity of LEDs to shine over a wide area. However, irregularity in lighting due to their respective positions on the luminescence side, and there is the problem of high cost due to the large numbers LEDs required. Therefore, it was decided to convert LED point luminescence into plane emission form by using light guide plate technology, to increase the LED’s efficiency and solve the above problems. This method of LED lighting used is examined here. Figure 1 shows a schematic diagram of a light guide plate.

High performance light guide plate

In the light guide plate, light is guided from an LED or other light source to desired locations via total internal reflection rendered by an index of refraction differential between the air and the diffuser material. The light in light guide plate tears a total reflection condition by reflecting in an internal projection (dot) and irradiates the surface. The shape of the dots was assumed to be frustum of circular cone shape, that the diameter on was 10 µm, the diameter below was 52 µm, height was 30 µm, and taper corner is 70 degree, referring to past research results [2]. The light guide plate converts the point light source to plane emission. One advantage of the light guide plate is its efficient use of light through the conversion of point light sources to plane emission. To achieve uniform plane emission, an important factor is bumps on the light guide plate that release light from the diffuser surface. Uniform plane emission is achieved by rendering an optimal bump shape and allocation pattern.

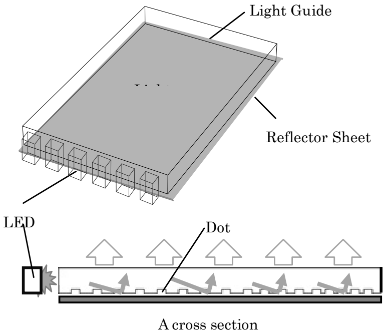

Fig. 1: *Explanation chart of light guide plate.*

Piling method

A high luminance LED and a light guide plate were combined to create a brighter lighting panel, for use as a lighting device. However, the size of the high luminance LEDs on the luminescence side was 5 mm, and there were no a light guide plates available of appropriate thickness. Therefore, we considered either two light guide plates of board thickness 2.6 mm or five light guide plates of board thickness 1 mm, piled up, to be suitable for the luminescence side. The result of increasing the number of piled sheets was to raise the mean luminance obtained. The reasons were thought to be the dots arranged by piling up two or more light guide plates besides the light guide plate bottom, and the ability to increase the number of dots even in a light guide plate of the same thickness. This was because of the higher probability that light would hit the dots, as shown in Fig. 2. Therefore, a piling

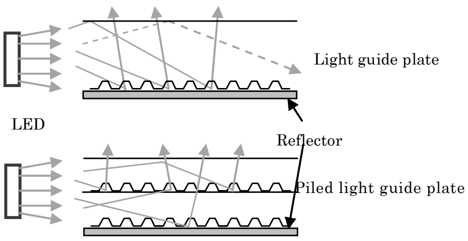

Fig. 2: *Ray route outline chats of each light guide plate.*

method of piling up two or more light guide plates was proposed as a method of achieving high luminance for highly effective lighting usage, and the device was analyzed with an optical simulator.

First of all, a small light guide plate (30 × 30 mm^2) was used. The dot arrangement area, the number of sheets piled up, and the total board thickness of the light guide plates was changed and the results were analyzed. An air layer of 0.01 mm was inserted between each light guide plate. The light source on the luminescence side used one white LED whose size matched each total board thickness. The measuring method emitted white light of 1 W from the LED, and measured the total energy of the light emitted from the luminescence side of the light guide plate. Figure 3 shows the result for a total board thickness of 2 mm.

The total light output energy changed according to the number of piled sheets and the total number of dots on the light guide plate. This result could also be confirmed for other total board thicknesses. Although in some cases the light output energy became saturated, the total light output energy increased as a result of any increases in the number of piled sheets and the total number of dots.

A piled light guide plate of the same condition was designed and verified according to a light guide plate (luminescence area = 50 × 90 mm^2, board thickness = 1 mm) that had been designed and made by a previous research for the sake of comparison. Figure 4 shows simulation results of usual type and piled type. Average luminance is 767 cd/m^2 in the piled light guide plate, compared to an average luminance of 668 cd/m^2 in a past light guide plate; hence the average luminance improved by about 15 %. Moreover, the dot total is 480,779 pieces in the piled light guiding plate while the dot total is 191,008 pieces in the previous light guide plate. The number of dots is about 2.5 times the previous figure. The number of sheets of accumulating was decided and optimized so that the number might become one million that was the number of saturation dots.

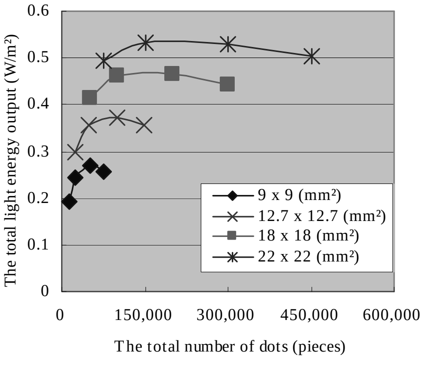

Fig. 3: *The relationship between the total light energy output and the total number of dots.*

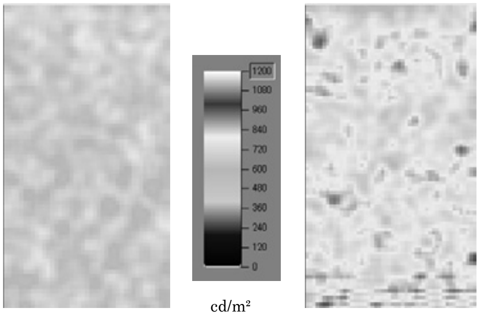

(a) usual (b) three pieces piled

(a)		(b)
668	average luminance (cd/m^2)	767
94	illumination uniformity (%)	95

Fig. 4: *Luminance distribution on surface of each light guide plate (simulation).*

Conclusions

The method of improving the utilization efficiency of light further to apply the light guide plate made in this laboratory as a form of lighting, and achieving high luminance, were examined. The light guide plates were piled up as a method of raising the utilization efficiency of light and the method of achieving high luminance by the piling method to increase the total of number of dots was proposed. The piling method was verified by using the simulation. Near a practical size as the lighting because a light guide plate so far at the time of optimized it in the past was compared with the piled light guide plate based on the above-mentioned result, and optimization of the arrangement of the dots of the piled light guide plate of luminescence area 50 × 90 mm^2 and the total board thickness 1 mm was achieved. As a result of optimization, the average luminance of the piled light guide plates was 767 cd/m^2, while that of previous light guide plates was 668 cd/m^2, representing an improvement of about 15 %.

It will be possible to convert it to a higher luminance light guide plate even when the same source of light is used.

References

[1] H. C. Chien and Z. P. Chen, Microsyst. Technol. **15**, pp. 383-389 (2009).
[2] Y. Okayama, K. Yamashita, D. Noda, and T. Hattori, Proc. 2008 IEEE Int. Symp. Micro-Nano Mech. Human Sci., pp. 408-413 (2008)

Technique for Preparing Defect-free High Aspect Ratio SU-8 Resist Structure Using X-ray Lithography

V. K. Singh, S. Maekawa[1], M. Katori[2], Y. Minamiyama[2], D. Noda[3], and T. Hattori[3]
[1]Natioal Institute of Information and Communications Technology, [2]Nanocreate Co., Ltd.,
[3]Laboratory of Advanced Science and Technology for Industry, University of Hyogo

Abstract

This paper describes the process of deep X-ray lithography (DXRL) using epoxy negative photoresist SU-8. Resist coating, soft bake, exposure, post exposure bake, and development of the resist are characterized. We have successfully fabricated HAR and defect-free vertical channel structures of 100 and 200 μm depths with 10 μm width in SU-8 resist introducing a new vapor development technique that will be useful for various MEMS devices. Utilizing this technique, we can not only increase the exposure dose for thicker resist structure without worrying the over dose effect but also reduce the developing time significantly.

Introduction

This paper describes the process of deep X-ray lithography (DXRL) using epoxy negative photoresist SU-8. Resist coating, soft bake, exposure, post exposure bake, and development of the resist are characterized. The negative resist SU-8 has been increasingly used in micro- and nanotechnologies due to its excellent coating, planarization and processing properties as well as its mechanical and chemical stability. The fabrication of polymer based high aspect ratio (HAR) micro-pillar structures by X-ray lithography is investigated. A low-energy beam line of 1.0 GeV with carbon X-ray mask is used to create arrayed micro-pillars on soda glass. One of the major limitations in the use of SU-8 in lithographic processes is the occurrence of internal stress and hence the distortion of the microstructure. In this study, a technique for preparing the defect-free HAR SU-8 resist structure is described.

Experimental

The resist used for the process is SU-8 3050. The resist height is approximately 200 μm, achieved by twice spin coating. The samples are soft baked at 95 ºC for 1 to 12 hours to remove the solvent [1]. The X-ray exposure doses used are from 10,000 to 25,000 mA·s/mm. The Post exposure bake (PEB) is carried out at 95 ºC for 1 to 10 min. The substrates are developed using pure PGMEA with gentle ultrasonic agitation. The parameters of Soft bake time, exposure dose, and PEB temperature and time are considered to have an influence on stress developed in resist structure [2]. The complex balance of parameters decides the quality of the resist structure.

Results and discussions

Figure 1 shows the optical micrographs of resist pattern exposed at different doses. It is shown that as exposure dose value increases, resist residue on top surface of the pattern increases due to the higher internal stress. The typical thicknesses of bumps on pattern edge and cross-shaped pattern edge are 1.5 and 0.5 μm, respectively. This result suggest that limitations of exposure dose value for SU-8 resist that means thicker resist where higher dose is needed cannot be fabricated successfully.

Figure 2 shows the effect of PEB temperature on the resist pattern. The exposure dose used is 25,000 mA·s/mm for 200 μm thick SU-8 resist. Figure 2(a) shows a photograph of cross- shaped pattern after X-ray exposure and before PEB. The temperature during X-ray exposure is assumed 30 ºC. Figure 2(b) shows a photograph after PEB at 65 ºC for 1 min. it can be seen that unexposed resist start to come out from the channel due to the expansion of exposed resists. It further becomes worse when PEB is carried out at 95 ºC for 1 min to enhance the cross-linking of the exposed resist as shown in Fig. 2(c). However, the recommended PEB process is 5 to 10 min at 95 ºC from the technical data sheet to complete the

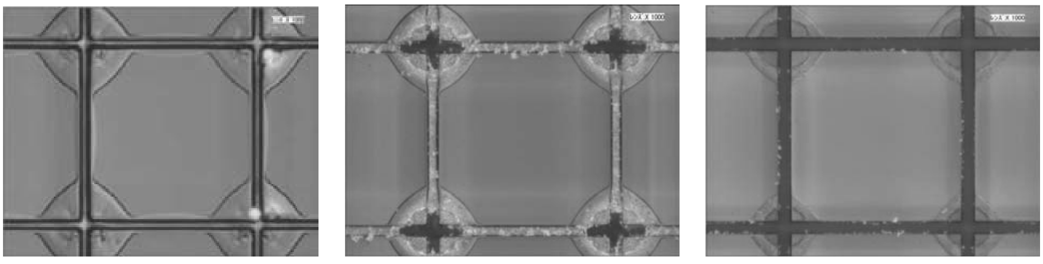

(a) 25,000 mA· s/mm (b) 20,000 mA· s/mm (c) 15,000 mA· s/mm

Fig. 1: *Top view of fabricated pillar array. The exposure doses are changed. Resist residue can be seen surrounding the cross-shaped design in a decreasing manner.*

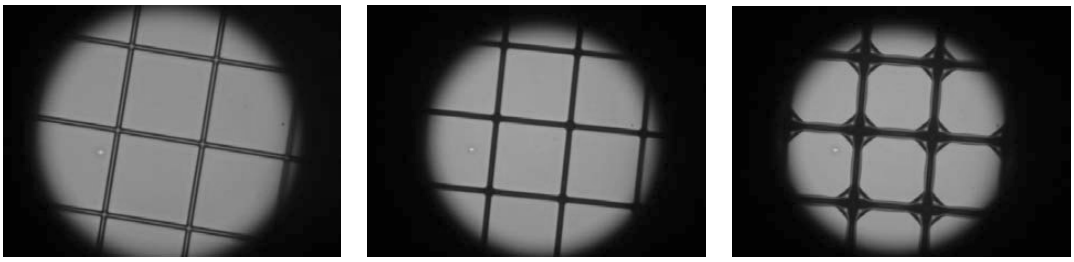

(a) (b) (c)

Fig. 2: *Optical photographs of (a) X-ray exposed sample, (b) after PEB at 65 °C for 1 min, and (c) further at 95 °C for 1 min. Resist residue increases with PEB temperature and time.*

cross-linking. It means longer PEB cannot be applied to avoid the resist residue problem.

A technique that can be applied without any limitation and with no side effects is attractive. For removing resist residue developed during DXRL on the resist structure, the post exposure baked sample is placed in a caped beaker with the liquid developer, PGMEA at room temperature for 15 min as shown in Fig. 3. The resist is considered to diffuse from thick region to thin region and spread surrounding surface due to surface tension effect. Figure 4(a) shows top SEM view of the pillars structure. The residue of resist can be seen clearly. The coefficient of thermal expansion (CTE) of SU-8 is 52 ppm/ºC [3]. It has been noticed that unexposed SU-8 might be squeezed out of a channel due to the thermal expansion of the exposed region, resulting in a resist residue on the top surface. The problem caused by thermal expansion becomes more serious when the exposed area is bigger. In our case, pillars are square of 150 × 150 μm^2 arranged with 10 μm gap. The effect caused by the large internal stress can be alleviated either by reducing the exposed area or by generating a discrete small-sized exposed region [4]. But this idea also limits the area of fabrication design and structure. Figure 4(b) shows top SEM photograph of resist structure after PGMEA vapor treatment. By putting the X-ray exposed sample in the caped beaker with PGMEA after PEB, the photoresist flows on the sample and becomes enough soft to remove during standard developing. This technique smoothen the resist surface too.

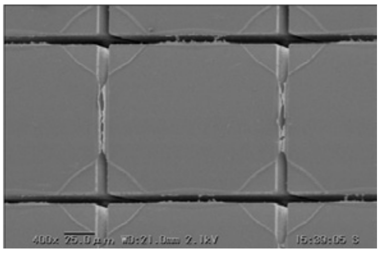

(a) normal condition

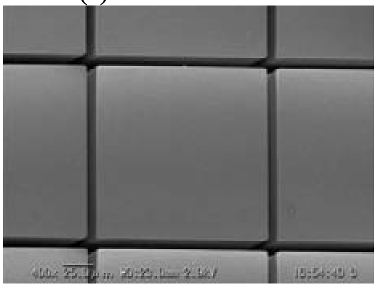

(b) after vapor treatment

Fig. 4: *SEM image of SU-8 resist pattern by X-ray lithography. Top views of resist pattern (a) suffering from resist residue problem, (b) becomes defect-free after applying PGMEA vapor treatment.*

Conclusions

We have successfully fabricated HAR and defect-free vertical channel structures of 100 and 200 μm depths with 10 μm width in SU-8 resist introducing a new vapor development technique that will be useful for various MEMS devices. More detail investigation on the fabricated micro structures are still under researches. Utilizing this technique, we can not only increase the exposure dose for thicker resist structure without worrying the over dose effect but also reduce the developing time significantly.

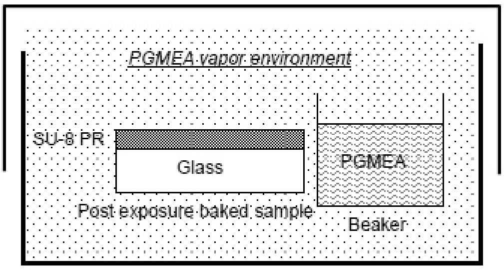

Fig. 3: *Setup for putting the sample in the PGMEA vapor environment.*

References

[1] L. Singleton, M. Kufner, and S. Megtert, J. Photopolym. Sci. Technol., **14**, pp. 649-656 (2001).

[2] R. L. Barber, M. K. Ghantasala, R. Divan, K. D. Vora, E. C. Harvey, and D. C. Mancini, Microsyst. Technol., **11**, pp. 303-310 (2005).

[3] H. Lorenz, M. Laudon, and P. Renaud, Microelectron. Eng., **41-42**, pp. 371–374 (1998).

[4] C. H. Lin, G. B. Lee, B. W. Chang, and G. L. Chang, J.Micromech. Microeng, **12**, pp. 590-597 (2002).